Tesis Doctoral

Ingeniería en Automática, Robótica y Telecomunicación

Accurate navigation applied to landing maneuvers on mobile platforms for unmanned aerial vehicles

Autor: Francisco Alarcón Romero

Directores: Dr.-Ing. Aníbal Ollero Baturone

Dr.–Ing. Antidio Viguria Jiménez

Dpto. Ingeniería de Sistemas y Automática

Escuela Técnica Superior de Ingeniería

Universidad de Sevilla

Sevilla 2019

Propuesta de tesis doctoral para la obtención
del título de Doctor por la Universidad de Sevilla

Accurate navigation applied to landing maneuvers on mobile platforms for unmanned aerial vehicles

Autor:
Francisco Antonio Alarcón Romero

Director 1:

Aníbal Ollero Baturone

Director 2:

Antidio Viguria Jiménez

Doctorado en Ingeniería Automática, Electrónica y de Telecomunicación

Escuela Técnica Superior de Ingeniería

Universidad de Sevilla

Sevilla, 2019

A Marta, Martita y Carlota,
las niñas de mis ojos.

Acknowledgements

I would first like to thank Antidio Viguria and Anibal Ollero for supervising my thesis. It has been a luck and a privilege to receive your guidance and advice during the last ten years. Special thanks to Antidio, his support has been invaluable and he has given me the opportunity of combining this thesis with the projects in which I have participated.

Moreover, it is necessary to say that this dissertation would not have been possible without the incredible work carried out by the CATEC staff and other extraordinary engineers that currently are spread out by the world. During these years they have become not only colleagues but also friends. I would like to mention especially to Manuel García, Paco Cuesta, Miguel Cordero, Daniel Santamaría, Antonio Jiménez and, of course, to my favorite pilots: José Ramón López and Allan Bell.

Finally, I would like to thank all my family and friends, as always, for their never-ending support. Very special thanks to my parents and my brother, without any doubt; they have been the key to become who I am. Also to my "other family", which is the one that is composed of my closest and faithful friends, thanks for being my Gladiators, the brothers that provide me the Force And Honor to enjoy and overcome any circumstance. And most of all, thanks to my loved Marta, certainly you are the cornerstone and the partner of my life. Thanks for your continued support, patience and understanding in the final stages of my work.

Francisco Alarcón Romero

Sevilla, 2019

Abstract

Drones are quickly developing worldwide and in Europe in particular. They represent the future of a high percentage of operations that are currently carried out by manned aviation or satellites. Compared to fixed-wing UAVs, rotary wing UAVs have as advantages the hovering, agile maneuvering and vertical take-off and landing capabilities, so that they are currently the most used aerial robotic platforms.

In operations from ships and boats, the final approach and the landing maneuver are the phases of the operation that involves a higher risk and where it is required a higher level of precision in the position and velocity estimation, along with a high level of robustness in the operation. In the framework of the EC-SAFEMOBIL and the REAL projects, this thesis is devoted to the development of a guidance and navigation system that allows completing an autonomous mission from the take-off to the landing phase of a rotary-wing UAV (RUAV). More specifically, this thesis is focused on the development of new strategies and algorithms that provide sufficiently accurate motion estimation during the autonomous landing on mobile platforms without using the GNSS constellations.

In one hand, for the phases of the flights where it is not required a centimetric accuracy solution, here it is proposed a new navigation approach that extends the current estimation techniques by using the EGNOS integrity information in the sensor fusion filter. This approach allows improving the accuracy of the estimation solution and the safety of the overall system, and also helps the remote pilot to have a more complete awareness of the operation status while flying the UAV

In the other hand, for those flight phases where the accuracy is a critical factor in the safety of the operation, this thesis presents a precise navigation system that allows rotary-wing UAVs to approach and land safely on moving platforms,

without using GNSS at any stage of the landing maneuver, and with a centimeter-level accuracy and high level of robustness. This system implements a novel concept where the relative position and velocity between the aerial vehicle and the landing platform can be calculated from a radio-beacon system installed in both the UAV and the landing platform or through the angles of a cable that physically connects the UAV and the landing platform. The use of a cable also incorporates several extra benefits, like increasing the precision in the control of the UAV altitude. It also facilitates to center the UAV right on top of the expected landing position and increases the stability of the UAV just after contacting the landing platform.

The proposed guidance and navigation systems have been implemented in an unmanned rotorcraft and a large number of tests have been carried out under different conditions for measuring the accuracy and the robustness of the proposed solution. Results showed that the developed system allows landing with centimeter accuracy by using only local sensors and that the UAV is able to follow a mobile landing platform in multiple trajectories at different velocities.

Contents

Figures

Tables

Acronyms

AL	Alert Limit
AGL	Altitude above ground level
ATLAS	Air Trafic Laboratory for Advanced unmanned Systems
AHRS	Attitude and Heading Reference System
CG	Center of Gravity
UCARS	Common Automatic Recovery System
UTC	Coordinated Universal Time
CP	Contact Point
DOP	Dilution of Precision
EC-SAFEMOBIL	Estimation and Control for SAFE wireless high MOBILity cooperative industrial systems
ECEF	Earth-centered earth-fixed frame
EGNOS	European Geostationary Overlay Service
EIRE	EGNOS IntegRity wEighted
EKF	Extended Kalman Filter
GNSS	Global Navigation Satellite System
GPS	Global Positioning System
GIVE	Grid Ionospheric Vertical Error
GCS	Ground Control Station
GSU	Ground Segment Units
GNC	Guidance, Navigation and Control
HDOP	Horizontal Dilution of Precision
HPL	Horizontal Protection Level
ICAO	International Civil Aviation Organization
IMU	Inertial Measurement Unit
INS	Inertial Navigation System
ILS	Instrumental Landing System

IOD	Issues of Data
LLA	Latitude, Longitude, altitude
LC	loosely coupled
MTOW	maximum take-off weight
MEMS	micro-electro-mechanical systems
MBZIRC	Mohamed Bin Zayed International Robotics Challenge
NDB	Non Directional Beacon
NED	north, east and down
OPATS	Object Position and Tracking Sensor
PCU	Positioning Calculation Unit
PDOP	Positional DOP
PL	protection level
PLC	Programmable Logic Controller
PPK	Post-Processed Kinematic
RAST	Recovery Assist, Secure and Transverse
RBS	Radio Beacon System
RC	Radio Control
R-GRANT	Radiobeacon–based GNSS-free RelAtive NavigaTor
RMS	Root Mean Square
RMU	Range Measurement Unit
RTK	Real Time Kinematics
RUAV	Rotary-wing UAV
SBAS	Satellite Based Augmentation System
STD	Standard Deviation
T-GRANT	Tether–based GNSS-free RelAtive NavigaTor
TC	Tightly coupled
TTA	Time To Alarm
TWA	Threshold and Weighted by Accelerations
UAV	Unmanned Aerial Vehicles (UAV)
UDRE	user differential range error
UIRE	user ionospheric range error

UWB	Ultra Wide Band
VDOP	Vertical Dilution of precision
VPL	Vertical Protection Level
VOR	VHF Omnidirectional Range
VTOL	Vertical Take Off and Landing
WGS84	Worl Geodetic System 1984

INTRODUCTION

1.1. Motivation

Unmanned Aerial Vehicles (UAV) are one of the most promising areas in the aeronautical industry worldwide. They represent the future of a high percentage of operations that are currently carried out by manned aviation or satellites. UAVs are becoming a powerful tool in strategic frameworks, not only for military use but also regarding civil and commercial applications.

In the last decade, drones have attracted significant interest in a wide range of applications, exploiting their ability to fulfill multiple mission types. Such applications include exploration (Stumberg et al., 2017) and inspection missions(McAree, AitKen and Veres, 2016), surveillance or monitoring tasks like landmine detection(Ganesh, Raju and Hegde, 2017), border protection and law enforcement (Kim and Lim, 2018), infrastructure inspection (Máthé and Busoniu, 2015), traffic surveillance(Vahidi and Saberinia, 2018), dumping detection of toxic substances and environmental disaster management(Erdelj et al., 2017).

The use of unmanned rotorcrafts for a wide variety of applications has increased during the last years. Compared to fixed-wing UAVs, rotary wing UAVs have the advantage of hovering, which is useful for monitoring some regions of interest, and their agile maneuvering and vertical take-off and landing capabilities. Easy to transport and deploy, these autonomous flying vehicles are cost-effective platforms to carry cameras and other surveillance equipment or even to transport and deploy loads.

Uncertainty in the position estimation of moving objects directly determines the safety distance to other mobile entities for safe operation. Coupled control of close mobile objects requires very precise relative motion estimation in order to reduce the safety distance, especially in presence of environmental perturbations. Even if some of these hazardous operations have already been performed in some particular conditions with lower uncertainty (i.e. landing on ship decks with benign wind and sea condition) or using mechanical linkages (i.e. cables to assist

landing), the safe efficient implementation in more severe conditions avoiding accidents still requires novel, very accurate motion estimation/prediction with sensor data fusion and closing reliably wireless sensing and actuation real-time control loops in spite of perturbations such as turbulence and other environmental uncertainties. In these applications the replacement of complex mechanical devices by more flexible and lower cost embedded systems maintaining safety requires a combination of a very accurate estimation on the relative position/motion between the mobile objects; and coordinated control. The performance and reliability of the mobility control methods depend directly on the quality of the state estimation. If a very fast and precise estimation of the relative displacement between the mobile platforms is available, physical couplings between the mobile entities could be eliminated and substituted by a control approach, at least under certain conditions. However, in many applications areas, the state cannot be measured directly with the required level of quality and reliability. Therefore, elaborated state estimation approaches are needed for coupled motion control. Thus, in the autonomous landing on mobile platforms, motion estimation is a prerequisite to land at the right time, as the moving platform and the flying vehicle are inertial moving objects.

Lack of reliability is usually related to uncertainties in the models and estimations and unexpected events but is also dependent on hardware, wireless communications, and architectural issues. Safety plays a critical role in the coordination and cooperation of high mobility systems. This thesis addresses the development of new estimation/prediction and their practical application to highly mobile entities with complex dynamics and functional behavior. Here, the main emphasis is placed on the preservation of safety and reliability while optimizing performance, taking into account uncertainties of sensor data and unreliability of wireless data transmission links. This formulation is critical in high mobility systems, including many industrial systems and many services. This work involves very precise motion estimation and safe guidance technologies to perform critical maneuvers such as the autonomous landing on mobile platforms. High accuracy and high-frequency control loops are required in these operations in the inner loops of the autopilot system so, the state vector computed through the estimation module needs to have a high update rate, higher than the controller algorithms.

This thesis is devoted to the development of a guidance and navigation system that allows completing an autonomous mission from the take-off to the landing phase of a rotary-wing UAV (RUAV). More specifically, this thesis is focused on the

development of new strategies and algorithms that provide sufficiently accurate motion estimation during the autonomous landing on mobile platforms without using the GNSS constellations.

1.2. Thesis Outline

This thesis consists of seven chapters and two appendices. A summary of the content is presented here:

- Chapter 2 presents a review of the state of art regarding navigation systems developed for the autonomous landing of unmanned helicopters on mobile platforms. It also studies the current state of the use of the EGNOS constellation in estimation filters. Main contributions of this thesis are also underline along this chapter.
- Chapter 3 describes the main phases of an autonomous mission and presents the guidance and navigation architecture implemented in the autopilot of the RUAV. It also presents the main systems and coordinate frames that will be used in the following chapters, paying special attention to the key technologies used throughout this thesis: EGNOS, the tether device and the radio-beacon system.
- Chapter 4 details the new navigator developed in this thesis for the take-off and waypoint navigation phases of an autonomous mission. This navigator is based on global coordinates and uses the EGNOS integrity information for improving the accuracy of the positional solution and the safety of the system.
- Chapter 5 presents a novel GNSS-free relative navigation system that will be used for the final approach of the UAV to a moving platform and for the landing maneuver. It details the novel system and measurements model developed and implemented in the fusion filter for the tether and the radio-beacon systems. This new navigation system does not make use of the GNSS technology and offers an alternative and accurate way for landing on a moving platform.
- Chapter 6 describes the field experiments carried out for testing the

developed navigation systems. Here, it is possible to note the strong experimental focus of this dissertation; in fact, throughout this thesis, more than 70 flights were performed in order to measure the performance of the different estimation algorithms implemented. In that way, this chapter summarizes the different test campaigns and presents the main results obtained.

- Chapter 7 presents the main conclusions and future lines of work.
- Appendix A contains the assumptions and the constraints of the landing platform motion in order to study its similarities with the movement of a ship under different environmental conditions.
- Appendix B presents the main coordinated frames used along this thesis and how to perform the transformations between them.
- Appendix C This section presents the sensors used by the global navigation system (excepting EGNOS) and their main characteristics and error properties, which will be used for building the mathematical models of the fusion algorithms.

1.3. Thesis Framework

On one hand, work related with the landing phase of the helicopter has been performed in the framework of the European Commission FP-7 project EC-SAFEMOBIL (Estimation and Control for SAFE wireless high MOBILity cooperative industrial systems). Under this framework, this thesis proposes the use of two different navigation and guidance strategies for performing a safe landing in a moving platform:

- The use of a tether as relative sensor,
- The use of a system based on radio-beacons signals (RBS) as relative sensor.

On the other hand, the experimental campaigns that validate the work related to the UAV global navigation phases have been carried out under the project REAL (RPAS EGNOS Assisted Landings). REAL has received funding from the European GNSS Agency within the framework program "EGNOS ADoption in Aviation".

Under this framework, this thesis has validated a new navigation algorithm based on the benefits that the EGNOS constellation provides to the aviation users.

2. STATE OF THE ART AND CONTRIBUTIONS

2.1. Autonomous landing of rotary-wing UAVs on moving platforms

In the next decade, it is expected that civil applications of Unmanned Aerial Vehicles will increase exponentially up to a market of 11.000 millions of euros in 2035 only in Europe. Moreover and due to the intrinsic low risk of maritime operations with UAVs, it is foreseen an important increase in the use of UAVs from ships, for different applications: environmental monitoring, fishing support, surveillance, etc. In operations from ships and boats, the final approach and the landing maneuver are the phases of the operation that involves a higher risk and where it is required a higher level of precision in the position and velocity estimation, along with a high level of robustness in the operation. Although landing of rotary-wing UAVs has raised the attention of multiple researchers during the last 15 years, it has not been yet completely solved in a robust and reliable manner. In fact, one of the three challenges at the Mohamed Bin Zayed International Robotics Challenge (MBZIRC) Competition in 2017 was the landing of a UAV on a moving platform (Acevedo et al., 2018).

One of the first research works that tackle the autonomous landing problem on mobile platforms was (Saripalli, Montgomery and Sukhatme, 2003) in 2003, where a real-time, vision-based landing algorithm was developed. Later, references(Saripalli et al., 2006),(Merz et al., 2006) presented vision-based algorithms that were able to estimate the helicopter position from images of a specially designed landing pad with the necessary level of precision and accuracy for the landing maneuver, most of the data was achieved from manual flights and simulations. More recently, references(Falanga et al., 2017),(Polvara et al., 2018) also have applied vision-based landing techniques increasing the autonomy level by including real-time trajectory generation. Also, it is possible to find recent works that study the problem of landing in an oscillating platform by using visual sensors. For instance, the authors in (Polvara et al., 2018) use a fiducial marker in

order to obtain the pose of the platform and implement an Extended Kalman Filter (EKF) to estimate the ship position. Simulations provide results very accurate by using only the odometry and the inertial measurements for the estimation. However, measurements from these sensors may not always be available, and they can suffer physical interferences and limitations in their fields of view. Additionally, these approaches generally only work under good light or visibility conditions so its performance has a strong dependency with the weather conditions, seriously limiting their applicability under a wide range of realistic scenarios for the landing operation. Moreover, some of these vision-based techniques assume the use of the Global Navigation Satellite System (GNSS) on their navigation systems, since the vision system is only used as an input that increases the precision of the relative estimation of position and velocity with respect to the landing platform. Therefore, the robustness of these solutions is compromised due to the known problems of current GNSS systems in environments without enough visibility.

Other methodologies used in the autonomous approach and landing phases of UAVs are based on the implementation of ground system infrastructures that help the vehicle to obtain its position. Commonly, in general aviation, the approach procedures are exclusively based on the ground navigation aids, such as Instrumental Landing System (ILS), VHF Omnidirectional Range (VOR) and Non-Directional Beacon (NDB)(Chiesa et al., 2014). However, in this kind of procedures, it is required expensive and big infrastructures, GNSS technology is usually involved, the landing location is generally a static runway and the aircraft has previous knowledge of the fixed position of the radio transmitter radio beacon. These reasons do not allow implementing traditional architectures in a mobile platform for aiding in the guidance and navigation tasks. Some other types of ground infrastructures have been explored for UAV autonomous landing in GNSS-denied environments, such as laser range finders, millimeter-wavelength radar, etc (Weiwei et al., 2017).

Also, it is possible to find several commercial systems that pretend to solve the autonomous landing task through the implementation of ground infrastructures. For example, the company RUAG developed a solution called OPATS (object position and tracking sensor) (RUAG, n.d.). Their system is based on a laser-based automatic landing system for UAS that represents an alternative to radar-based landing systems. Its key feature system is the continuous position measurement of

the approaching unmanned aircraft using an infrared laser beam which is echoed back from a passive heated retro-reflector on the aircraft. This system can measure the position of an approaching aircraft at a distance around 4000 m. Another commercial system is the Common Automatic Recovery System (UCARS) (Sierra Nevada Corporation, n.d.) developed by Sierra Nevada Corporation. This system is based on a millimeter-wavelength ground radar and provides precision approach (within 2.5 cm) in adverse weather condition and without using the GNSS. While those solutions are effective, these technologies are not valid for this project due to the limited payload of small UAVs and the needed of a communication channel between the ground infrastructure and the aerial vehicle. In (Kim and Choi, 2016), the authors deployed passive Ultra Wide Band (UWB) anchors in the landing location, which listen for the UWB signals emitted from a UAV. The position of the target is computed on ground and sends it back to the UAV through an aviation communication channel. This work achieves a positioning accuracy of 40 cm. However, here also it is needed a communication channel. Besides this, in this work all the presented tests have been performed in static scenarios. In this dissertation, one of the novelties presented is the implementation of a new system based on a ground infrastructure for the approach and autonomous landing phases of a rotary unmanned aerial system. This system is based on several radio-beacon deployed on the ground following a specific pattern and with an operation similar to the GNSS constellation. Each radio-beacon transmits its own radio signal, then the UAV receives them and perform a triangulation that allows positioning itself. The position accuracy obtained by using this system has tested to be under one meter. Furthermore, this system can be deployed in any landing platform, both static and moving, and does not rely on GNSS signals or a communication channel. Another advantage of this system is that the vehicle equipment is low weight, allowing its integration into UAVs with a maximum take-off weight (MTOW) under 25 kg.

Related to the final landing phase in a moving platform with cm accuracy and without the use of GNSS sensors, this thesis proposes the use of a tether. The use of a cable or tether that physically connects the UAV and the moving platform is not new, although as it will be explained in the following, most of the existing works were theoretical and only with simulation results. Some works were focused on the study of the control and stabilization problems of tethered rotorcrafts such as (Schmidt and Swik, 1974). Also in (Rye, 1985) it can be found a study of the longitudinal stability of a hovering tethered rotorcraft. The first use of a tether for

helping in the landing phase of a UAV can be found in (Oh et al., 2006) where a controller is developed in order to use the tether tension to couple the translation of the helicopter to the rotation.

In (Sandino et al., 2015), an Unscented Kalman Filter is applied to the attitude and relative position estimation of a small-size tethered unmanned helicopter. For that purpose, the state prediction is performed using a kinematic process model driven by measurements of the inertial sensors (accelerometer and gyroscope) onboard the helicopter and the subsequent correction is done using information from additional sensors like magnetometer, radar altimeter and magnetic encoders measuring the tether orientation relative to the helicopter. This approach avoids the need of a global positioning system (GPS) as the position is estimated relative to the anchor point. Simulation results show a good performance in terms of estimation errors as well as CPU time. However, an improvement point mentioned by the authors in their conclusions is the dependence of the filter performance on the information related to the platform state. Although simulation results have shown that this performance is good enough for execution within the controller feedback when platform motion is totally unknown, the performance improves considerably when this information is taken into account.

In (Mfiri et al., 2016) the authors describe the design of a flight control system architecture for a tethered quad-rotor aircraft where the tether is also used for transmitting power to the UAV. Results from simulated waypoint navigation and hovering of the tethered vehicle suggest that the designed system is fit for use in an automated landing mission. In (Nicotra, Nald and Garone, 2017), the authors take advantage of the tensile force acting along the taut cable and solve the nonlinear control of the tethered UAV by using a cascade control scheme based on thrust vectoring and using a novel "Reference Governor scheme". The work presented in (Glick and Arogeti, 2018) is also focused on the control design problem of a tethered drone and uses the tether as a position sensor. Simulations results show that a fully autonomous flight could be achieved indoors by using its approach. However, in all these works the tether is used just for control and stability purposes and all the results and conclusions are obtained from simulations.

There are very few experimental results regarding the use of a tether with a UAV for landing purposes. The first experimental results can be found in (Sandino et al., 2014), where a tethered helicopter lands autonomously over a static landing platform in an outdoor scenario. This work explores an alternative approach to

GPS sensors to avoid typical drawbacks, such as inaccuracies of standalone sensors or weight/cost for Real Time Kinematic (RTK) setups. Appropriate sensing of tether attitude relative to the helicopter together with an altitude measurement, allows estimation of the helicopter's linear position relative to the landing point. However, landing in mobile platforms is not considered and the relative estimation is simply based on geometrical considerations. Previous work was extended in (Sandino et al., 2016) with more experimental tests but in this case the main focus was on the control strategy and the advantages that a tether can provide to the stability of a UAV. In (Kiribayashi, Yakushigawa and Nagatani, 2017), a power-feeding tethered micro UAV is used and a position estimation method based on observing the slack tether is proposed. Some indoor experiments are carried out in order to prove the feasibility of this method. The authors in (Xiao et al., 2018) propose to localize a UAV in indoor environments by using only a quasi-taut tether. The tether's sensory feedback is fed into a catenary-based mechanics model to localize the UAV in an indoor global frame defined by the tether reel center. Their localization method was tested on a real robot (Fotokite Pro). Although it is true that it is possible to find real experimental data in (Kiribayashi, Yakushigawa and Nagatani, 2017) and (Xiao et al., 2018), landing tests in these works were performed over static platforms and in indoor scenarios where the weather conditions do not affect the navigation capabilities.

The rope system developed in this work has been designed for landing a rotary-wing UAV (RUAV) on a mobile platform with a high level of accuracy and robustness, and without using GNSS. The design has been inspired by the Recovery Assist, Secure and Transverse (RAST) system used by manned helicopters to improve the stability using a tether during the landing operation (Mcgeer and Von Flotow, 2013). Main contributions of this work are: the use of the radio-beacon and/or a tether to estimate the relative position and velocity between the UAV and the mobile platform without using GNSS, the design of a robust guidance approach to perform landings in a safe and robust manner, and the validation of the designed algorithms in a large number of flying tests, including landings with speeds of the mobile platform up to 40 km/h. The relative information obtained from the navigator developed along this thesis is entirely independent of the GNSS and represents an alternative, low cost and reliable positioning system for tethered helicopter UAVs or multicopters. Therefore, the main contributions of this thesis regarding the final approach to a moving landing platform are listed below, along with relevant related publications:

- Research and development of a new fusion filter that models the relative motions between a UAV and a moving platform through an improvement of a generic Singer model. Here, the relative accelerations have been modeled as a non-zero mean first-order stationary Markov process that makes use of the accelerations measured in the vehicle. This novel model is more effective than other approaches because it includes in the model most of the dynamics of the relative motion. This contribution has been published in (Alarcón et al., 2019).
- Research, development and testing of a new Attitude and Heading Reference System (AHRS) filter. This filter uses the Euler angular errors measured in the body frame and reduces the computational complexity of those filters that use the Euler angles directly. The measurement model of this filter has been built by using a new logic that indicates when it is possible to use the accelerometers and magnetometers for calculating the measurement vector. It also weights in real-time the filter matrices depending on the module of the acceleration vector. This novel algorithm has been called the TWA (Threshold and Weighted by Accelerations) AHRS.
- Research, development, and implementation of a new robust estimation method that makes use of a novel tether system that provides relative position measurements at 100 Hz. The developed navigation system does not depend on GNSS measurements and is able to calculate a relative vector with cm accuracy. The tether system has been designed, manufactured and integrated into a rotary-wing UAV in the framework of this thesis. This new Tether-based GNSS-free RelAtive NavigaTor has been called the T-GRANT module. This contribution has been published in (Alarcón et al., 2015), (Alarcón, Santamaría and Viguria, 2015) and (Alarcón et al., 2019).
- Research, development, and implementation of a new navigation and guidance system that switches between different sensors, fusion filters and guidance strategies depending on the UAV flight phase and on the equipment integrated. This contribution has been partially published in (Alarcón et al., 2015), (Alarcón, Santamaría and Viguria, 2015) and (Alarcón et al., 2019).

- Implementation and the first field experiments of a new estimation method that allows calculating a relative navigation solution at 100 Hz with sub-meter accuracy by using the measurements provided by a ground infrastructure based on a radio-beacon system integrated on a moving platform. The system model implemented in the navigator has been published in (Alarcón et al., 2019). This new Radiobeacon –based GNSS-free RelAtive NavigaTor has been called (R-GRANT) module. A video showing the final tests can be found in (CATEC, 2019).
- To the best of our knowledge, tests included in this work were the first worldwide field experiments with a tethered unmanned helicopter landing on a mobile platform by using the tether as its only positioning source. Contributions based on the navigation module has been published in (Alarcón et al., 2019). A video showing the final tests can be found in (CATEC, 2019)

2.2. EGNOS-based navigator for unmanned aerial systems

Global Navigation Satellite Systems have been the primary positioning source in most applications over the last three decades. However, applications are progressively requiring higher accuracy requirements and, at the same time, lower price levels. For example, in some remote sensing applications, it is usually necessary to achieve a level of accuracy below the meter to characterize and know what is the state of a crop accurately. In the User Guide for EGNOS application developers(ESA, 2009), it is presented that the expected performance of the Global Positioning System (GPS) signals uses to be between 7 and 13 meters. In order to improve and complement the GPS performance, in the last decades, numerous augmentation systems have been launched. EGNOS (European Geostationary Overlay Service) is a Satellite Based Augmentation System (SBAS) designed to complement the GPS positioning system improving the integrity and the positioning and timing service accuracy. The use of the EGNOS system jointly with GPS can provide a horizontal accuracy better than 3 meters and a vertical accuracy better than 4 meters at 95 % of the time.

In the field of the UAVs, several systems benefit from the EGNOS services. Most of them take advantage of the accuracy improvement that an EGNOS-capable GNSS

receiver provides. For example, in (Półka et al., 2018) the author combines the cellular technology, early Galileo services and EGNOS to localize the smartphones of potential victims. In this case, EGNOS is used for improving the accuracy of the GPS measurements and in this way it makes easier to find victims of natural or man-made disasters. In the mapKITE project (Molina et al., 2015), the Satellite-based Augmentation Systems is used as an accurate and safe low-cost navigator. Authors achieve position errors below the meter in both the horizontal and vertical plane.

In (Tamouridou et al., 2017), a multispectral camera is integrated on a fixed-wing UAV with a high-performance GNSS sensor which features EGNOS error correction, allowing the author to obtain sub-metric accuracy. The author of (Molina et al., 2011) uses a multi-sensor navigation scheme where it is fused a barometric altimeter, a magnetometer, a redundant inertial Navigation system and an EGNOS-enabled receiver. In this case, the objective is to interpret thermal images for person identification, and again EGNOS is used just for incrementing the accuracy of the GNSS solution. In (Molina et al., 2011), the authors used an EGNOS-enabled GNSS receiver with a low-cost inertial measurement unit to support the search component of Search-And-Rescue operations. The EGNOS corrected pseudoranges are used in this case in the mechanization differential equations to improve the positional solution.

All these works are focused on the fusion of the solution provided by their EGNOS- receivers with the solutions of other sensors. It is to say, the improvement on the accuracy of these systems is exclusively based on the corrections and calculations that their GNSS sensors perform internally. In these works, it is not possible to find a direct interaction between their estimation algorithms and the messages and services that EGNOS provides; for example, they do not make use of the SBAS integrity information in their navigation strategies. Besides this, in none of these research there are a relevant number of field tests that allows us comparing the real improvements that EGNOS provides with respect to the use of navigators that only rely on the GPS constellation.

Currently, there are not too many works regarding the use of the EGNOS integrity signals in the UAV navigation field. In (Colomina et al., 2008), the authors make use of the integrity information for calibrating and orientate their sensors. In this case, the corrections are performed in a post-processing stage, so it is not applicable to a navigation system that needs to perform its estimations in real-time.

As a summary, at the moment, commercial navigation systems do not exploit all the functionalities that EGNOS offers to the users. In this thesis, it has been developed, integrated and tested a new navigation system that makes use of the EGNOS information for improving the navigation and guidance performance of the UAV autopilot. Using the SBAS corrections and the integrity information, the position and velocity accuracy of the estimation process is improved with respect to the solution of those navigators that only rely on the GPS constellation. One of the novelties of this research is the use of the EGNOS infrastructure for improving the accuracy of the system and taking advantage of the integrity information in the estimation process. Through this information, also is achieved an increase in the robustness and safety of the guidance and navigation system in cases of GNSS degradation. Contributions about this topic have been published in (Alarcón et al., 2013). In addition, through this thesis, more than 30 flights have been performed for obtaining very specific and real telemetry. With this data, it has been possible to perform a relevant comparison of our new EGNOS IntegRity wEighted (EIRE) navigation algorithm and those that only use as positional source a GPS sensor. In that way, based on the results obtained from this field data, it has been possible to test and prove the benefits that the EGNOS infrastructure can provide to the autonomous navigation field. To the best of our knowledge, this is one of the most extense data sets logged with a UAV with the purpose of validating the benefits of the EGNOS constellation, making it very valuable to the European Spatial Agency.

2.3. Conclusions

This chapter presents a review of the state of the art regarding navigation systems developed for the autonomous landing of unmanned helicopters on mobile platforms and about the use of the EGNOS constellation in the current navigators.

On the one hand, regarding the autonomous landing over a mobile platform without the use of GPS, different technologies have been presented for the approach and final maneuver flight phases, highlighting their main advantages and limitations regarding their applicability to small RUAVs (Maximun Take Off Weight < 25Kg) in GPS denied scenarios. From this study, one of the main conclusions is that currently there are not systems that allow landing safely without using GPS sensors, without communication channels and with low-weight sensors. Although it is possible to find researches that offer a solution to this problematic,

their results are obtained from simulations or from experiments performed in very controlled scenarios where the landing platform is usually static. So that, through this section, it is justified the development and testing of two new navigators that make use of a radio-beacon infrastructure or a tether system for the approach and landing in a mobile platform.

On the other hand, it has been presented different navigators that make use of EGNOS for improving their accuracy. However, from the literature, it is possible to say that currently, in the framework of the navigation, the integrity information obtained from the new constellations is not used for improving the navigation performances. Taking this into account, it is concluded that it is possible to build a new navigator and guidance module that benefits from the use of the new possibilities that the EGNOS constellation offer to the different users.

3. AUTONOMOUS MISSION: INVOLVED SYSTEMS AND FLIGHT PHASES

In this chapter, it is presented the specific systems and coordinate frames that will be used throughout the thesis for the development of the autonomous navigation and guidance systems of the RUAV. Then, it is described the logical architecture implemented in the autopilot and the flight phases that will guide the vehicle from the take-off to the landing on a mobile platform.

3.1. Reference frames involved in the navigation and guidance system

In the majority of the robotic systems, the measurements of the different sensors are obtained in different coordinate frames and need to be transformed into a coordinate frame suitable for processing and navigating. A basic inertial navigation system involves at least four different frames. For example, for the inertial navigation system, the accelerometers measure the platform accelerations with respect to the inertial frame of reference. The accelerations are resolved in the instrumental frame of the accelerometers, so they need to be transformed into a platform coordinate frame by a fixed rotation matrix. Gyros measure the platform angular rates relative to the inertial frame of reference and resolve this in the instrumental frame of the gyros, which are transformed into angular rates in the platform frame by a fixed rotation matrix. From the gyro measurements, a rotation matrix is calculated which transform the accelerations in the platform-frame into the used navigation frame, where they are processed to determine the velocity and position of the navigation system. In Appendix B, all the reference frames and coordinate transformations that are relevant in this thesis are explained in detail. Below, it has been summarized the main reference frames used commonly for navigation purposes:

- Body frame (**B**) The body frame is a non-inertial coordinate system associated with the vehicle with the origin at its center of gravity. The x-axis points in the forward direction, the z-axis down through the vehicle and the y-axis completes the right-hand coordinate system. This frame will be denoted by the superscript b.
- Local Navigation Tangent Plane frame (**N**): This is an inertial coordinate system determined by fitting a tangent plane to the geodetic reference ellipsoid at a fixed point. This point is taken as the origin of the coordinate system. The x-axis points to the true North, the y-axis points to the West and the z-axis points up. This frame will be denoted by the superscript n.

However, due to the novel system developed in this thesis, a new coordinate system has been defined; the so-called tether-frame (T). This frame corresponds to the tether system developed along this thesis, which is presented in section 3.2.3. The tether frame (t): it is a non-inertial coordinate system associated with a cardan joint mechanism. It has its origin in the point where the tether is connected to the helicopter. The x and y-axes rotate with respect to the fuselage of the helicopter and the z-axis is always pointing towards the landing point. This frame is denoted with superscript t. This frame is shown in Figure 3-1 together with the body axes frame.

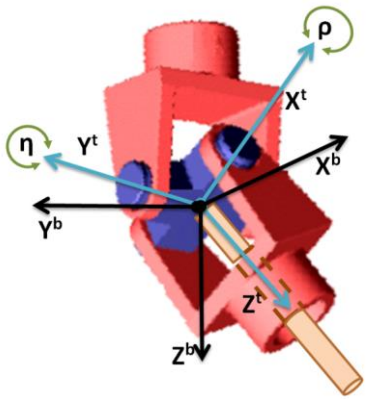

Figure 3-1: Tether frame representation

3.2. Sensors used in the navigation system

This section presents the sensors that have been used in a novelty way in this thesis for building the global and relative navigation systems. In addition to the systems explained in this chapter, in Appendix C, it is possible to find the rest of the sensors that compounds the navigators and their main characteristics and error properties, which are used throughout this dissertation for building the mathematical models of the fusion algorithms

3.2.1. EGNOS

From October 1994, when the US government offered civil aviation the possibility of using GPS free of charge, ICAO (International Civil Aviation Organization) began to study complementary systems to compensate certain disadvantages of GNSS in terms of accuracy (mostly in the vertical plane), integrity, continuity of service and availability. This work gave rise to the SBAS concept. The SBAS concept is based on the transmission of differential corrections and integrity messages for navigation satellites which are within sight of a network of reference stations deployed across an entire continent. A key characteristic of SBAS is that the data link frequency band and signal modulation are identical to those of GPS signals. In addition, the SBAS signal is broadcast by geostationary satellites so it is able to cover vast areas.

The European Geostationary Overlay Service is an SBAS constellation that complements the American GPS system (European Global Navigation Satellite System Agency, n.d.). It is composed by a number of navigation payloads on-board satellites in geostationary orbit, a ground-based network comprising a series of positioning stations and several control centers. As can be seen in Figure 3-2, all of these elements are interconnected

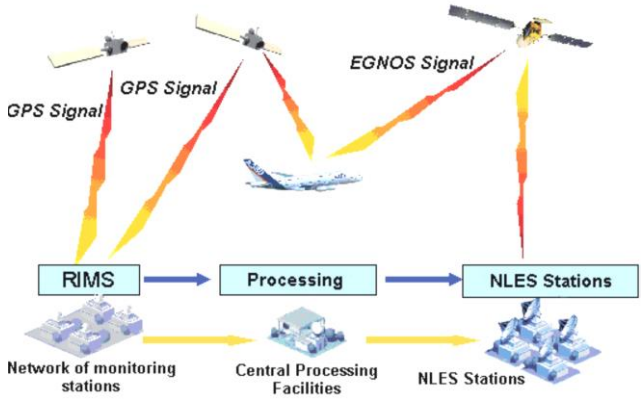

Figure 3-2: EGNOS Infrastructure

One of the main advantages of EGNOS is the improved accuracy in relation to a position calculated solely using GPS. This is possible by the broadcasting of differential corrections to GPS orbits, GPS clocks, and the ionosphere. Table 3-1 shows some of the corrections made by the EGNOS infrastructure in comparison with the GPS solution.

Error type	GPS	EGNOS
Orbit and clock synchronization	1 m	0,5 m
Tropospheric error	0,25 m	0,25 m
Ionospheric error	2 m	0,3 m
Receiver noise	0,5 m	0,5 m
Multipath	0,2 m	0,2 m
UERE (quadratic sum of errors - 1 σ)	2,31 m	0,83 m

Table 3-1: Comparison of the errors that affect GPS and EGNOS

Summarizing, Table 3-2 compares the expected performance of a navigator without and with EGNOS enabled. Here the horizontal accuracy corresponds to a 95% confidence bound of the 2-dimensional position error in the horizontal local plane for the Worst User Location and the vertical accuracy corresponds to a 95% confidence bound of the 1-dimensional unsigned position error in the local vertical

axis for the Worst User Location (European Space Agency, 2019)

Accuracy	GPS	EGNOS
Horizontal	7.1 m	3 m
Vertical	13.2 m	4 m

Table 3-2: Comparison of the positioning solution performance with GPS and EGNOS

Despite its accuracy, the reliability of data supplied by the GPS system is not guaranteed, for example, a malfunction of an atomic clock on-board a satellite may lead to very significant positioning errors. Caution is therefore called for, especially on critical applications like aviation. Moreover, the GPS system does not make possible to guarantee the position or time calculated by the user. In particular:

- The probability of loss of integrity of a GPS satellite is far greater than that which is required for the purposes of navigating an aircraft.
- In the event of system breakdown or malfunction (clock drift, broadcasting of erroneous data, etc.), pseudorange measurement can be biased from a few meters to a few kilometers.

Due to its system architecture, these errors may impact the user for several hours. GPS system errors or breakdown can also have serious repercussions for user safety if not detected in time and have the effect of restricting the number of possible applications. In particular, they make the system unsuitable for critical applications. It is with a view to overcoming the limitations of GPS with respect to integrity, that augmentation systems were developed. This is where EGNOS input will be a key in the modern navigation systems. Thanks to permanent monitoring of the GPS constellation, EGNOS detects distortions affecting the signals transmitted by GPS and prevent users from tracking unhealthy or misleading signals. It assigns a confidence level to the data transmitted to the user. These data are used by the GPS/EGNOS receiver to work out the protection levels. Basically, by using an SBAS system, the user obtains three types of information:

- satellite geometry information
- ranging information
- measurement quality-related information

The satellite geometry information comprises the ephemeris data of the ranging satellites from which the position of the satellites as a function of time can be

derived, and contains the satellite ephemeris data and the differential corrections to the satellite positions. The ranging information consists of three different contributions: the ranges, the clock and ephemeris corrections, and the ionospheric corrections. Finally, measurement quality information is provided in the form of variances that are related to the two types of corrections: the user differential range error (UDRE) for the ephemeris and clock corrections and the L1 residual user ionospheric range error (UIRE) for the ionospheric corrections.

The measurement flows from the ranging sources and the SBAS messages are asynchronous. Therefore, the SBAS information needs to be synchronised with the range measurements. For the ionospheric correction, rather than a time-synchronization, an ionospheric path correction is applied in which the received values are all transformed to relate to the user's position. For the scope of this thesis, it will be assumed that all these synchronizations have been performed and all parameter values relate to the same point in space and the same moment in time. The user equipment translates the differentially corrected ranges into a position solution by a weighted least squares algorithm. To determine the optimal position solution, measurements with a small noise variance will be more heavily weighted than more noisy measurements. The variances of the differentially corrected ranges are computed from the UDRE and the UIRE, combined with the local noise variance:

$$\sigma_i^2 = UDRE_i + UIRE_i + \sigma_{local,i}^2 \tag{3-1}$$

where:

- σ_i^2: variance of the position error distribution.
- $UDRE_i$: variance of residual clock and ephemeris errors in corrected range to the *i*th ranging satellite.
- $UIRE_i$: variance of residual ionospheric errors in corrected range to the *i*th ranging satellite.
- $\sigma_{local,i}^2$: variance of the local receiver noise and multipath.

This information is fed to the SBAS integrity equation, which describes the position error distribution obtained by using differentially corrected measurements where the validity of these measurements have been checked by the ground network in the absence of failures that are local to the user. It gives a simple means to assess the externally provided accuracy and the integrity performance. The equation is:

$$e_{pos} \sim N(0, \sigma_{pos}^2) \tag{3-2}$$

which means that the positioning error e_{pos} has a Gaussian distribution with mean 0 and variance σ_{pos}^2.

Integrity is specified in terms of the protection level, which is related to the probability that the alert limit may be exceeded. Depending on the satellite geometry, the GPS system errors or malfunctions may have serious repercussions for user safety, especially if they are not detected in time. To validate a GNSS based navigation systems, it has to be guaranteed that the position that the system provides has sufficient integrity. For the navigation system, it is required to deliver an alarm when the error in the derived user position solution exceeds an alarm limit (XAL). This warning must be issued within a given period and with a given probability or integrity risk. In contrast to GPS for which no guarantee is given, EGNOS broadcasts an integrity signal provide the possibility of calculating a confidence interval. This interval can give an alert when a GPS satellite malfunctions and is not advisable to use it for an application where safety is a major factor. Four parameters characterize integrity:

- Alarm limit;
- Protection level;
- Integrity risk;
- Time To Alarm (TTA).

Ideally, the user would like that the difference between the computed position and the true position (called the true position error or PE) to be smaller than the Alert Limit (AL). However, an alternative approach is required since it is not possible to know the true position, and therefore, the PE cannot be determined. So that, for each solution that the receiver gives in position, a predicted position error is estimated. This estimation is called protection level (PL) and it is performed for:

- Horizontal Protection Level (HPL): The Horizontal Protection Level is the radius of a circle in the horizontal plane tangent to the WGS-84 ellipsoid WGS-84(ESA, n.d.) Whose center if the true position of the vehicle. The importance of this parameter resides in that the horizontal position of the UAV is assured to be contained in this circle.

- Vertical Protection Level (VPL): The Vertical Protection Level is half the length of a segment perpendicular to the horizontal plane of WGS-84 ellipsoid. Its center is also the true position of the UAV and it describes the region certain to contain the real vertical position.

This calculation is based on the real-time processing of the data broadcast by EGNOS, which contains correction information for all the pseudorange measurements. These data arrive at the user position by many types of messages coordinated through Issues of Data (IOD): types of messages 1, 2 to 5, 6, 7, 9, 12, 24 and 25 provide the fast and long term corrections, and UDRE, those due to ephemeris and clock errors. Messages 18 and 26 contain ionospheric corrections and the Grid Ionospheric Vertical Error (GIVE). Finally, message 10 contains degradation parameters (José Santa, 2006). Once these values are available, the integrity algorithm must proceed to evaluate some mathematical expressions (they can be found described in (The Radio Technical Comission for Aeronautics., 2016) or (Bruckner, Graas and Skidmore, 2011)). Finally, these calculations are translated to the HPL and the VPL. If the predicted position error exceeds the stated protection level, an alarm must be transmitted to the user. This alarm must be received by the user within the Time To Alarm limit. Users of a GNSS system wishing to obtain a certain degree of integrity must state their needs in line with these four parameters for a given application.

Then, the EGNOS Integrity concept can be summarized in the following way:

The solution of navigation and the protection levels are calculated by the receiver. As the user is not able to measure the real position error, the user relies on this estimation to determine the system integrity (predicted position error). Next, the computed protection levels are compared to the alert limits that have been previously defined for the type of operation. Three situations are possible and are shown in Figure 3-3

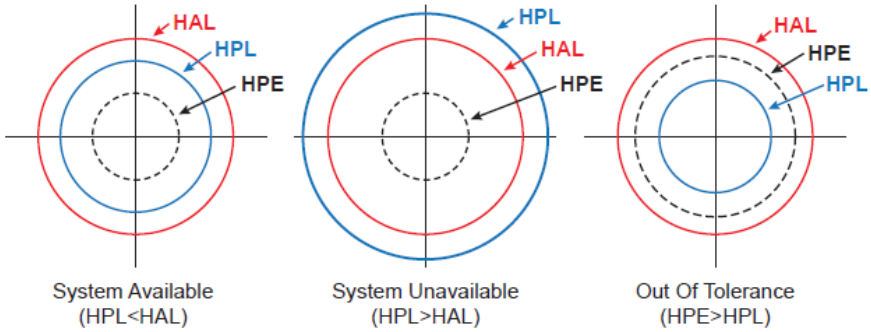

Figure 3-3: Possible situations with the integrity signal.

- If the computed protection levels are smaller than the alert limits defined for the intended operation, the system is declared available as the safety of the operation is ensured.
- If the protection levels are larger than the corresponding alert limits, the system becomes unavailable (the performance level provided by the system at that time is not sufficient to ensure the safety of the intended operation).
- If the error is not properly bounded by EGNOS (HPE>HPL), safety issues could arise if the error is larger than the alert limits defined for the intended operation. However, the probability of this situation is minimal by design.

3.2.2. Radio Beacon System

The Radio Beacon System (RBS) works on similar principles as Global Navigation Satellite Systems (GNSS): multilateration based on independent RF-based ranging signals. The user segment calculates its 3D position in a relative coordinate frame by measuring the distances to multiple ground stations, of which the positions are known in the ground segment's body-frame. The RBS ground stations can be installed on any fixed or moving ground base and its RF band is fully independent of GNSS. The measurement technique that this system applies has been specifically designed to determine the range between the ground stations' antennas and the

user segment antennas with highest accuracy in a local area.

With six ground segment units (GSU) integrated into the landing platform, it is possible to determine the position of a moving user segment relative to the ground segment. Figure 3-4shows the integration of the GSUs over the landing platform developed in this thesis.

Figure 3-4: Ground segments units installed over a landing platform.

The main airborne components regarding the RBS equipment are:

- RMU (Range Measurement Unit): Unit connected to two small-size airborne antennas. It computes the range measurements based on RF-signals between the two airborne antennas and the six antennas on the moving platform.
- PCU (Positioning Calculation Unit): processing unit that takes data from the altimeter and the RMU and fuses data in order to compute accurate relative positioning to the moving platform.
- Altimeter: sensor based on RF-signals which measures relative height to the ground/moving platform.
- Airborne Antennas: these antennas receive the signals emitted by the Ground Station Units on the landing platform.

It is important to note that both the RMU and the altimeter are operating in GNSS-independent frequency bands. Figure 3-5 shows the airborne segment equipment required.

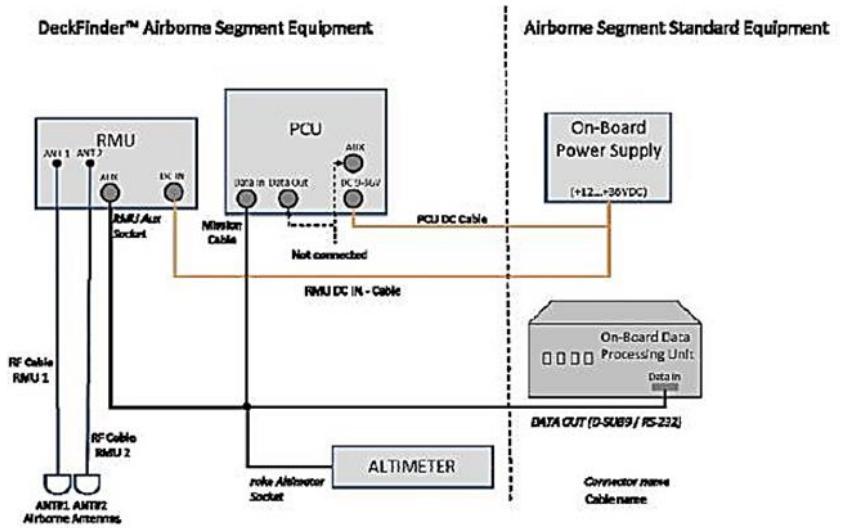

Figure 3-5: Airborne segment equipment for standard operation (AIRBUS)

The system underlies the same problematic as other multilateral positioning systems with respect to the constraints posed by the geometry formed between the roving (here airborne) element and the elements that send the positioning signals. I.e., the accuracy of the relative position information provided by the RBS is dependent on the relative ground segment ↔ airborne segment geometry. This effect is known as Dilution of Precision (DOP) in satellite navigation applications. In general, it holds that the horizontal position accuracy gets better when approaching the dedicated landing spot that is surrounded by the GSUs (Ground Segment Unit). The same holds true for the vertical position accuracy. However, the vertical positioning component is much more affected by the geometry conditions, even in medium vicinity to the Ground Segment. That's why the use of an altimeter is essential for providing independent height measurements as input data to the positioning software of the RBS and the navigator.

3.2.2.1. Landing Maneuver Constraints

As it has been described before, the expected RBS relative positioning accuracy is

strongly dependent on the relative geometrical state of the two vehicles, which can be expressed through DOP values. The smaller the DOP value, the better is the expected relative positioning accuracy. The operation radius strongly depends on the local system geometry determined by the GSUs. As an example, a rectangular ground station geometry with 8 m x 10 m side lengths would lead to an operating radius of 100 m. Consequently, a Vertical Take-Off and Landing (VTOL) UAV would use the RBS solely in the near field of the target landing platform, i.e. for the final approach and landing phase.

In a horizontal radius from 100 m to 50 m to the landing spot the navigation solution still relies on GPS, but in parallel the RBS relative position information is available. This allows for health monitoring and consistency checking of both system solutions. A flight height of at least 20 m is desirable. At a horizontal distance to the landing spot of approximately 50 m it has to be decided whether the final approach can be started or not. This decision is based on the previous monitoring phase. During the final approach and landing the relative position information provided by the RBS is used for navigation and the GPS based information can be ignored.

Some flight paths are better suited than others due to the resulting helicopter - ground infrastructure local geometry. The optimum flight height has been derived from the criterion of minimizing the PDOP (Positional DOP) value. The smaller the PDOP value, the better the expected relative position accuracy. The three-dimension position accuracy gets continuously better when approaching the dedicated landing point.

In Figure 3-6, it is shown that the optimum glide slope angle from a RBS performance perspective, when no altimeter data is available, is approximately 40°. The increase of the optimum flight height and the PDOP close to the dedicated landing spot at (0,0,0) results from the exclusion of altimeter data. If three-dimensional relative position information is required when the airborne segment is close to the x-y-plane of the RBS ground segment (assumption: all GSUs are in the same plane), altimeter data has to be provided to the RBS PM module.

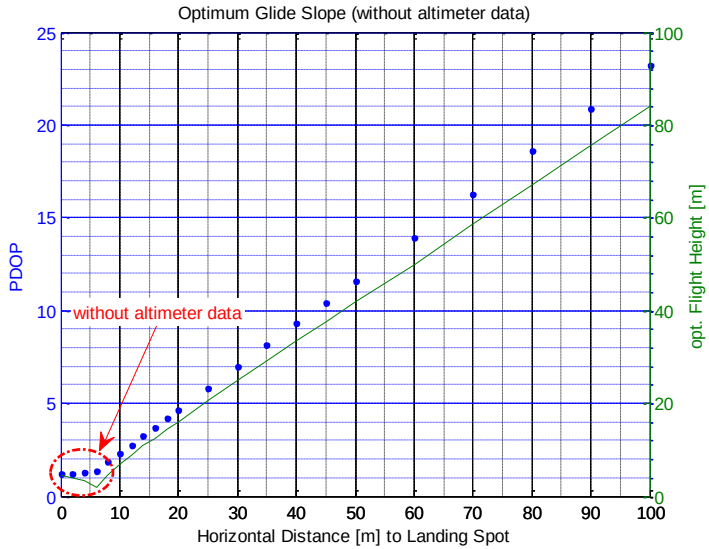

Figure 3-6: Optimum Flight Height (when altimeter data cannot be used)

Note, that the previously presented glide slope considerations are only relevant if the altimeter data cannot be used during the whole flight path. As shown in Figure 3-7 (top) the PDOP value is dominated by the vertical component (VDOP) if no altimeter data can be processed. Then glide-slope angles of 3° do hardly make sense except from the direct vicinity to the landing point. As soon as altimeter data can be processed by RBS, the PDOP value is dominated by the horizontal component (HDOP), see Figure 3-7 (bottom). Then the operation area of the RBS can be extended significantly independent from the actual glide slope angle. If only the horizontal relative position information is relevant, it is also possible to extend the RBS operation area without the need of introducing an altimeter. Even if altimeter data can be processed by the RBS during the whole flight path, it holds that the relative positioning accuracy gets the better the closer the airborne vehicle is to the dedicated landing point.

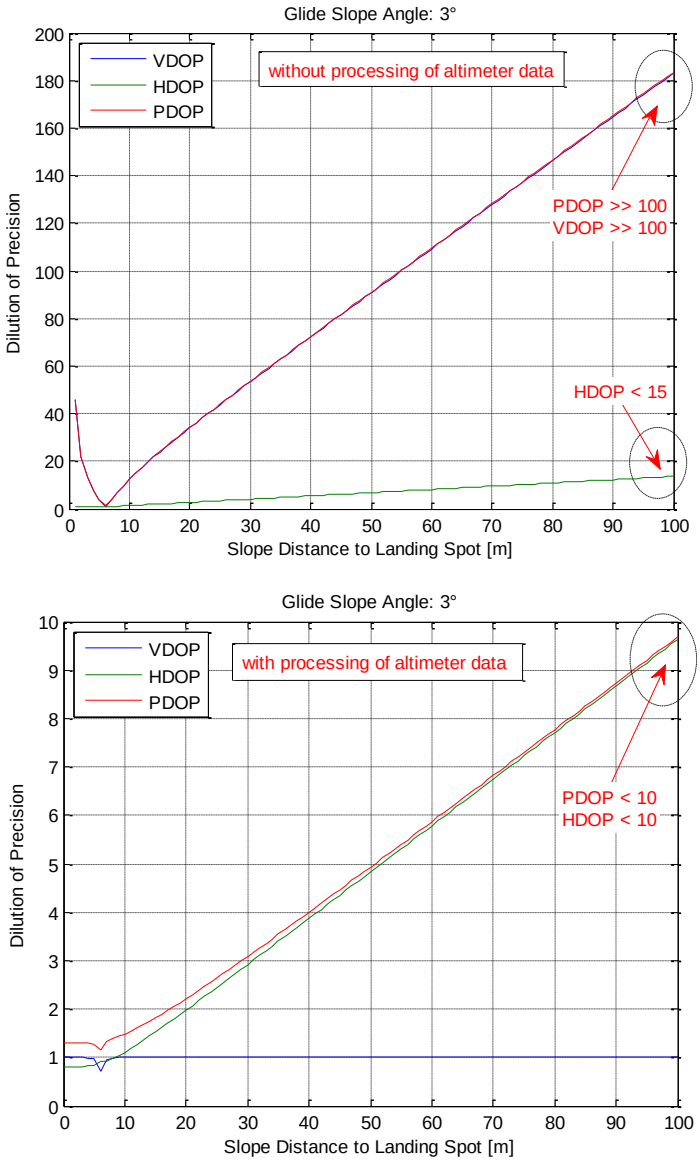

Figure 3-7: PDOP without altimeter (top) and with altimeter (bottom)

In this work, and after several tests, it was decided to configure the RBS to work with the altimeter.

3.2.3. Tether System

Through this thesis, a specific cardan joint device has been developed (see Figure 3-8). This device is similar to those used for slung loads transportation by cooperative helicopters in (Robotics, n.d.). The device consists of 2-axis coupled cardan joints equipped with magnetic encoders attached to each axis. This system allows estimating the angles between the tether and the helicopter frame in terms of the two successive rotations of the cardan joint. Additionally, the device has a load sensor to measure the tension level of the tether and a tether release system for safety purposes. This safety mechanism produces the separation between the helicopter and the tether and it can be directly activated from the safety pilot radio in case of emergency.

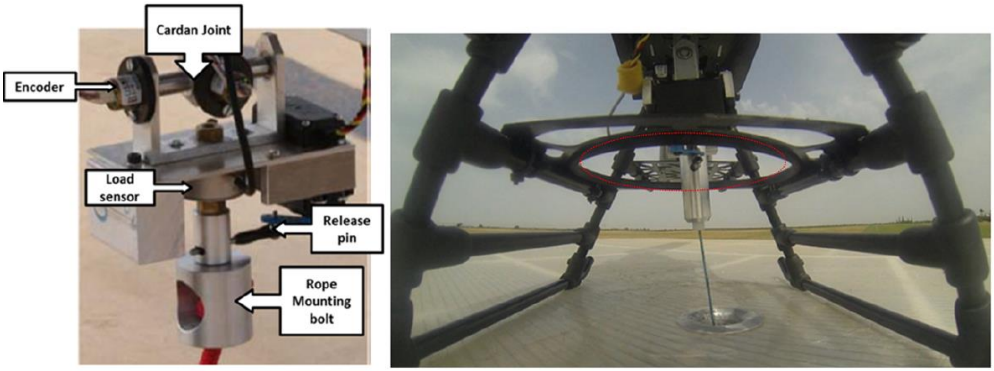

Figure 3-8: Cardan sensor integrated into LOGO 800 with the tether attached.

In order to avoid dangerous situations with the cable, a protective frame (indicated with red dots in Figure 3-8) has been integrated for assuring that the tether does not reach the skids of the helicopter, limiting in that way the maximum cardan angle measured and the maximum distance under the estimations are correct. These constraints are used in the guidance block to limit the relative references that are provided to the controller. In that manner, the autopilot is able to maintain always the helicopter in the range where the estimations are accurate.

Figure 3-9 shows the relation between the different variables that define the envelope of the cardan angle device.

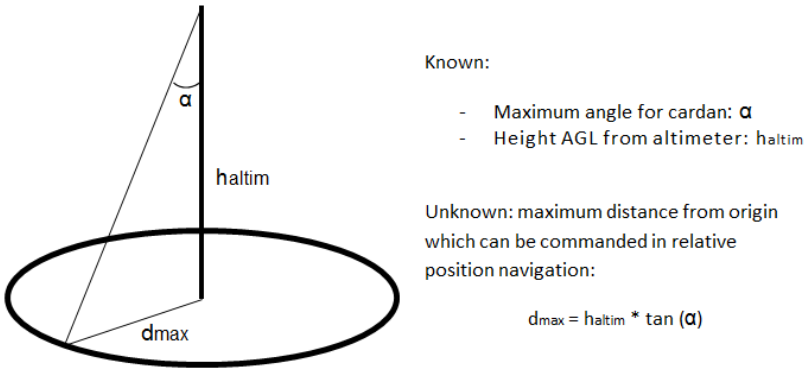

Figure 3-9: Envelope of the cardan angle device.

3.2.4. Landing Platform

The landing pad structure has a dimension of 3 x 3 meters. It is composed of three detachable transparent reinforced panels. An electric engine, located in the base, moves the spindle and transmits its rotational movement to vertical movement through a scissor pattern structure. This allows the platform to perform movements in the vertical axis with amplitude oscillations up to 4 meters and a maximum vertical velocity of 0.5 m/s. The goal was to replicate qualitatively the motion of a ship's deck under sea conditions below sea 5 (following the Beaufourt scale). Appendix A presents the assumptions taken into account and the limitations regarding the vertical motion capabilities of the landing platform for replicate the behavior of a ship's deck under different weather conditions.

The control of the platform is commanded via a Radio Control (RC) transmitter, a Programmable Logic Controller (PLC) and a communication link. In that way, the vertical movement of the platform can be remotely commanded in real-time during the operation. In Figure 3-10, the different components of the moving platform are shown

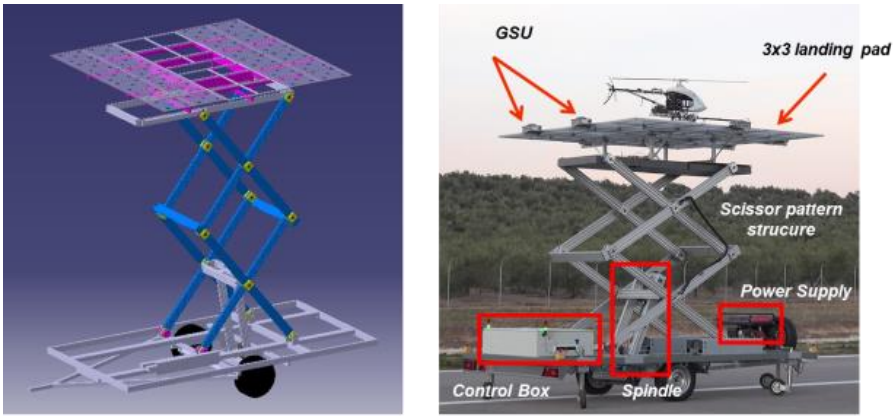

Figure 3-10: Catia design of the moving platform (left) and the real platform built in CATEC (right)

3.3. Flight phases of an autonomous mission

A typical mission of a RUAV uses to be split into several phases. The helicopter takes-off from its base, it flies to a specific area to perform its mission (generally by using global coordinates). Once the mission has been completed, the RUAV starts the approach to the landing area. Finally, when the helicopter is over the landing location, it starts the descent until it lands.

The majority of the navigation strategies employed in autopilots are based on fusing the GNSS information with the navigation solution calculated through the accelerometers and gyros of the inertial measurement unit integrated into the vehicle. This strategic is generally valid and a good approach for the taking-off and waypoint navigation phases, where the positioning in absolute coordinates provides enough accuracy for performing the different maneuvers. However, for those phases that are critical from a safety point of view, as could be a landing maneuver over a moving platform, it will be required a more robust navigation strategy based on more accurate sensors. In addition, if it is added that some of these critical phases are carried out in non-GNSS friendly environments, to have alternative sources of positioning not dependant on the satellite constellations

becomes crucial in order to increase the robustness of the system.

In this work, it has been developed a novel scheme that combines different strategies for the guidance and navigation of a rotary-wing UAV. The decision about the strategy to use is taken by the autopilot's logic. Figure 3-11 presents the architecture of the autopilot system developed in this thesis

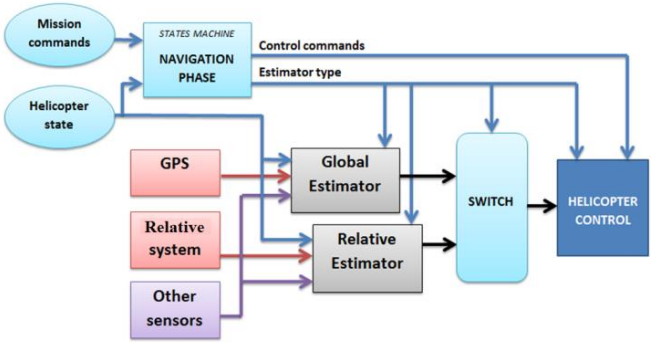

Figure 3-11: Guidance, Navigation and Control architecture

The architecture shown in Figure 3-11 is organized in the following functional blocks:

- Navigation/Estimation system: It is in charge of fusing the information of the different sensors onboard the UAV in order to obtain the position, velocity, and attitude of the helicopter. In this case, this block is composed by two different modules: the so-called global navigator that makes use of the GNSS constellation in its estimation algorithm, and the relative navigator that uses the relative positioning system as positioning sensor.
- Guidance block: It implements the logic that guides the UAV during the different phases of flight by providing the references to the controller. It is in charge of the generation of the trigger signal that makes the change between the global and the relative navigation strategy and vice-versa. This change is triggered depending on the phase of flight and the state of the different sensors that are taking part in the operation.
- Controller block: It implements the control algorithms that generate the commands signals for the actuators.

Figure 3-12 shows the scheme of the different strategies implemented in the

guidance and navigation algorithms. The decision about the strategy to use will depend on the current phase of the flight, the distance to the landing platform and the equipment integrated onboard the UAV.

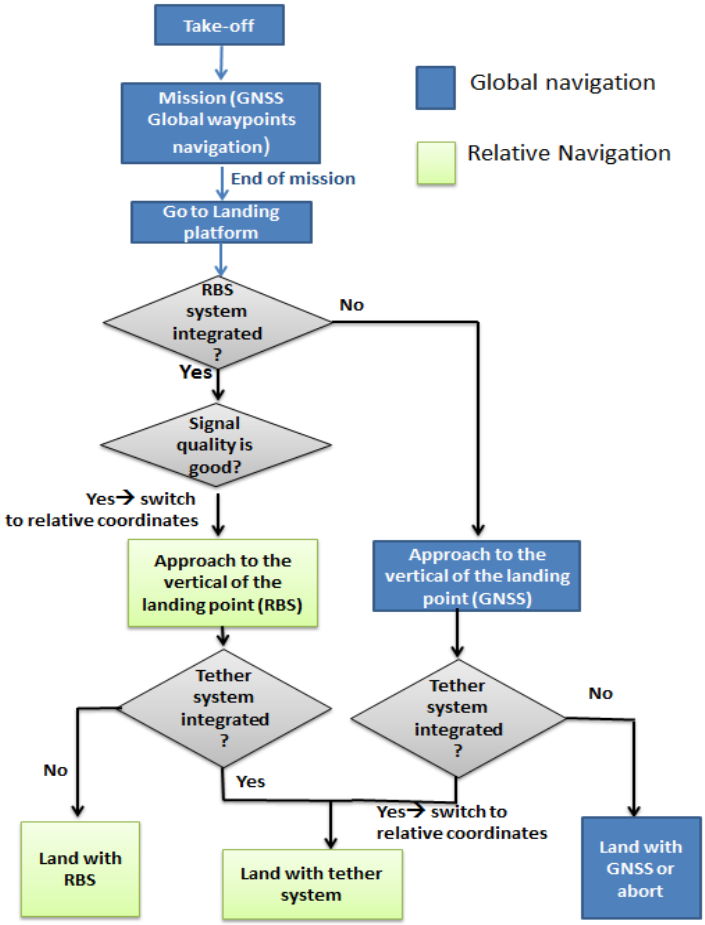

Figure 3-12: Operation strategy

The first configuration presented in Figure 3-12 comes into play during the takeoff, hovering and waypoint navigation phases. In these stages, it is usually possible to accomplish with the mission objectives without centimetric accuracy in the navigational solution. For these cases, the estimation strategy is based on fusing the GNSS solution with the inertial sensors, so the guidance can be carried out in global

coordinates.

Once the UAV is close to the landing platform and the autopilot receives the approach command from the ground control station (GCS), the vehicle enters in a new operational phase. For the approaching to the landing point, it is advisable to use a system more with more accuracy than the GNSS and, if it is possible, that be able to provide information about the distance to the landing position. In our approach, if the radio-beacon sensor is integrated into both the helicopter and the landing platform; the navigator will be able to obtain directly with sub-meter accuracy the relative positioning information between the vehicle and the landing platform. Relative coordinates will allow guiding the UAV to the vertical of the landing point without the need for external guidance commands. However, if this sensor is not integrated on the helicopter or if it is not working correctly, the autopilot will have to perform the approach by using the absolute coordinates (GNSS sensor) and also it will be necessary to receive guidance commands from the GCS or external information about the location of the landing point.

Once the RUAV is over the landing platform, three different cases are possible.

- If the tether device has been integrated on the helicopter, the estimator will make use of the measurements obtained from this device to calculate accurately the relative position and velocity of the vehicle with respect the landing point. In this thesis, the use of this sensor is the best strategy possible for the landing phase because it has proved to be the most accurate among all the sensors integrated into the UAV. Furthermore, the tether strategy also improves the stability of the system and the robustness of the controller during the descent of the helicopter (this is demonstrated in (Sandino Velásquez, 2016)).
- In the cases where the rope is not equipped, but the RBS system is integrated into the UAV, this will be the sensor chosen for performing the landing procedure. In this case, it is important to note that the accuracy of the RBS is around one meter, so the landing platform should be prepared for a landing procedure with this margin of error (for example a landing platform of several meters).
- For the last, the worst case is that in which the navigator only can rely on the GNSS sensor measurements. In this situation, the operator should decide if it is safe to land or it is better to abort the mission and perform

this operation in a different location where the GNSS solution is enough for performing the maneuver safely.

3.3.1. Operation phases for landing in a moving platform

The UAV landing guidance block is the logical module that contains the state machine that guides the helicopter during the last phase of the operation by using the information provided by the different positioning systems integrated into the vehicle. Figure 3-13 shows the state machine that manages the different phases of flight.

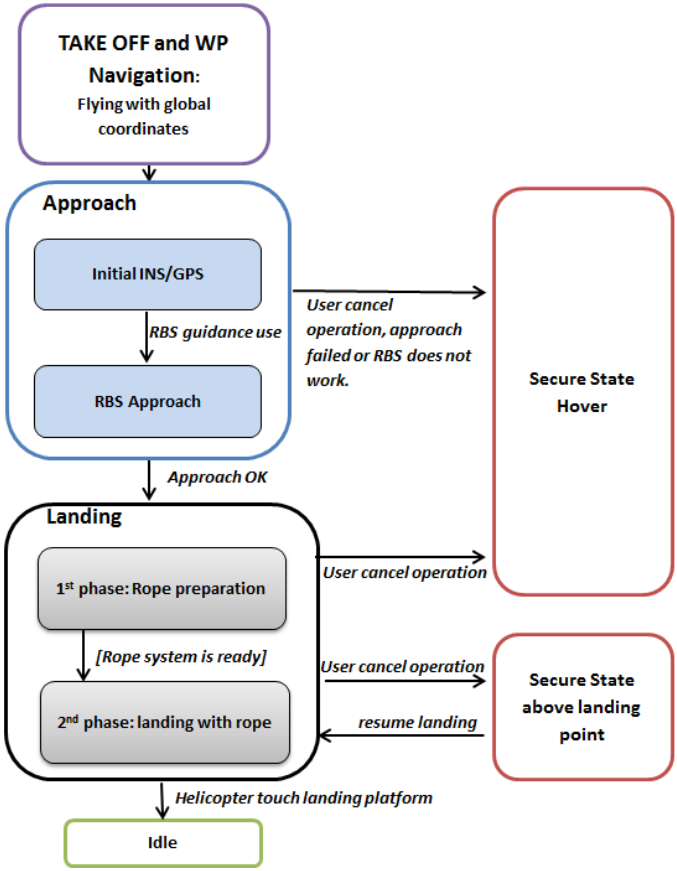

Figure 3-13: State machine for the autonomous landing phase

Below, the phases presented in the Figure 3-13 are explained in detail.

Take Off and Way-Point navigation

For the take-off and those operations where the UAV navigates following global coordinates, it has been developed a logic based on the integrity information provided by EGNOS. In general, autopilots enter in an emergency state when the GPS sensor fails In these cases, the aerial vehicle enters in a degraded operation mode where the most usual procedure is to hover and wait for the satellite signals recovery. In those cases where the GPS is not recovered, the vehicle starts a landing procedure, or the remote pilot takes control of the aircraft. This degraded behavior has a high intrinsic risk due to during the hover maneuver, if not positional information is managed by the autopilot, the control of the aircraft is usually performed by commanding a roll and pitch angles of zero degrees and trying to maintain the altitude calculated with a barometer. This kind of control usually causes the UAV moves in the longitudinal axis, because any external force (usually the wind) can push the vehicle without the autopilot can realize this behavior. Besides, if the GPS is not recovered and the UAV starts the landing procedure, the descent can be carried out in any place, which is a risk for the platform and the surrounding.

Using the EGNOS integrity information, it is possible to anticipate this situation of completely loss of the satellites and to know in every moment which is the confidence level of the solution that the sensor is calculating. This information allows differentiating between four possible situations that can be mapped in navigation modes of the UAV:

1- Signals are providing reliable values, and therefore, the solution of the GNSS sensor is expected to have good accuracy. This reliability has a close relationship with the value of the protection limits.
2- The sensor is not receiving information from the EGNOS infrastructure, so the corrections cannot be performed, and the protection levels are not calculated. In this case, the GPS is used just for positional purposes, as it is done in a standard navigator.
3- The GPS constellation state has poor quality, and the protection levels are higher than limits imposed in the autopilot logic. In this case, GPS

measurements are not accurate and it is possible that the solution gets worse with time, even losing the signal coverage completely.

4- The receiver does not receive enough satellites and is not able to calculate a solution.

Figure 3-14 presents the scheme of the states machine implemented for the global navigation phases. Here, it is shown how the EGNOS integrity information can be used and the transitions between the different states. Depending on these states, the autopilot is programmed to perform different actions. In this case, the protection and alarm levels are user parameters managed by the logic of the autopilot. In addition to the protection levels, the guidance logic also manages the information about the number of satellites in view and its quality, however this information is redundant and uses to be implicit in the integrity information.

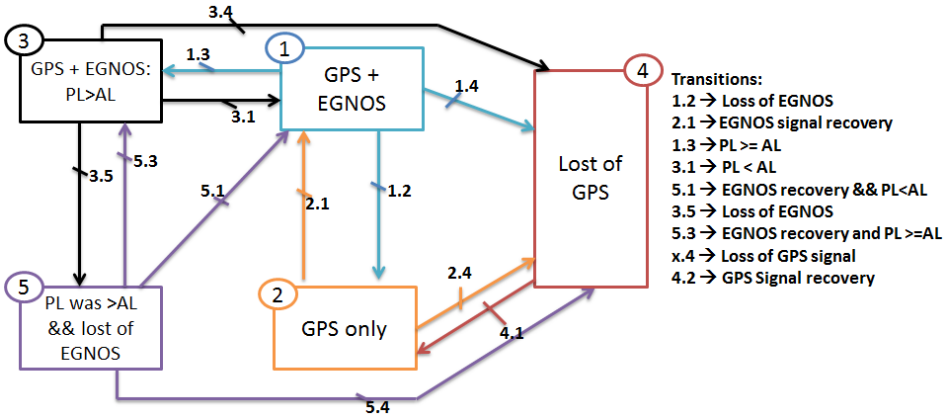

Figure 3-14: States Machine Using EGNOS

The behavior of the autopilot can be summarized as follows:

- In the states 1 and 2, navigation is allowed. However, the number of satellites is monitored and if it is lower than a programmed threshold, the autopilot goes to the state 3 or 4.
- In the states 3 and 5, the quality of the solution is not accurate enough. In this case, the UAV is commanded to perform a "return to home" procedure, preventing to enter in a lost of signal state.
- In the state 4, the GPS signals are lost. The only procedure possible is the indicated previously. The UAV is commanded to hover and wait for

recovering the GPS signal. After several seconds, if not enough satellites are received for calculating the position, the UAV starts a landing procedure or the remote pilot takes control of the platform.

The use of the EGNOS capabilities in this thesis also allows the improvement of its geo-fencing capabilities. Geo-fencing concept aims to use geographical information to establish boundaries or fences, to prevent hazardous UAV flights in sensitive areas. This is used to limit flights near airports, or above certain altitudes. The navigation positioning solution based on EGNOS, provides the means to determine better whether the UAV is crossing a geo-fence by assessing not only the position computed but the protection levels. Protection levels describe the region assured to contain the UAV, and it is based upon the error estimates provided by EGNOS. Hence, even if the UAV calculated position is outside a sensitive area, the protection levels may lay inside, meaning that UAV may be really crossing the geo-fences (see Figure 3-15). Here the behavior programmed is the following, if the HPL crosses a geo-fence, the UAV stops waiting for a new route. After a time, if this new route is not commanded, the aircraft perform a return to home procedure.

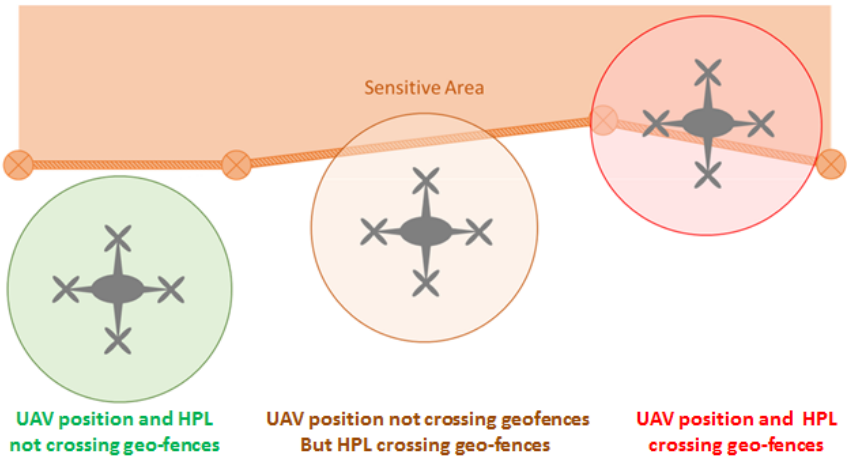

Figure 3-15: RPAS horizontal protection levels interference with geo-fencing.

Approach using INS/GNSS

In this phase, the position and velocity solution used in the controller are the provided by the UAV global INS/GNSS-based estimator. The RBS relative data is used to calculate the ship position by subtracting the relative to the absolute position. In this case, the relative measurements are used only for guidance purposes; the navigator continues estimating the global state vector.

$$\text{Ship position} \approx \text{absolute position} - \text{relative position} \tag{3-3}$$

The desired position commanded to the controller is the landing platform position with an altitude offset of 30m over the ship deck. By using this approach, the UAV helicopter starts to follow the ship and gets a velocity approximately equal to the ship velocity. Figure 3-16 shows the approach maneuver using UAV estimator absolute states:

Figure 3-16: Approach maneuver using UAV estimator absolute states

Approach transition to RBS

When the UAV guidance block detects that the relative velocity module is smaller than a threshold value (for example 1 m/s), the module generates a signal that changes the position and velocity states from absolute to relative coordinate systems, and also is used by the UAV controller to initialize the integrators of its control loops. At the same time, the position reference is changed for keeping the same position error than before the change in the navigation algorithm.

Approach using RBS

Once the relative architecture is running, the position references in the horizontal plane are changed to zero. This means that the horizontal coordinates of the touchdown point are sent to the UAV. The vertical reference is set to 10 meters over the landing point and it is added a height increment proportional to the module of the horizontal distance of the helicopter multiplied by the optimal glide slope angle $\propto_{\text{opt}}$ (this angle has been calculated based on the different tests performed along this thesis).The vertical reference is calculated using the following equation:

$$z^* = 10 + \propto_{\text{opt}} \sqrt{x_{rel}{}^2 + y_{\text{rel}}{}^2} \tag{3-4}$$

Figure 3-17 shows the approach maneuver using RBS relative states:

Figure 3-17: Approach maneuver using RBS relative states

Once the helicopter is over the platform at 10 meters approximately, it is possible to start the landing maneuver by using both the tether or the RBS system.

a) Landing maneuver using the tether:

This state covers the preparation of the rope system and the descent with the rope tethered to the moving platform.:

1st phase (rope preparation)

While the helicopter hovers above the landing point (end of the approach phase), the guiding-tether is deployed by the helicopter and locked into the device installed in the landing platform for controlling the tether tension and velocity. Figure 3-18 depicts some of the different actions to be carried on in order to prepare the tether.

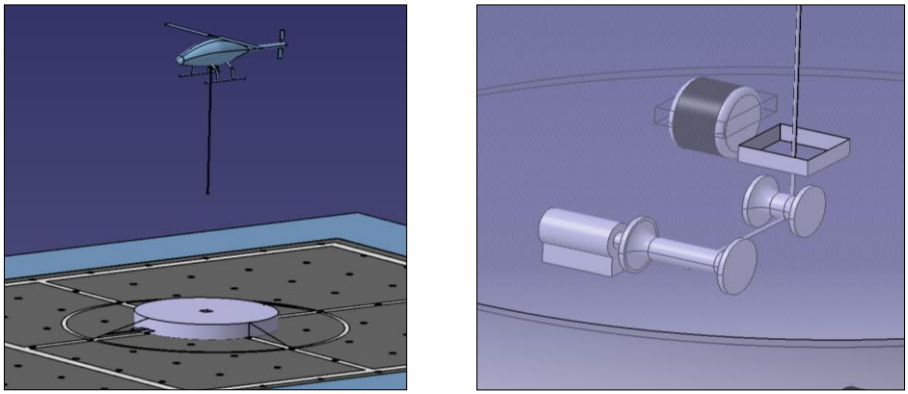

(a) (b)

Figure 3-18: Rope preparation for landing maneuver : (a) Tether deployment during 1st phase (rope preparation) and (b) Detail of device onboard landing platform for tether control

2nd phase (landing with rope): "UAV guidance controller (tether mode)":

In this phase, the tether itself is used as a guiding element. More precisely, the pulling movement of the tether commands a decreasing altitude reference whereas longitudinal and lateral references are given by the corresponding coordinates of the tether's fixed point at ground.

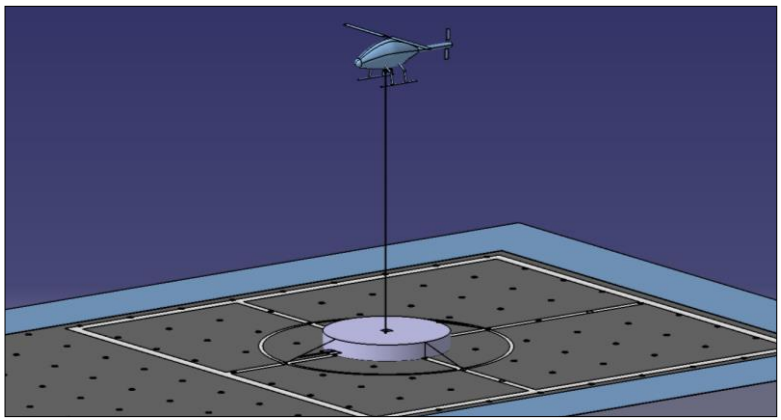

Figure 3-19: Tether is pulled during 2nd phase (landing with rope)

b) Landing using RBS

If the sensor chosen for landing is the RBS, the landing phase is as follows. When the helicopter is at a distance of approximately 10m over the landing point, the desired altitude is changed to 3m below the ship deck height. Once this altitude is reached, the helicopter starts the final descent up to land. *Figure 3-20* shows the final descent maneuver using RBS relative states.

Figure 3-20: Final landing descent maneuver using RBS relative states

Idle:

When it is detected that the landing skids of the UAV have finally touched the landing platform, an idle signal is sent to the autopilot for stopping the engine. This state finish when the rotor is stopped.

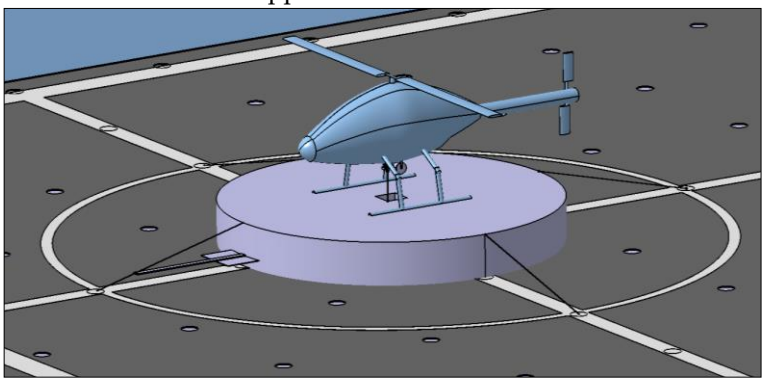

Figure 3-21: Helicopter standing on the landing platform (Idle phase)

Emergency states:

Secure state hover from RBS:
The sequence previously described is used when no failure is detected by the UAV RBS supervisor. If this module detects a failure in the RBS signal, a secure state hover is activated. This state implies a safe an imminent transition to the absolute reference controller, which is based on the INS/GPS positioning solution provided by the global estimator. Additionally, a safe absolute position reference over the current UAV position is sent in order to stop the translational movement of the UAV and let the moving platform get away.

Secure state hover from the tether:
In this emergency state, the rotary wing UAV flies in a controlled way towards a hovering location far from the moving platform. This state is triggered in case of degradation on tether measurements reliability/consistency during the landing approach. In this situation, the UAV supervisor sends a signal to the guidance controller that releases the tether from the UAV.

Secure state above landing point:
This state is triggered when the rotary-wing UAV is performing the last maneuver for landing. In this case, the helicopter is commanded to ascend to a safe altitude and to follow the platform in the horizontal plane if possible. In other cases, the rope is released of the helicopter and it remains in a hovering state.

3.4. Conclusions

This chapter starts with a presentation of the main systems and coordinate frames used during this thesis. It is focused on the key technologies used for the new navigators: EGNOS, the tether system, and the RBS.

From the EGNOS presentation it is possible to conclude that, apart from the accuracy improvements that this sensor provides to the GPS constellation, the protection levels calculated from this sensor can be used for improving the performance o the navigator and guidance modules.

From the RBS system, it is explained that it can work with two different altitude

measurements, the inner calculations or the measurements obtained externally from an altimeter. After several tests, it is checked that as soon as altimeter data is processed, the PDOP value is dominated by the HDOP and the operation area of the RBS can be extended significantly independent from the actual glide slope angle. Based on this results it was concluded that for obtaining the best results, an altimeter would be used for this thesis.

Regarding the tether system, it has been shown that limiting physically the angle to the cardan sensor, dangerous situations with the cable can be avoided and false measurements can be detected (when the maximum angle is achieved). In that way, it is concluded that by installing a protective frame and operating always below the limit angle, the measurements will have the best accuracy possible.

This chapter also presents the flight phases that compound an autonomous mission and the Guidance, Navigation and Control strategy that follows the autopilot developed in this thesis. The main conclusion is that if the different strategies and technologies presented in this thesis are combined, it will be possible to accomplish with all the flight phases and their peculiarities. In this case, the conclusions are that for those phases that do not require cm level of accuracy, the best strategy is to use a navigator based on global coordinates. On the other hand, in the phases that require higher accuracies (in this case the approach to the mobile platform and the landing maneuver), the best strategy is to switch from the global to a relative navigation strategy. Once the UAV is in the landing phase using the relative navigation mode, based on the accuracy results obtained from different tests, it is concluded that if it is possible to use the tether, this will be the chosen sensor for performing this maneuver.

4. EGNOS-INTEGRITY-WEIGHTED GLOBAL NAVIGATOR

Navigation could be defined as the determination of the position and velocity of a moving vehicle. The three components of position and velocity describe the translational motion of the vehicle in the chosen coordinate axes. If the attitude of the vehicle is added to this six-component state vector, it is possible to know the complete state of the vehicle. The basic navigation strategies, from which it is possible to build more sophisticated and accurate systems, could be categorized into three types:

- Dead-reckoning navigation systems: Beginning in a known initial position, and based on previous measurements, these sensors allow deriving their state vectors.
- Absolute navigation systems: The state vector is measured without any knowledge of the past measures. It is possible to differentiate between two systems:
    - Radio systems: A group of transmitters sends data that allows the receptors to compute its position relative to the positions of the different transmitter stations, which are known accurately.
    - Celestial systems: The elevation and azimuth of the celestial bodies are measured relative to the land level and North.
- Mapping navigation systems: These systems are able to observe and recognize images, features, profiles, etc, and to compare these with a stored database.

Departing from these systems, more complex and accurate navigation systems can be built through sensor fusion strategies. Before the deployment of GPS, dead-reckoning computations used to be the core of every navigation system. If three gyroscopes and three accelerometers are used in the navigation algorithm, it is possible to measure the changes in the direction and velocity of a body. The main

problem is that the measures of these sensors have to be integrated in order to obtain the vehicle position, which implies errors that tend to increase with time. In the past, inertial sensors used to be expensive and the size and weight of them were high for their implementation in robotics systems with restricted payloads. Recently the progress in micro-electro-mechanical systems (MEMS) technology enables a complete inertial unit to be built on a chip, composed of multiple integrated MEMS accelerometers and gyroscopes. The characteristics of MEMS, such as immediate start-up time, low power consumption, light-weight, and low cost, offers the opportunity of applying inertial navigation for a wide variety of new applications.

In the navigation field, it is essential for both manned and unmanned robotic systems to maintain an accurate track of the position, velocity and the attitude of the vehicle. Unfortunately, neither cheap dead reckoning sensors nor absolute sensors can fulfill these requirements in stand-alone mode. This is the main reason why sensors are fused, looking for the improvement of the navigation accuracy by taking advantage of the nature of the different systems in use. With the arrival of global systems as the GPS, architectures based on fusing different sensors began to be the heart of the navigation systems. For a long time, the integration of the INS, GPS, and other sensors has been a common field of study for many researchers. As a consequence, lots of navigation systems have been developed and integrated into all types of vehicles.

Currently, the principles of inertial navigation are well understood. So the challenge, when working with the current generation of low-cost MEMS instruments, is to develop a robust navigation capability that can deal with the large instrument errors that are experienced with these low-grade inertial sensors. Then, although MEMS INS/GPS systems constitute an increasingly attractive low-cost option, it is essential to work on their performance.

With the launch of the SBAS systems, an improvement of the accuracy and the integrity is available to their users. Currently, the majority of the GNSS receivers have the option of using the EGNOS constellation. In that way, through a GPS-EGNOS/INS integration, it is possible to obtain a better performance than the achieved by those navigators that do not implement the augmentation system services in their algorithms.

In this section, it is presented the EIRE (**E**GNOS **I**nteg**R**ity w**E**ighted) global

navigator. This is a new navigation system that makes use of EGNOS and its integrity capabilities in a novelty way. This approach improves the estimation solution accuracy in comparison with those architectures that do not make use of the different SBAS services in their estimation algorithms. Here, one important innovation is the use of the protection levels obtained from the integrity services to adapt the performance of the estimation filter in real-time during an operation.

4.1. Integration Strategy

As it was described in section 3, the EIRE global navigator developed in this thesis is used during the take-off and global waypoint navigation phases of the RUAV. The purpose of this system is to combine the data of the GNSS, INS and additional sensors in an optimal way to obtain a navigation solution with both higher update rate and smaller position error than the standalone sensors. Figure 4-1 presents the advantages of using a combined strategy for obtaining the vehicle's position.

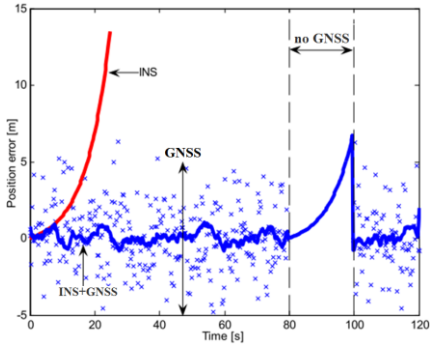

Figure 4-1: Position errors of GPS, INS and combined INS/GPS (Bijker's, 2006).

In most cases, the fusion of GNSS/INS uses to be performed by an Extended Kalman filter. This algorithm is often implemented in a complementary form where the estimates states usually correct the position, velocity, attitude and the IMU sensors errors(Ding, 2008). The filtering outputs use to be fed forward to the INS navigation outputs to generate the navigation solution and they are also fed back to the INS sensors in order to calibrate their errors. The complementary integration structure is commonly used because it provides a convenient reference trajectory that makes easier the linearization of non-linear dynamics. Moreover, it estimates only the error components of the integrated system and in that way, reduces the

tracking dynamics. This is possible because the error components use to change much slower than the direct positioning dynamics(Brown and Hwang, 1997).

In literature, it is possible to find multiple integration architectures that provide combined navigation solutions (Falco, Pini and Marucco, 2017). The differences between the different implementations use to be based on the type of information that is shared between the individual sensors and how this information is managed. GNSS/INS integrated system may have a variety of structures. However, in practical implementations, two main approaches predominate over the rest: the loosely coupled (LC)(Solimeno, 2007) and the tightly coupled (TC)(Petovello, 2003) schemes. Both strategies can be open-loop, where the estimation of the INS errors does not interfere with the operation of the INS, or closed loop, where the sensor errors are compensated within the calculation procedure of the INS mechanization algorithm.

In a loosely coupled integrated system, the GNSS receiver runs internally its own Kalman filter (GNSS filter). This filter calculates the user position and velocity by processing the pseudorange and Doppler measurements measured by the sensor chip. Under this approach, the differences between the INS and GNSS calculated positions and velocities, are used as measurements for a second Kalman filter (INS filter). This second filter is in charge of providing estimations of all the observable INS errors, which are consequently used to correct the IMU raw measurements and to compensate the INS outputs. Figure 4-2shows a typical loosely coupled scheme (Solimeno, 2007)

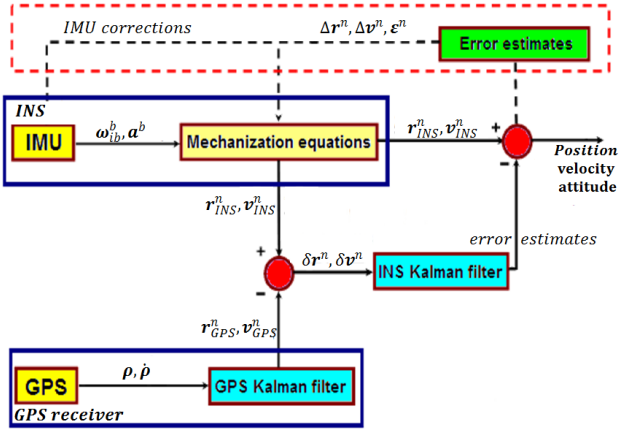

Figure 4-2: A GPS/INS Loosely coupled integration scheme.

In Figure 4-2, $\boldsymbol{\omega}_{ib}^{b}$ is the angular rate in body axes measured by the gyroscopes, $\boldsymbol{a}^{b}$ is the specific force in body axes measured by the accelerometers, $\boldsymbol{r}_{INS}^{n}$ and $\boldsymbol{v}_{INS}^{n}$ are the position and velocity in the navigational frame respectively, $\delta\boldsymbol{r}^{n}$ and $\delta\boldsymbol{v}^{n}$ are the difference between the calculated position and velocity of the GPS and the INS, $\boldsymbol{\rho}$ and $\dot{\boldsymbol{\rho}}$ are the raw pseudoranges and carried phase measured by the GPS receiver and $\Delta\boldsymbol{r}^{n}, \Delta\boldsymbol{v}^{n}$ and $\boldsymbol{\varepsilon}^{n}$ are the position, velocity and attitude errors estimated by the INS Kalman filter.

On the other hand, the tightly coupled integration uses a single Kalman filter to integrate both GNSS and INS measurements. This is referred to as tight integration because the INS measurements are also used to aid the GNSS processing. In this case, the position is used to form predicted range measurements to each of the satellites. These ranges are then differenced with the raw GNSS measurements to estimate the INS errors using a single integration filter. An example of this kind of strategy is shown in Figure 4-3.

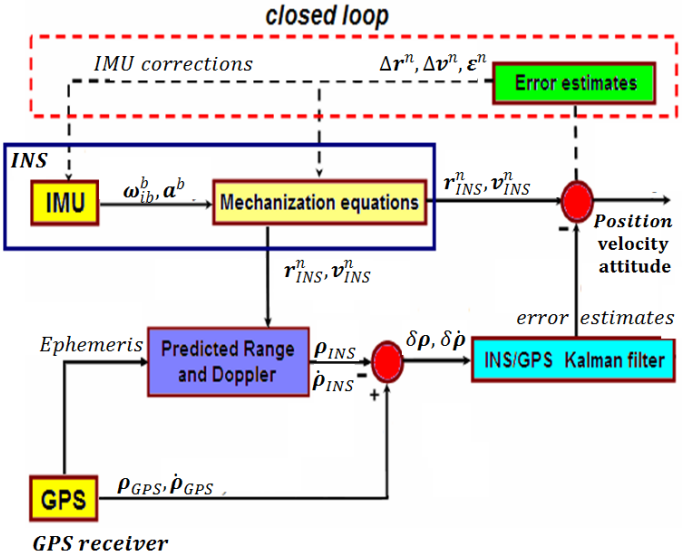

Figure 4-3: INS/GPS Tightly Coupled integration scheme

In Figure 4-3, $\delta\boldsymbol{\rho}$ and $\delta\dot{\boldsymbol{\rho}}$ are the differences between the pseudorange and Doppler

measurements of the GPS and the predicted ones by using the Ephemeries information and the INS calculations.

The loosely coupled scheme has as advantages that the processing time is faster than the tightly coupled one. This is because the dimension of its state vector is smaller than the used in the tightly scheme. Also, the implementation of this architecture is simple and it is possible to build it with the most commons GNSS receivers interfaces (no need to access to information that it is usually handled internally by the GNSS receiver). However, the disadvantages of this scheme are that the GPS receiver needs at least 4 satellites for computing the solution and that the capabilities of filtering are reduced because the process noise is added to two different fusion filters. On the other hand, the tightly coupled integration can provide a solution of navigation even if there are less than 4 satellites visible. The existence of a single filter provides a statistically rigorous information framework between filter states and improves the filtering capabilities because the process noise is only added to this unique filter. Another advantage of the tightly coupled algorithms is the use of the individual data provided by the satellites in the measurement update since satellites with poor measurements can be rejected. However, the TC implementation has some problems because it uses a larger size of the state vector so the computational cost of the fusion algorithm is increased with respect to the LC one. Furthermore, another disadvantage is that requires complete access to the GNSS raw data information, and this is not usually available by regular receivers, so the list of devices that can be used for this approach is drastically reduced.

In this thesis, the global navigator algorithm is implemented as a loosely-coupled scheme. The filter developed manages the following information: accelerations, angular rates, magnetic field measurements and the position, velocity and integrity solution of the EIRE receiver. In Figure 4-4, it is shown the scheme of the implemented filter architecture. The sensor fusion algorithm is based on an Extended Kalman Filter whose system model has been implemented by using the INS error dynamic equations (see section 4.4).

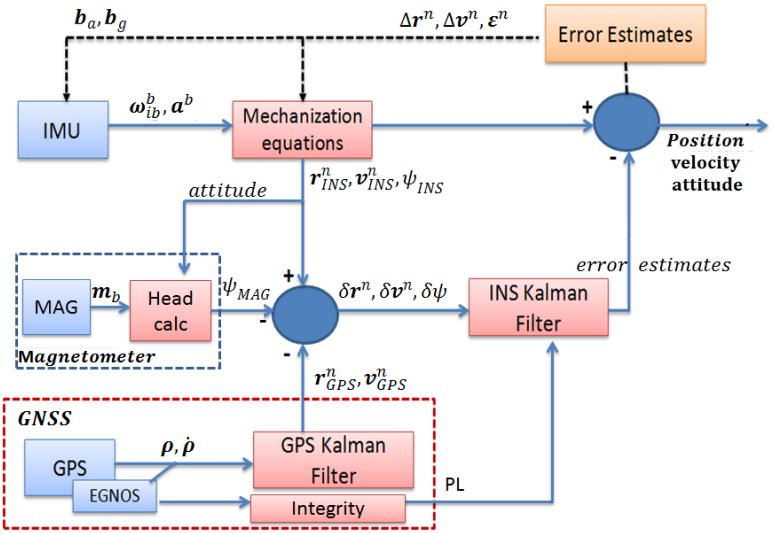

Figure 4-4: Loosely coupled architecture of the EIW global navigator.

In Figure 4-4, ψ_{MAG} is the heading calculated by the magnetometer, $\delta\psi$ is the difference between the headings calculated with the magnetometer and the INS, $\boldsymbol{b}_a$ and $\boldsymbol{b}_g$ are the bias correction terms for the accelerometers and the gyroscopes respectively, and PL are the protection levels calculated by using the integrity information provided by EGNOS.

In the developed algorithm, the measurement model of the fusion filter uses as inputs the differences between the positions and velocities calculated through the INS and the GNSS receiver respectively. It also uses the heading difference calculated comparing the magnetometer calculations and the INS solution. Here, one of the novelties is the use of the integrity information provided by the EGNOS satellites for weighting the filter parameters, allowing the adaptation of the algorithm to the current state of the satellite constellations (this is described in section 4.5.3). This algorithm provides estimations of all observable INS errors, which are used to correct the IMU raw measurements and also to compensate for the navigation solution calculated previously through the mechanization equations. Through this approach, it is possible to obtain a navigational solution with both higher update rate and smaller positioning error than the standalone GPS-receiver and with better accuracy than those navigation algorithms that do not make use of the EGNOS properties.

4.2. Estimation Process: Fusion Algorithm

In this thesis, the algorithm in charge of fusing the different sensors is based on an Extended Kalman filter. The Kalman filter is a recursive algorithm that uses a series of predictions and measurement update steps to obtain an optimal estimate of the state vector in the sense of minimizing the mean square errors. This algorithm assumes that the process **x**(t) to be estimated can be modeled in discrete time and the measurement of the process occurs at discrete points in time. It further assumes that the dynamics noise and the measurement noise have white noise characteristics (i.e. zero-mean and zero-correlation).

The equations in the Kalman filter algorithm fall under two groups. The first group of equations predicts the state (and the associated covariance) of the system, based on the current state and the assumed system model, in order to obtain an *a priori* estimate for the next time step, as indicated by

$$\hat{\boldsymbol{x}}(k+1|k) = \boldsymbol{\phi}_k \hat{\boldsymbol{x}}(k|k) \tag{4-1}$$

$$\boldsymbol{P}(k+1|k) = \boldsymbol{\phi}_k \boldsymbol{P}(k|k) \boldsymbol{\phi}_k^T + \boldsymbol{Q}_k \tag{4-2}$$

$\boldsymbol{P}(k+1|k)$ and $\boldsymbol{P}(k|k)$ are the error covariance matrices associated with the estimated state vector at the prediction and time update steps, respectively.

The second group of equations updates the predicted states and covariance estimates with the currently available measurements in accordance with the measurement model:

$$\hat{\boldsymbol{x}}(k|k) = \hat{\boldsymbol{x}}(k|k-1) + \boldsymbol{K}_k[\boldsymbol{z}_k - \boldsymbol{H}_k \hat{\boldsymbol{x}}(k|k-1)] \tag{4-3}$$

$$\boldsymbol{P}(k|k) = [\boldsymbol{I} - \boldsymbol{K}_k \boldsymbol{H}_k] \boldsymbol{P}(k|k-1) \tag{4-4}$$

The term $[\boldsymbol{z}_k - \boldsymbol{H}_k \hat{\boldsymbol{x}}(k|k-1)]$ is called the innovation sequence; it is the difference between the actual observation and the predicted observation, thus it represents the amount of new information introduced into the system by the actual measurement. The Kalman gain matrix $\boldsymbol{K}_k$ is a weighting factor indicating how much of the new information contained in the innovation sequence should be accepted by the system. As such, the gain matrix is optimized to produce a minimum error variance, and its expression is given by:

$$\boldsymbol{K}_k = \boldsymbol{P}(k|k-1)\boldsymbol{H}_k^T[\boldsymbol{H}_k\boldsymbol{P}(k|k-1)\boldsymbol{H}_k^T + \boldsymbol{R}_k]^{-1} \quad (4\text{-}5)$$

The Kalman Filter is used in linear systems, however, in this case, the navigational equations are not linear. So it is necessary to use another approximation for the estimation of the navigation solution. The Extended Kalman Filter (EKF) extends the scope of Kalman filter to nonlinear optimal filtering problems by forming a Gaussian approximation to the joint distribution of state $\mathbf{x}$ and measurements by using a transformation based on Taylor series. This work implements a first-order EKF where the navigation equations are linearized around the output of the INS. The filtering model used in the EKF is:

$$\boldsymbol{x}_k = \boldsymbol{f}(x_{k-1}, k-1) + \boldsymbol{w}_{k-1} \quad (4\text{-}6)$$

$$\boldsymbol{z}_k = \boldsymbol{h}(x_k, k) + \boldsymbol{r}_k \quad (4\text{-}7)$$

where $\boldsymbol{x}_k$ is the state, $\boldsymbol{z}_k$ is the measurement, $\boldsymbol{w}_{k-1} \sim \boldsymbol{N}(0, \boldsymbol{Q}_{k-1})$ is the process noise, $\boldsymbol{r}_{k-1} \sim \boldsymbol{N}(0, R_{k-1})$ is the measurement noise, $\boldsymbol{f}$ is the nonlinear dynamic model function and $\boldsymbol{h}$ is the measurement model function. The first order EKF approximate the distribution of state $\boldsymbol{x}_k$ given the observations $\boldsymbol{z}_{1:k}$ with a Gaussian:

$$\boldsymbol{p}(\boldsymbol{x}_k|y_{1:k}) \approx \boldsymbol{N}(\boldsymbol{x}_k|\boldsymbol{m}_k, \boldsymbol{P}_k) \quad (4\text{-}8)$$

The EKF is separated into two steps. The steps for the first order EKF are as follows:

Prediction:

$$\boldsymbol{m}_k^- = f(m_{k-1}, k-1) \quad (4\text{-}9)$$

$$\boldsymbol{P}_k^- = \boldsymbol{F}_x(\boldsymbol{m}_{k-1}, k-1)\boldsymbol{P}_{k-1}\boldsymbol{F}_x^T(\boldsymbol{m}_{k-1}, k-1) + \boldsymbol{Q}_{k-1} \quad (4\text{-}10)$$

Update:

$$\boldsymbol{v}_k = \boldsymbol{z}_k - \boldsymbol{h}(m_k^-, k) \quad (4\text{-}11)$$

$$\boldsymbol{S}_k = \boldsymbol{H}_x(\boldsymbol{m}_k^-, k)\boldsymbol{P}_k^-\boldsymbol{H}_x^T(\boldsymbol{m}_k^-, k) \tag{4-12}$$

$$\boldsymbol{K}_k = \boldsymbol{P}_k^-\boldsymbol{H}_x^T(\boldsymbol{m}_k^-, k)\boldsymbol{S}_k^{-1} \tag{4-13}$$

$$\boldsymbol{m}_k = \boldsymbol{m}_k^- + \boldsymbol{K}_k\boldsymbol{v}_k \tag{4-14}$$

$$\boldsymbol{P}_k = \boldsymbol{P}_k^- - \boldsymbol{K}_k\boldsymbol{S}_k S_k^T \tag{4-15}$$

where the matrices $\boldsymbol{F}_x(\boldsymbol{m}_{k-1}, k-1)$and $\boldsymbol{H}_x(\boldsymbol{m}_k^-, k)$ are the Jacobians of f and h, with elements

$$[\boldsymbol{F}_x(m_k, k-1)]_{j,j'} = \left.\frac{\delta f_j(x, k-1)}{\delta x_{j'}}\right]_{x=m} \tag{4-16}$$

$$[\boldsymbol{H}_x(m_k, k-1)]_{j,j'} = \left.\frac{\delta h_j(x, k)}{\delta x_{j'}}\right]_{x=m} \tag{4-17}$$

The estimation process follows the scheme presented in the Figure 4-5.

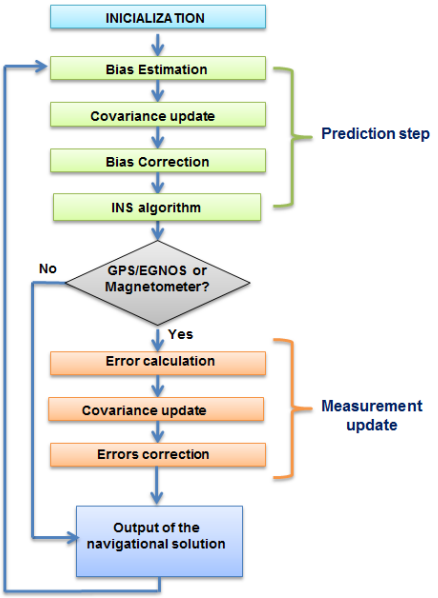

Figure 4-5: Scheme of the estimation process.

In the beginning, an initialization step is performed to initialize and calibrate the sensors, the initial values are given to the algorithms and the alignment is done automatically. Once this step has finished, the estimation process begins. If one of the sensors of the measurement model (GPS/ EGNOS and/or the magnetometer) has new data, the solution calculated using the INS equations is compared with the measurements and the error is estimated, then the covariance is updated, the errors are corrected and the integrators of the INS are reset.

Once the estimation measurement update step is finished, or if there are not new measurements from the sensors, the bias of the accelerometers and gyroscopes are calculated, the covariance is updated and the bias of the IMU sensors is corrected. Finally, the equations of the INS are solved and the new navigational solution is calculated. These steps are performed at the IMU rate, providing a faster solution than the GPS sensors typically provide.

4.3. Mechanization equations of the inertial navigation system

The mechanization equations are a set of differential equations that convert the output of the Inertial Measurement Unit, which includes rotation rates and specific force measurements, into position, velocity, and attitude information. Kinematic equations describe mathematically the movement of the vehicle; its derivation can be divided into three parts: position, velocity, and attitude. The position in the navigational frame is expressed in curvilinear coordinates.

$$\boldsymbol{r}^n = [\varphi \quad \lambda \quad h]^T \tag{4-18}$$

where r^n is the position vector in the navigation frame, φ is the latitude, λ the longitude and h is the altitude of the RPA in the Worl Geodetic System 1984(WGS84). While the velocities (v^n) are expressed with respect to the north, east and down (NED)

$$\boldsymbol{v}^n = [v_N \quad v_E \quad v_D]^T \tag{4-19}$$

And they are defined in the n-frame by:

$$\boldsymbol{v}^n = \begin{pmatrix} v_N \\ v_E \\ v_D \end{pmatrix} = \begin{pmatrix} (R_m + h) & 0 & 0 \\ 0 & (R_N + h)cos\varphi & 0 \\ 0 & 0 & -1 \end{pmatrix} \begin{pmatrix} \dot{\varphi} \\ \dot{\lambda} \\ \dot{h} \end{pmatrix} \tag{4-20}$$

Where R_N and R_N are radii of curvature in the meridian and prime vertical at a given latitude (see section 3.1). So, the time derivative of the curvilinear coordinates can be defined by:

$$\dot{\boldsymbol{r}}^n = \boldsymbol{D}^{-1}\boldsymbol{v}^n \tag{4-21}$$

where:

$$\boldsymbol{D^{-1}} = \boldsymbol{diag}\left(\frac{1}{R_m + h}, \frac{1}{\left(R_p + h\right)\cos(\varphi)}, -1\right) \tag{4-22}$$

In order to obtain the velocity dynamics equations, it is possible to start from the following equation (similar derivations can be found in (Esmat, 2007) and (Noureldin, Karamat and Georgy, 2013)):

$$\boldsymbol{v}^n = \boldsymbol{R}_e^n \dot{\boldsymbol{r}}^e \tag{4-23}$$

Now the time derivative of the coordinates is expressed in the earth frame:

$$\dot{\boldsymbol{r}}^e = \boldsymbol{R}_i^e(\dot{\boldsymbol{r}}^i - \boldsymbol{\Omega}_{ie}^i \boldsymbol{r}^i) \tag{4-24}$$

Where Ω represents the skew-symmetric matrix form of the vector ω and R_i^e is the rotation matrix from the inertial to the earth frame. If eq.(4-24) is substituted into (4-23), it is obtained:

$$\boldsymbol{v}^n = \boldsymbol{R}_i^n(\dot{\boldsymbol{r}}^i - \boldsymbol{\Omega}_{ie}^i \boldsymbol{r}^i) \tag{4-25}$$

Where $\boldsymbol{R}_i^n$ is the rotation matrix from the inertial to the navigation frame. So, considering the Earth's rotation rate as a constant, the velocity dynamics can be obtained as follows:

$$\begin{aligned}\dot{\boldsymbol{v}}^n &= \boldsymbol{R}_i^n\boldsymbol{\Omega}_{ni}^i\left(\dot{\boldsymbol{r}}^i - \boldsymbol{\Omega}_{ie}^i\boldsymbol{r}^i\right) + \boldsymbol{R}_i^n\left(\ddot{\boldsymbol{r}}^i - \boldsymbol{\Omega}_{ie}^i\dot{\boldsymbol{r}}^i\right)\\ &= \boldsymbol{R}_i^n\ddot{\boldsymbol{r}}^i + \boldsymbol{R}_i^n\left(\boldsymbol{\Omega}_{ni}^i - \boldsymbol{\Omega}_{ie}^i\right)\boldsymbol{r}^i - \boldsymbol{R}_i^n\boldsymbol{\Omega}_{ni}^i\boldsymbol{\Omega}_{ie}^i\boldsymbol{r}^i\end{aligned} \tag{4-26}$$

From eq.(4-26), if the position rate is written in the inertial frame:

$$\begin{aligned}\dot{\boldsymbol{v}}^n &= \boldsymbol{R}_i^n\boldsymbol{\Omega}_{ni}^i\left(\dot{\boldsymbol{r}}^i - \boldsymbol{\Omega}_{ie}^i\boldsymbol{r}^i\right) + \boldsymbol{R}_i^n\left(\ddot{\boldsymbol{r}}^i - \boldsymbol{\Omega}_{ie}^i\dot{\boldsymbol{r}}^i\right)\\ &= \boldsymbol{R}_i^n\ddot{\boldsymbol{r}}^i + \boldsymbol{R}_i^n\left(\boldsymbol{\Omega}_{ni}^i - \boldsymbol{\Omega}_{ie}^i\right)\boldsymbol{r}^i - \boldsymbol{R}_i^n\boldsymbol{\Omega}_{ni}^i\boldsymbol{\Omega}_{ie}^i\boldsymbol{r}^i\end{aligned} \tag{4-27}$$

and taking into account that $\boldsymbol{I} = \boldsymbol{R}_n^i\boldsymbol{R}_i^n$, it is possible to use this relation in (4-26) to obtain:

$$\begin{aligned}\dot{\boldsymbol{v}}_n &= \boldsymbol{R}_i^n\ddot{\boldsymbol{r}}^i + \boldsymbol{R}_i^n\left(\boldsymbol{\Omega}_{ni}^i - \boldsymbol{\Omega}_{ie}^i\right)\boldsymbol{R}_n^i\boldsymbol{R}_i^n\boldsymbol{R}_e^i(\dot{\boldsymbol{r}}^e + \boldsymbol{\Omega}_{ie}^e\boldsymbol{r}^e) - \boldsymbol{R}_i^n\boldsymbol{\Omega}_{ni}^i\boldsymbol{\Omega}_{ie}^i\boldsymbol{r}^i\\ &= \boldsymbol{R}_i^n\ddot{\boldsymbol{r}}^i + (\boldsymbol{\Omega}_{ni}^n - \boldsymbol{\Omega}_{ie}^n)\boldsymbol{R}_e^n\dot{\boldsymbol{r}}^e + (\boldsymbol{\Omega}_{ni}^n - \boldsymbol{\Omega}_{ie}^n)\boldsymbol{R}_e^n\boldsymbol{\Omega}_{ie}^e\boldsymbol{r}^e - \boldsymbol{R}_i^n\boldsymbol{\Omega}_{ni}^i\boldsymbol{\Omega}_{ie}^i\boldsymbol{r}^i\\ &= \boldsymbol{R}_i^n\ddot{\boldsymbol{r}}^i + (\boldsymbol{\Omega}_{ni}^n - \boldsymbol{\Omega}_{ie}^n)\boldsymbol{R}_e^n\dot{\boldsymbol{r}}^e + \boldsymbol{\Omega}_{ni}^n\boldsymbol{R}_e^n\boldsymbol{\Omega}_{ie}^e\boldsymbol{r}^e - \boldsymbol{\Omega}_{ie}^n\boldsymbol{R}_e^n\boldsymbol{\Omega}_{ie}^e\boldsymbol{r}^e - \boldsymbol{R}_i^n\boldsymbol{\Omega}_{ni}^i\boldsymbol{\Omega}_{ie}^i\boldsymbol{r}^i\end{aligned} \tag{4-28}$$

If now, the equation (4-25) is used with the following expression:

$$\boldsymbol{\Omega}_{ni}^n\boldsymbol{R}_e^n\boldsymbol{\Omega}_{ie}^i r^e = \boldsymbol{R}_n^i\boldsymbol{R}_i^n\boldsymbol{\Omega}_{ni}^n\boldsymbol{R}_i^n\boldsymbol{R}_n^i\boldsymbol{R}_e^n\boldsymbol{\Omega}_{ie}^e\boldsymbol{R}_i^e\boldsymbol{R}_e^i\boldsymbol{r}^e) = \boldsymbol{R}_i^n\boldsymbol{\Omega}_{ni}^i\boldsymbol{\Omega}_{ie}^i\boldsymbol{r}^i \tag{4-29}$$

It is possible to reduce the velocity dynamics to:

$$\begin{aligned}\dot{\boldsymbol{v}}^n &= \boldsymbol{R}_i^n\ddot{\boldsymbol{r}}^i + (\boldsymbol{\Omega}_{ni}^n - \boldsymbol{\Omega}_{ie}^n)\boldsymbol{v}_n - \boldsymbol{\Omega}_{ie}^n\boldsymbol{R}_e^n\boldsymbol{\Omega}_{ie}^e\boldsymbol{r}^e\\ &= \boldsymbol{R}_i^n\ddot{\boldsymbol{r}}^i - (2\boldsymbol{\Omega}_{ie}^n + \boldsymbol{\Omega}_{en}^n)\,\boldsymbol{v}_n - \boldsymbol{R}_e^n\boldsymbol{\Omega}_{ie}^e\boldsymbol{\Omega}_{ie}^e\boldsymbol{r}^e\end{aligned} \tag{4-30}$$

If we come back to the equation of the specific force introduced in section 0:

$$\boldsymbol{f} = \ddot{\boldsymbol{r}}^i - \boldsymbol{g} \tag{4-31}$$

and we use it in the equation (4-30), this yields

$$\begin{aligned}\dot{\boldsymbol{v}}^n &= \boldsymbol{R}_i^n(\boldsymbol{f}^i + \boldsymbol{g}^i) - (2\boldsymbol{\Omega}_{ie}^n + \boldsymbol{\Omega}_{en}^n)\,\boldsymbol{v}_n - \boldsymbol{R}_e^n\boldsymbol{\Omega}_{ie}^e\boldsymbol{\Omega}_{ie}^e\boldsymbol{r}^e\\ &= \boldsymbol{R}_i^n\boldsymbol{f}^i - (2\boldsymbol{\Omega}_{ie}^n + \boldsymbol{\Omega}_{en}^n)\boldsymbol{v}_n + \boldsymbol{R}_e^n\,(\boldsymbol{g}^e - \boldsymbol{\Omega}_{ie}^e\boldsymbol{\Omega}_{ie}^e\boldsymbol{r}^e)\\ &= \boldsymbol{R}_b^n\boldsymbol{f}^b - (2\boldsymbol{\Omega}_{ie}^n + \boldsymbol{\Omega}_{en}^n)\boldsymbol{v}_n + \boldsymbol{g}^n\end{aligned} \tag{4-32}$$

Finally, eq.(4-32) can be expressed as:

$$\dot{\boldsymbol{v}}^n = \boldsymbol{R}_b^n \boldsymbol{f}^b - (2\boldsymbol{\omega}_{ie}^n + \boldsymbol{\omega}_{en}^n) \times \boldsymbol{v}^n + \boldsymbol{g}^n \tag{4-33}$$

For the attitude dynamics, it is used the following definition:

$$\dot{\boldsymbol{R}}_b^n = \boldsymbol{R}_b^n \boldsymbol{\Omega}_{nb}^b = \boldsymbol{R}_b^n (\boldsymbol{\Omega}_{ib}^b - \boldsymbol{\Omega}_{in}^b) \tag{4-34}$$

Finally, through the equations (4-22), (4-32) and (4-33), it is possible to obtain the navigation equations that are used in the fusion algorithm of the global navigator system developed in this thesis:

$$\begin{bmatrix} \dot{\boldsymbol{r}}^n \\ \dot{\boldsymbol{v}}^n \\ \dot{\boldsymbol{R}}_b^n \end{bmatrix} = \begin{bmatrix} \boldsymbol{D}^{-1}\boldsymbol{v}^n \\ \boldsymbol{R}_b^n \boldsymbol{f}^b - \left(2\widetilde{\Omega}_{ie}^n + \widetilde{\Omega}_{en}^n\right)\boldsymbol{v}^n + \boldsymbol{g}^n \\ \boldsymbol{R}_b^n \widetilde{\Omega}_{ib}^b - \left(\widetilde{\Omega}_{ie}^n + \widetilde{\Omega}_{en}^n\right)\boldsymbol{R}_b^n \end{bmatrix} \tag{4-35}$$

Where $\boldsymbol{f}^b$ and $\boldsymbol{\Omega}_{ib}{}^b$ are the outputs of the IMU and g is the gravity vector. In order to update the attitude, we have that the increment of the angular velocity with respect the navigation plane is given by the equation:

$$\underline{\boldsymbol{\omega}}_{nb}^b = \underline{\boldsymbol{\omega}}_{ib}^b - \boldsymbol{R}_n^b \left(\underline{\boldsymbol{\omega}}_{ie}^n + \underline{\boldsymbol{\omega}}_{en}^n\right) \tag{4-36}$$

Generally, the computation of the attitude update is performed by using quaternions. In this way, it is possible to avoid the singularities and to improve the computational load. The update of the quaternions is given by:

$$\dot{\boldsymbol{q}} = 0.5 \begin{bmatrix} 0 & -\omega_{nb,x}^b & -\omega_{nb,y}^b & -\omega_{nb,z}^b \\ \omega_{nb,x}^b & 0 & \omega_{nb,z}^b & -\omega_{nb,y}^b \\ \omega_{nb,y}^b & -\omega_{nb,z}^b & 0 & \omega_{nb,x}^b \\ \omega_{nb,z}^b & \omega_{nb,y}^b & -\omega_{nb,x}^b & 0 \end{bmatrix} q \tag{4-37}$$

$$\boldsymbol{q}_{k+1} = \boldsymbol{q}_k + \dot{\boldsymbol{q}} dt \tag{4-38}$$

Where dt is the time between two measures of the gyros. Once the quaternions are obtained, the DCM is built by using:

$$\boldsymbol{R}_b^n = \begin{pmatrix} (q_1^2 + q_2^2 + q_3^2 + q_4^2) & 2(q_1q_2 - q_3q_4) & 2(q_1q_3 + q_2q_4) \\ 2(q_1q_2 + q_3q_4) & (q_2^2 - q_1^2 - q_3^2 + q_4^2) & 2(q_2q_3 - q_1q_4) \\ 2(q_1q_3 - q_2q_4) & 2(q_2q_3 + q_1q_4) & (q_3^2 - q_1^2 - q_2^2 + q_4^2) \end{pmatrix} \quad (4\text{-}39)$$

As it was explained through the equation (4-33), the velocity in the navigation plane is obtained by applying the Coriolis and gravity corrections. The velocity in the following time frame is calculated as:

$$\underline{\boldsymbol{v}}_{k+1} = \underline{\boldsymbol{v}}_k + \underline{\dot{\boldsymbol{v}}}dt \quad (4\text{-}40)$$

Finally, in order to update the position, a trapezoidal integration is applied:

$$\boldsymbol{r}_{\boldsymbol{k+1}}^{\boldsymbol{n}} = \boldsymbol{r}_k^n + \frac{1}{2}\boldsymbol{D}^{-1}(\boldsymbol{v}_k^n + \boldsymbol{v}_{k+1}^n)dt \quad (4\text{-}41)$$

Using these equations, the mechanization equations in the UAV navigaton system can be calculated by following four basic steps:

1. Correction of raw data through known or estimated errors.
2. Attitude update.
3. Transformation of specific force to the navigation frame.
4. Calculation of velocity and position.

These steps are summarized in the scheme presented in Figure 4-6.

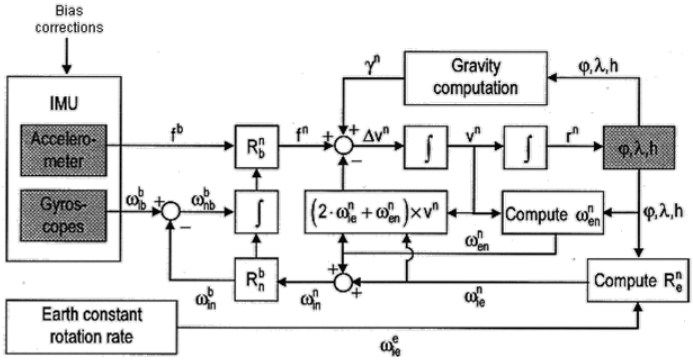

Figure 4-6: Mechanization Equations (Solimeno, 2007)

4.4. Equation of the dynamic error in the INS

The dynamic error equations are obtained by perturbing the kinematic equations. These equations are necessary to build the Kalman filter, which is responsible for correcting the outputs of the IMU. The perturbation of the position, velocity, and attitude can be expressed as follows:

$$\hat{\boldsymbol{r}}^n = \boldsymbol{r}^n + \delta\boldsymbol{r}^n \tag{4-42}$$

$$\hat{\boldsymbol{v}}^n = \boldsymbol{v}^n + \delta\boldsymbol{v}^n \tag{4-43}$$

$$\hat{\boldsymbol{R}}_b^n = (\boldsymbol{I} - \boldsymbol{E}^n)\boldsymbol{R}_b^n \tag{4-44}$$

Where:

$\delta\boldsymbol{r}^n = [\delta\varphi \quad \delta\phi \quad \delta h]$ are the position errors described in curvilinear coordinates.

$\delta\boldsymbol{v}^n = [\delta v_N \quad \delta v_E \quad \delta v_D]$ are the velocity errors in the navigation plane.

And finally $\boldsymbol{E}^n$ is the skew-symmetric matrix of the attitude errors:

$$\boldsymbol{E}^n = (\boldsymbol{\varepsilon}^n \times) = \begin{bmatrix} 0 & -\varepsilon_D & \varepsilon_E \\ \varepsilon_D & 0 & -\varepsilon_N \\ -\varepsilon_E & \varepsilon_N & 0 \end{bmatrix} \tag{4-45}$$

4.4.1. Position, velocity and attitude errors

Perturbing the equation of the position $\dot{\boldsymbol{r}}^n = \boldsymbol{D}^{-1}\boldsymbol{v}^n$, it is possible to obtain the linearized position error (Esmat, 2007).

$$\partial\dot{\boldsymbol{r}}^n = \boldsymbol{F}_{rr}\delta\boldsymbol{r}^n + \boldsymbol{F}_{rv}\delta\boldsymbol{v}^n \tag{4-46}$$

Where $\boldsymbol{F}_{rr}$ and $\boldsymbol{F}_{rv}$ are the Jacobians of the mechanization equations that were deduced in Section 4.3, and can be expressed as:

$$\boldsymbol{F}_{rr} = \begin{bmatrix} \frac{\delta\dot{\varphi}}{\delta\varphi} & \frac{\delta\dot{\varphi}}{\delta\lambda} & \frac{\delta\dot{\varphi}}{\delta h} \\ \frac{\delta\dot{\lambda}}{\delta\varphi} & \frac{\delta\dot{\lambda}}{\delta\lambda} & \frac{\delta\dot{\lambda}}{\delta h} \\ \frac{\delta\dot{h}}{\delta\varphi} & \frac{\delta\dot{h}}{\delta\lambda} & \frac{\delta\dot{\phi}}{\delta h} \end{bmatrix} = \begin{bmatrix} 0 & 0 & \frac{-V_N}{(R_M+h)^2} \\ \frac{v_E sin\varphi}{(R_N+h)cos^2\varphi} & 0 & \frac{v_E}{(R_N+h)^2 cos\varphi} \\ 0 & 0 & 0 \end{bmatrix} \tag{4-47}$$

$$\boldsymbol{F}_{rv} = \begin{bmatrix} \frac{\delta\dot{\varphi}}{\delta V_N} & \frac{\delta\dot{\varphi}}{\delta V_E} & \frac{\delta\dot{\varphi}}{\delta V_D} \\ \frac{\delta\dot{\lambda}}{\delta V_N} & \frac{\delta\dot{\lambda}}{\delta V_E} & \frac{\delta\dot{\lambda}}{\delta V_D} \\ \frac{\delta\dot{h}}{\delta V_N} & \frac{\delta\dot{h}}{\delta V_E} & \frac{\delta\dot{\phi}}{\delta V_D} \end{bmatrix} = \begin{bmatrix} \frac{1}{R_M+h} & 0 & 0 \\ 0 & \frac{1}{(R_N+h)cos\varphi} & 0 \\ 0 & 0 & -1 \end{bmatrix} \tag{4-48}$$

The velocity error dynamics equation can be obtained from the mechanization equation (4-33). In that way, the dynamics of the velocity error can be expressed as:

$$\begin{aligned} \delta\dot{\boldsymbol{v}}^n &= \delta\boldsymbol{R}_b^n\boldsymbol{f}^b + \boldsymbol{R}_b^n\delta\boldsymbol{f}^b - \left(2\widetilde{\Omega}_{ie}^n + \widetilde{\Omega}_{en}^n\right)\delta\boldsymbol{v}^n - \left(2\delta\widetilde{\Omega}_{ie}^n + \delta\widetilde{\Omega}_{en}^n\right)\boldsymbol{v}^n + \delta\boldsymbol{g}^n \\ &= \delta\boldsymbol{R}_b^n\boldsymbol{f}^b + \boldsymbol{R}_b^n\delta\boldsymbol{f}^b - \left(2\widetilde{\Omega}_{ie}^n + \widetilde{\Omega}_{en}^n\right)\delta\boldsymbol{v}^n + \boldsymbol{v}^n(2\delta\boldsymbol{\omega}_{ie}^n + \delta\boldsymbol{\omega}_{en}^n) + \delta\boldsymbol{g}^n \end{aligned} \tag{4-49}$$

The errors of the angular velocity vectors are calculated as:

$$\boldsymbol{\omega}_{ie}^n = \omega_e[\cos(\varphi) \quad 0 \quad -\operatorname{sen}(\varphi)]^T \tag{4-50}$$

$$\delta\boldsymbol{\omega}_{ie}^n = \boldsymbol{C}_{\omega ep}\delta\mathbf{r}^n = \omega_e[-\operatorname{sen}(\varphi) \quad 0 \quad -\cos(\varphi)]^T\,\delta\varphi \tag{4-51}$$

$$\boldsymbol{\omega}_{en}^n = \left[\frac{v_E}{R_p+h} \quad -\frac{v_N}{R_m+h} \quad -\frac{v_E\tan(\varphi)}{R_p+h}\right]^T \tag{4-52}$$

$$\delta\boldsymbol{\omega}_{en}^n = \boldsymbol{C}_{\omega np}\delta\boldsymbol{r}^n + \boldsymbol{C}_{\omega nv}\delta\boldsymbol{v}^n \tag{4-53}$$

$$\boldsymbol{C}_{\omega np} = \begin{bmatrix} 0 & 0 & \dfrac{v_E}{\left(R_p + h\right)^2} \\ 0 & 0 & \dfrac{v_N}{(R_m + h)^2} \\ -\dfrac{v_E}{(R_p + h)\cos^2(\varphi)} & 0 & \dfrac{v_E \tan(\varphi)}{\left(R_p + h\right)^2} \end{bmatrix} \tag{4-54}$$

$$\boldsymbol{C}_{\omega nv} = \begin{bmatrix} 0 & \dfrac{1}{R_p + h} & 0 \\ -\dfrac{1}{R_m + h} & 0 & 0 \\ 0 & -\dfrac{\tan(\varphi)}{R_p + h} & 0 \end{bmatrix} \tag{4-55}$$

The error of the gravity vector can be expressed as:

$$\delta \boldsymbol{g}^n = \boldsymbol{G}_r \delta \boldsymbol{r}^n \tag{4-56}$$

$$\boldsymbol{G}_r = \begin{bmatrix} 0 & 0 & 0 \\ 0 & 0 & 0 \\ g_\varphi & 0 & g_h \end{bmatrix} \tag{4-57}$$

$$g_h = -2\gamma/a(1 + f + m - 2fsen^2(\varphi)) \tag{4-58}$$

$$g_\varphi = \gamma'[1 - \frac{2}{a(1 + f + m - 2fsen^2(\varphi)h]} + 4\gamma fhsen(2\varphi)/a \tag{4-59}$$

Finally, it is necessary to obtain the error of the rotation matrix $\delta \boldsymbol{R}_b^n$ in order to calculate the term $\delta \boldsymbol{R}_b^n \boldsymbol{f}^b$. For this, it is possible to use that the estimated transformation matrix can be expressed as:

$$\widehat{\boldsymbol{R}}_b^n = \boldsymbol{R}_b^n + \delta \boldsymbol{R}_b^n = (\boldsymbol{I} + \widetilde{\boldsymbol{E}}) \boldsymbol{R}_b^n \tag{4-60}$$

Where $\widetilde{\boldsymbol{E}}$ is the anti-symmetric matrix that corresponds to the attitude error $\boldsymbol{\varepsilon}$. In this way it is obtained:

$$\delta \boldsymbol{R}_b^n = \widetilde{\boldsymbol{E}} \boldsymbol{R}_b^n \tag{4-61}$$

$$\delta \boldsymbol{R}_b^n \boldsymbol{f}^b = \widetilde{\boldsymbol{F}}^n \boldsymbol{\varepsilon} \tag{4-62}$$

Substituting the previous expressions in the equation of the velocity error dynamics, it is obtained that:

$$\delta \dot{\boldsymbol{v}}^n = \widetilde{\boldsymbol{F}}^n \boldsymbol{\varepsilon} + \boldsymbol{R}_b^n \delta \boldsymbol{f}^b - \left(2\widetilde{\Omega}_{ie}^n + \widetilde{\Omega}_{en}^n\right)\delta \boldsymbol{v}^n + \widetilde{\boldsymbol{V}}^n \left(\left(2\boldsymbol{C}_{\omega ep} + \boldsymbol{C}_{\omega np}\right)\delta \boldsymbol{r}^n + \boldsymbol{C}_{\omega nv}\delta \boldsymbol{v}^n\right) + \boldsymbol{G}_r \delta \boldsymbol{r}^n \tag{4-63}$$

This equation can be grouped as:

$$\delta \dot{\boldsymbol{v}}^n = \boldsymbol{F}_{vr}\delta \boldsymbol{r}^n + \boldsymbol{F}_{vv}\delta \boldsymbol{v}^n + (\boldsymbol{f}^n \times)\boldsymbol{\varepsilon}^n + \boldsymbol{R}_b^n \delta \boldsymbol{f}^b \tag{4-64}$$

where $\delta \boldsymbol{f}^b$ is the perturbation of the specific force vector in the body frame and the final Jacobian matrices are calculated as:

$$\boldsymbol{F}_{vr} = \begin{bmatrix} -2v_E\omega_e cos\varphi - \dfrac{v_E^2}{(Rn+h)cos^2\varphi} & 0 & \dfrac{-v_N v_D}{(R_M+h)^2} + \dfrac{v_E^2 tan\varphi}{(R_N+h)^2} \\ -2\omega_e(v_N cos\varphi - v_D sin\varphi) + \dfrac{v_E V_N}{(Rn+h)cos^2\varphi} & 0 & \dfrac{-v_E(v_D + v_N tan\varphi)}{(R_N+h)^2} \\ 2v_E\omega_e sin\varphi & 0 & \dfrac{v_E^2}{(R_N+h)^2} + \dfrac{v_N^2}{(R_M+h)^2} - \dfrac{2\gamma}{(R+h)} \end{bmatrix} \tag{4-65}$$

$$\boldsymbol{F}_{vv} = \begin{bmatrix} \dfrac{v_D}{R_M+h} & -2w_e sin\varphi - 2\dfrac{v_E tan\varphi}{R_N+h} & \dfrac{v_N}{R_M+h} \\ 2\omega_e sin\varphi + \dfrac{v_E tan\varphi}{R_N+h} & \dfrac{v_D + v_N tan\varphi}{R_N+h} & 2\omega ecos\varphi + \dfrac{v_E}{R_N+h} \\ -2\dfrac{v_N}{R_M+h} & -2w_e cos\varphi - 2\dfrac{v_E}{R_N+h} & 0 \end{bmatrix} \tag{4-66}$$

Finally, the linearization of the attitude error dynamic equation can be calculated as:

$$\dot{\boldsymbol{\varepsilon}} = -(\widetilde{\boldsymbol{\omega}}_{ie}^n + \widetilde{\boldsymbol{\omega}}_{en}^n)\boldsymbol{\varepsilon} + \left(\boldsymbol{C}_{\omega np} + \boldsymbol{C}_{\omega ep}\right)\delta \boldsymbol{r}^n + \boldsymbol{C}_{\omega nv}\delta \boldsymbol{v}^n - \boldsymbol{R}_b^n \delta \boldsymbol{\omega}_{ib}^b \tag{4-67}$$

If these terms are grouped, the equation can be expressed as:

$$\dot{\boldsymbol{\varepsilon}}^n = \boldsymbol{F}_{er}\delta \boldsymbol{r}^n + \boldsymbol{F}_{ev}\delta \boldsymbol{v}^n - (\boldsymbol{\omega}_{in}^n \times)\boldsymbol{\varepsilon}^n - \boldsymbol{R}_b^n \delta \boldsymbol{\omega}_{ib}^b \tag{4-68}$$

where:

$$\boldsymbol{F}_{er} = \begin{bmatrix} -\omega_e sin\varphi & 0 & \dfrac{-v_E}{(R_N+h)^2} \\ 0 & 0 & \dfrac{v_N}{(R_M+h)^2} \\ -\omega_e cos\varphi - \dfrac{v_E}{(R_N+h)cos^2\varphi} & 0 & \dfrac{v_E tan\varphi}{(R_N+h)^2} \end{bmatrix} \tag{4-69}$$

$$\boldsymbol{F}_{er} = \begin{bmatrix} 0 & \dfrac{1}{R_N+h} & 0 \\ \dfrac{-1}{R_N+h} & 0 & 0 \\ 0 & \dfrac{-tan\varphi}{R_N+h} & 0 \end{bmatrix} \tag{4-70}$$

Where $\delta\underline{\boldsymbol{\omega}}_{ib}^{b}$ is the perturbation of the angular velocity vector of the body frame relative to the inertial frame and expressed in the body frame.

Finally, the error dynamic equations of the measurements of the sensors can be obtained from the relations explained in section 0. These equations are given by

$$\delta\dot{\boldsymbol{f}}^b = -\boldsymbol{T}_a^{-1}\boldsymbol{f}^b + \boldsymbol{w}_a \tag{4-71}$$

$$\delta\dot{\boldsymbol{\omega}}_{ib}^{b} = -\boldsymbol{T}_g^{-1}\boldsymbol{\omega}_{ib}^{b} + \boldsymbol{w}_g \tag{4-72}$$

where $\boldsymbol{T}_a$ and $\boldsymbol{T}_g$ are the correlation time of the accelerometer and gyroscopes noise respectively, and $\boldsymbol{w}_a$ and $\boldsymbol{w}_g$ are white noise of the accelerometers and gyros.

4.5. Integration Process

This section details the mathematical models used to build the EKF developed in this thesis. The state vector used in our filter implementation is the following:

$$x = [\delta\boldsymbol{r}^n \quad \delta\boldsymbol{v}^n \quad \varepsilon^n \quad \boldsymbol{b}_a \quad \boldsymbol{b}_g] \tag{4-73}$$

Where $\boldsymbol{r}^n$, $\delta\boldsymbol{v}^n$ and ε^n are the position, velocity and the attitude error vectors respectively and $\boldsymbol{b}_a$ and $\boldsymbol{b}_g$ are the accelerometer and gyroscopes bias drift vectors.

As it was explained before, the final objective of the fusion filter is to use its

estimations to correct the position, velocity and attitude solution that has been calculated using the mechanization equations of the INS. At the same time, the filter is also in charge of reducing the IMU measurements errors by using the bias calculated during the estimation algorithm.

4.5.1. System Model

Equations of the dynamic error of the INS can be included in a system dynamic matrix **F** in that way that $\dot{\boldsymbol{x}} = \boldsymbol{F}\boldsymbol{x} + \boldsymbol{G}\boldsymbol{w}$

$$\begin{bmatrix} \boldsymbol{\delta\dot{r}^n} \\ \boldsymbol{\delta\dot{v}^n} \\ \boldsymbol{\dot{\varepsilon}} \\ \boldsymbol{\delta\dot{f}^b} \\ \boldsymbol{\delta\dot{\omega}_{ib}^b} \end{bmatrix} = \begin{bmatrix} \boldsymbol{F_{rr}} & \boldsymbol{F_{rv}} & \boldsymbol{0_{3x3}} & \boldsymbol{0_{3x3}} & \boldsymbol{0_{3x3}} \\ \boldsymbol{F_{vr}} & \boldsymbol{F_{vv}} & (\boldsymbol{f^n}\times) & \boldsymbol{R_b^n} & \boldsymbol{0_{3x3}} \\ \boldsymbol{F_{er}} & \boldsymbol{F_{ev}} & -(\boldsymbol{\omega_{in}^n}\times) & \boldsymbol{0_{3x3}} & -\boldsymbol{R_b^n} \\ \boldsymbol{0_{3x3}} & \boldsymbol{0_{3x3}} & \boldsymbol{0_{3x3}} & -\boldsymbol{diag}(\boldsymbol{T_a^{-1}}) & \boldsymbol{0_{3x3}} \\ \boldsymbol{0_{3x3}} & \boldsymbol{0_{3x3}} & \boldsymbol{0_{3x3}} & \boldsymbol{0_{3x3}} & -\boldsymbol{diag}(\boldsymbol{T_g^{-1}}) \end{bmatrix} + \boldsymbol{G}\boldsymbol{w} \quad (4\text{-}74)$$

Here, the terms $\boldsymbol{F_{xy}}$ correspond to the terms that were calculated in section 4.4.1, and the noise terms can be expressed as:

$$\boldsymbol{w} = [\boldsymbol{w_a} \;\; \boldsymbol{w_g}]^T \quad (4\text{-}75)$$

$$\boldsymbol{G} = \begin{bmatrix} \boldsymbol{0_{3x3}} & \boldsymbol{0_{3x3}} \\ \boldsymbol{R_b^n} & \boldsymbol{0_{3x3}} \\ \boldsymbol{0_{3x3}} & -\boldsymbol{R_b^n} \\ \boldsymbol{0_{3x3}} & \boldsymbol{0_{3x3}} \\ \boldsymbol{0_{3x3}} & \boldsymbol{0_{3x3}} \end{bmatrix} \quad (4\text{-}76)$$

$$\boldsymbol{Q_{ini}} = \begin{bmatrix} \boldsymbol{diag}(\boldsymbol{q_{a)}} & \boldsymbol{0_{3x3}} \\ \boldsymbol{0_{3x3}} & \boldsymbol{diag}(\boldsymbol{q_{b)}} \end{bmatrix} \quad (4\text{-}77)$$

Where $\boldsymbol{w}$ is the system noise vector, **G** is the noise-input mapping matrix and $\boldsymbol{Q_{ini}}$ is the covariance matrix vector. The terms of the diagonal matrix of covariance Q are usually the expected noise of the accelerometers and gyroscopes, however in this thesis, one of the novelties introduced is that this matrix can be dynamically weighted by using the EGNOS information in order to improve the accuracy of the filter. This will be expanded in section 4.5.3.

Due to the measurements of the IMU are by its nature discrete over time, these

equations need to be discretized for its implementation in the computer algorithms. In that way the continuous-time system matrix **F** is transformed to its corresponding discrete-time form:

$$\boldsymbol{x}_{k+1} = \boldsymbol{\Phi}_k \boldsymbol{x}_k + \boldsymbol{w}_k \tag{4-78}$$

Where k denotes the instant of time t_k and $\boldsymbol{\Phi}_k$ is the state transition matrix. This matrix can be calculated from the dynamic matrix as (Grewal and Andrews, 2001):

$$\boldsymbol{\Phi}_k = e^{\boldsymbol{F}(t_k)dt} = \boldsymbol{I} + \boldsymbol{F}(t_k)dt + \frac{(\boldsymbol{F}(t_k)dt)^2}{2} + \cdots \tag{4-79}$$

Where dt is the rate of the INS and **I** is the identity matrix. In this thesis, this matrix is calculated using up to the second-order of the equation (3-3). Higher terms can be neglected without changes in the performance of the navigator. In the same way, the discrete-time noise sensor associated covariance matrix $\boldsymbol{Q}_k$ can be calculated following the following expression (Shin, 2005):

$$\boldsymbol{Q}_k \approx \frac{1}{2}\left[\boldsymbol{\Phi}_k \boldsymbol{G}(t_k)\boldsymbol{Q}(t_k)\boldsymbol{G}^{\boldsymbol{t}}(t_k) + \boldsymbol{G}(t_k)\boldsymbol{Q}(t_k)\boldsymbol{G}^{\boldsymbol{t}}(t_k){\boldsymbol{\Phi}_k}^t\right]dt \tag{4-80}$$

4.5.2. Measurement Model

In this work, the measurement vector $\boldsymbol{z}$ of the fusion filter is compound by the differences between the position and velocity of the GNSS+EGNOS measurements and the navigational solution. Also, this vector includes the difference between the heading measurements calculated through the magnetometer and the INS solution. In this way, the measurement vector is given by:

$$\boldsymbol{z} = \begin{bmatrix} (R_M + h)\varphi_{INS} - \varphi_{GPS+EGNOS} \\ [(R_M + h)\cos(\varphi)]\lambda_{INS} - \lambda_{GPS+EGNOS} \\ h_{INS} - h_{GPS+EGNOS} \\ v_{INS} - v_{GPS+EGNOS} \\ \psi_{INS} - \psi_{Magnetometer} \end{bmatrix} \tag{4-81}$$

$$\boldsymbol{H} = \begin{bmatrix} R_M + h & 0 & 0 & & & & & \\ 0 & R_N + h & 0 & 0_{3x3} & & 0_{3x3} & & 0_{3x3} & 0_{3x3} \\ 0 & 0 & 1 & & & & & \\ & 0_{3x3} & & I_{3x3} & & 0_{3x3} & & 0_{3x3} & 0_{3x3} \\ & 0_{3x3} & & 0_{3x3} & \tan(\theta)\cos(\psi) & \tan(\theta)\sin(\psi) & 1 & 0_{3x3} & 0_{3x3} \end{bmatrix} \quad (4\text{-}82)$$

The term $R_M + h$ is introduced in the equations in order to solve numerical instabilities that could appear when the Kalman gain is calculated. These instabilities occur because the measurements of the latitude and longitude are very small values. Finally, the initial measurement noise covariance matrix is given by:

$$\boldsymbol{R}_{ini} = \begin{pmatrix} \sigma_{\varphi}^2 & 0 & 0 & 0 & 0 & 0 & 0 \\ 0 & \sigma_{\lambda}^2 & 0 & 0 & 0 & 0 & 0 \\ 0 & 0 & \sigma_h^2 & 0 & 0 & 0 & 0 \\ 0 & 0 & 0 & \sigma_{V_N}^2 & 0 & 0 & 0 \\ 0 & 0 & 0 & 0 & \sigma_{V_E}^2 & 0 & 0 \\ 0 & 0 & 0 & 0 & 0 & \sigma_{V_D}^2 & 0 \\ 0 & 0 & 0 & 0 & 0 & 0 & \sigma_{\psi}^2 \end{pmatrix} \quad (4\text{-}83)$$

The values for the individual weights of $\boldsymbol{R}_{ini}$ use to be initially fixed as the expected accuracy of the sensors in use. In this thesis, this matrix will be modified using the EGNOS protection levels; the modification of $\boldsymbol{R}_{ini}$ is presented in the following section 4.5.3

4.5.3. Improving the filter performance with EGNOS

In this section, it is presented a new strategy that allows improving the estimation filter accuracy through the modification in real-time of the Kalman matrices using the integrity parameters calculated through the EGNOS' integrity signals.

The accuracy and behavior of a Kalman filter rely on the values placed in the different covariance matrices. These values have to be found through a process that leads to an optimal result, and this is called tuning. The behavior of the filter as a result of the adjustment of the $\boldsymbol{Q}_{ini}$ and $\boldsymbol{R}_{ini}$ matrices is the following:

- The system noise or state covariance matrix Q provides the statistical description of the error model. A large value in Q indicates increased

parameter uncertainty and implies noisy estimations. During the prediction, if the uncertainty in the IMU data grows, the GNSS+EGNOS position estimation will correct the INS at a higher level. In other words, a large value in Q will cause the INS to closely follow the GPS position estimations. This, in turn, can lead to an inaccurate navigation solution, if the GPS estimations are noisy.

- How well the measurement noise is modeled is determined by the measurement noise covariance matrix R. Imperfect modeling of the noise of the measurement observables leads to a bad estimation quality. Choosing a large value for R reflects inaccurate and noisy measurements and might not correct the INS sufficiently. Otherwise, a small value implies an accurate measurement and it will cause the system to rely more on the measured data than on the model.

The uncertainty in the covariance parameters of Q and R has a significant impact on the performance of the Extended Kalman Filter (Salychev, 2004). These matrices directly influence the weight that the filter applies between the existing process information and the latest measurements. Errors in any of them may result in the filter being suboptimal or even cause it to diverge. In practice, the Q and R values are generally fixed and applied during the whole operation of the vehicle. Due to the process noise and measurement errors are dependent on the application environment and process dynamics, settings of the stochastic parameters have to be conservative in order to stabilize the filter for the worst-case scenario, which leads to performance degradation.

Here, the innovation of the system developed in this thesis is based on the utilization of the vertical and horizontal protection levels calculated from the EGNOS integrity messages for weighting the **Q** and **R** parameters. These levels can provide information to the fusion algorithm and be used for tunning their matrix gains. In this way, these protection levels perform a real-time adaptation of the matrices and, in this way, to change the behavior of the filter depending on the quality and accuracy information that EGNOS provides concerning the GPS satellites.

For using this new procedure in the estimation algorithm, the first step consists of performing the tuning of the $\boldsymbol{R}_{ini}$ and $\boldsymbol{Q}_{ini}$ matrices in the usual way. These matrices have the expressions introduced in eq. (4-77) and eq.(4-88).

Once these preliminary matrices have been chosen, it is possible to start using the EGNOS integrity information by weighting the values of $\boldsymbol{R}_{ini}$ and $\boldsymbol{Q}_{ini}$. In this way, we obtain two new matrices ($\boldsymbol{R}_{Egnos}$ and $\boldsymbol{Q}_{Egnos}$) which depend on the protection and the alarm levels.

$$\boldsymbol{R} = \boldsymbol{R}_{ini} * \boldsymbol{R}_{Egnos} \tag{4-84}$$

$$\boldsymbol{Q} = \boldsymbol{Q}_{ini} * \boldsymbol{Q}_{Egnos} \tag{4-85}$$

Where the new matrices have the following form:

$$\boldsymbol{R}_{Egnos} = \begin{pmatrix} \frac{HPL}{HUL} * rxy & 0 & 0 & 0 & 0 & 0 & 0 \\ 0 & \frac{HPL}{HUL} * rxy & 0 & 0 & 0 & 0 & 0 \\ 0 & 0 & \frac{VPL}{VUL} * rz & 0 & 0 & 0 & 0 \\ 0 & 0 & 0 & \frac{HPL}{HUL} * rxyv & 0 & 0 & 0 \\ 0 & 0 & 0 & 0 & \frac{HPL}{HUL} * rxyv & 0 & 0 \\ 0 & 0 & 0 & 0 & 0 & \frac{VPL}{VUL} * rzv & 0 \\ 0 & 0 & 0 & 0 & 0 & 0 & 1 \end{pmatrix} \tag{4-86}$$

$$\boldsymbol{Q}_{Egnos} = \begin{pmatrix} \frac{HUL}{HPL} * qh & 0 & 0 & 0 & 0 & 0 \\ 0 & \frac{HUL}{HPL} * qh & 0 & 0 & 0 & 0 \\ 0 & 0 & \frac{VUL}{VPL} * qa & 0 & 0 & 0 \\ 0 & 0 & 0 & 1 & 0 & 0 \\ 0 & 0 & 0 & 0 & 1 & 0 \\ 0 & 0 & 0 & 0 & 0 & 1 \end{pmatrix} \tag{4-87}$$

Where:

- HUL is the Horizontal User Level, it is a constant that the user imposes to the filter.
- HPL is the Horizontal Protection Level
- VUL is the Vertical User Level,it is a constant that the user imposes to the filter

- VPL is the Vertical Protection Level.
- rxy, rz, rxyv, rzv, qh and qa allows to give more or less importance to the integrity parameters. These parameters are imposed by the designer and must fulfill the following conditions:

$$\forall \tau_i > 0 \quad rxy, rz, rxyv, rzv = \begin{cases} \frac{1}{\tau_1} if \ \frac{HPL}{HUL} \leq 1 \\ \tau_2 \ if \ \frac{HPL}{HUL} > 1 \end{cases} \tag{4-88}$$

$$\forall \tau_i > 0 \quad qh, qa = \begin{cases} \frac{1}{\tau_3} if \ \frac{HPL}{HUL} > 1 \\ \tau_4 \ if \ \frac{HPL}{HUL} \leq 1 \end{cases} \tag{4-89}$$

Depending on these matrices, the behavior of the filter is the following:

- If the signals of the GPS and EGNOS satellites are available and are offering a good accuracy (protection levels are lower than the xUL field), then the weights of the elements of the matrix $\boldsymbol{R}_{Egnos}$ are smaller and the elements of the matrix $\boldsymbol{Q}_{Egnos}$ become bigger. In this case, the filter relies more in the measurement model than in the system model, so the outputs are corrected following the GPS+EGNOS measurements.
- If the protection levels are higher than the alarm xUL field, then the weights of the variances of the matrix $\boldsymbol{R}_{Egnos}$ are increased because the confidence on the GPS+EGNOS signal decreases. In this situation, the values of $\boldsymbol{Q}_{Egnos}$ become smaller, the inertial sensors gain importance in the estimation and the measurement model corrects the outputs of the filter in a softer way.
- If the receiver is not receiving the EGNOS signals, then the matrix $\boldsymbol{R}_{Egnos}$ and the matrix $\boldsymbol{Q}_{Egnos}$ remain constants with the weights calculated in the initial tuning procedure ($\boldsymbol{R}_{ini}$ and $\boldsymbol{Q}_{ini}$).

Figure 4-7 shows a summary of the real-time tuning process.

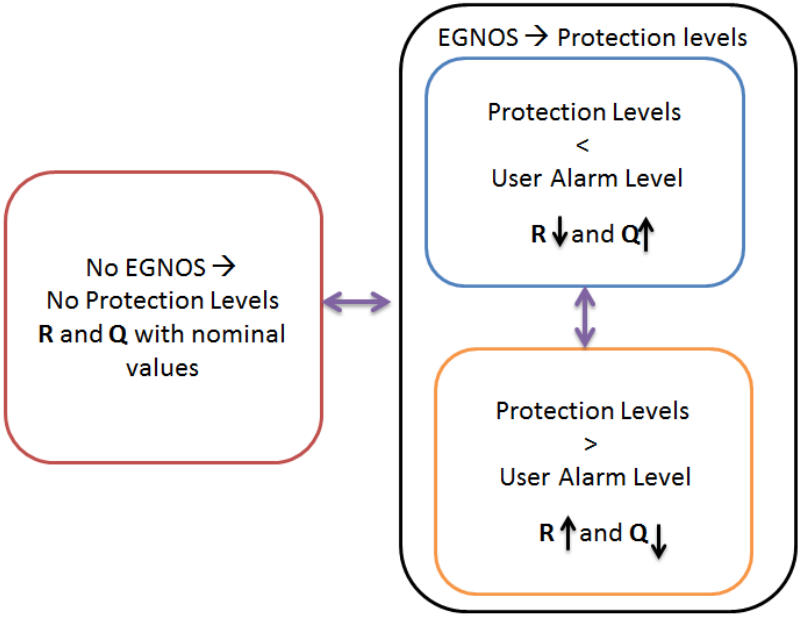

Figure 4-7: New Tuning procedure using the EGNOS protection levels.

4.6. Conclusions

In this chapter, it has been presented the EIRE navigator system. This navigator is used for the take-off and waypoint navigation phases of the autonomous mission. Here, two fusion integrations strategies are presented: The Tighly Coupled and the Loosely Coupled schemes. From the characteristics of both of them, it is concluded that the Loosely Coupled scheme is the most appropriate architecture for the navigator developed in this thesis. This is due to the LC processing time is faster than the obtained with the TC architecture, and also, due to the implementation of the LC architecture is more straightforward than the TC one, making possible to

add more sensors to the fusion filter in a faster way.

Through this chapter, it is also derived the navigation and mechanization equations of the Inertial Navigation System. This derivation is done because the EKF that is running in the EIRE navigation algorithm has been built by perturbing the kinematics equations. In this filter it was decided to add the bias in the state vector by modeling this error as a Gaussian Markov process. Although the turn-on bias could be added also to this filter, it is concluded that this error can be removed from the navigational solution with an initial calibration stage and, in this way, the filter is reduced by 6 dimensions.

Finally, this chapter presents a new strategy that improves the performance of the fusion filter in real-time by using the protection level information provided by the EGNOS sensor.

5. GNSS-FREE RELATIVE NAVIGATION SYSTEM

The accuracy provided by usual algorithms, most of them based on fusing a GNSS sensor with an INS, it is not typically enough to perform a safe approach and landing, especially in moving platforms. Therefore a new technique to estimate the position in real-time with high accuracy is needed to successfully accomplish with these maneuvers in an autonomous and safe way. In this work, two new relative estimators have been developed and implemented in an autonomous helicopter for their use during the approach and landing phases on both static and mobile platforms. The main differences between these estimators are based on the sensor that they use as the source of the positioning relative measurements, and the transformations needed to convert these measurements to the frame in which the fusion algorithm is working. In Figure 5-1, it is shown the architecture of the **T**ether –based **G**NSS-free **R**el**A**tive **N**aviga**T**or (T-GRANT) module. As it can be seen, the inputs to this module are the data provided by the tether system (angles η, λ and tension of the tether T), the altitude of the altimeter h_{alt}, the accelerations and angular velocities of the INS ($\mathbf{a}^b$, $\boldsymbol{\omega}$) and the magnetic field measurements of the magnetometer ($\mathbf{m}^b$).

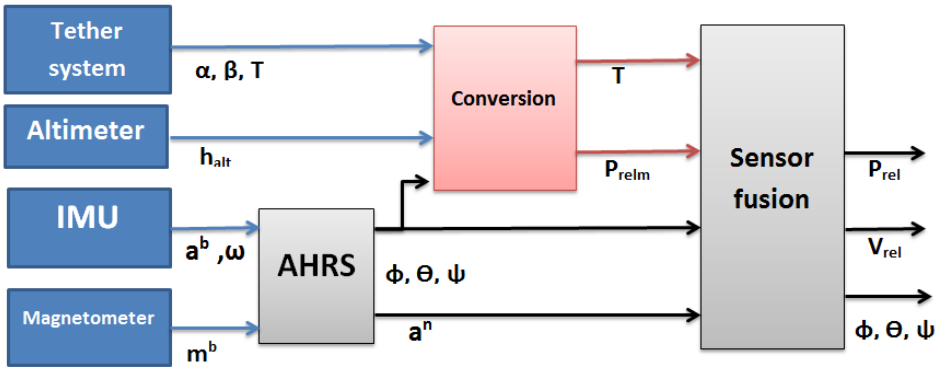

Figure 5-1: Architecture of the T-GRANT module

In Figure 5-2, it is shown the architecture of the Radiobeacon –based **G**NSS-free **R**el**A**tive **N**aviga**T**or (R-GRANT). The inputs to this module are the relative position to the landing platform provided by the radio-beacon system ($\boldsymbol{p}_r^{rb}$), the altitude measured by the altimeter sensor, the accelerations and angular velocities of the INS integrated into the helicopter($\mathbf{a}^b$, $\boldsymbol{\omega}^b$) and the magnetic field measurements of the magnetometer ($\mathbf{m}^b$).

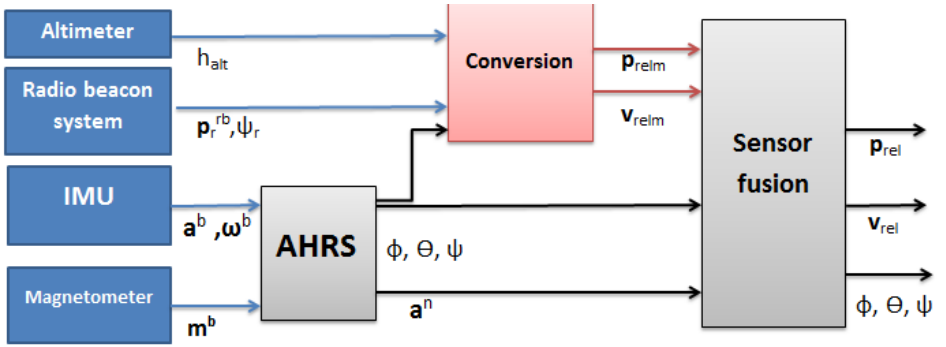

Figure 5-2: Architecture of the R-GRANT

In the schemes presented in Figure 5-1 and Figure 5-2, leaving apart the sensors, it is possible to see that the navigators are built mainly by three different blocks:

- Attitude and Heading Reference System (AHRS) block: This is the module in charge of calculating the attitude of the UAV (roll ϕ, pitch θ and yaw ψ). The attitude is defined as the inclination of its body-axes reference frame to the navigation reference frame. Also in this block, the accelerations are rotated to the navigation axes ($\mathbf{a}^n$) in order to be used in the fusion algorithm.
- Conversion blocks This block performs all the geometric and rotation operations needed to transform the raw measurements of the RBS or tether device to a relative position vector (P_{rel}) expressed in the navigational frame.
- Sensor Fusion: This block fuses all the information obtained from the AHRS and the conversion block, and estimates the relative state vector that will be used by the controller of the RUAV.

While the AHRS system is the same for both architectures, the conversion block and the measurement model of the fusion filter of these estimators are different. In this section, these blocks are derivated for both navigators.

5.1. Thresholded and Weighted by Accelerations AHRS

The Attitude and Heading Reference System is the module in charge of calculating the attitude of the UAV. In this thesis, a new algorithm has been developed departing from the proposed by Setoodeh in (Setoodeh, Khayatian and Frajah, 2004) and improving it by introducing a new criteria for building the measurement vector. This new algorithm has been called the TWA (Threshold and Weighted by Accelerations) AHRS algorithm. In this filter, the angular rate measurements obtained from the gyroscopes ($\boldsymbol{\omega}_{\mathbf{ib}}^{\mathbf{b}}$) are used for updating the previous attitude estimation. In this case, the attitude is parameterized with unitary quaternion and calculated by using quaternion kinematics equations.

$$q_k = q_{k-1} + \dot{q}_k \tag{5-1}$$

$$\dot{q} = \frac{1}{2}\begin{bmatrix} q_0 & -q_1 & -q_2 & -q_3 \\ q_1 & q_0 & -q_3 & q_2 \\ q_2 & q_3 & q_0 & -q_1 \\ q_3 & -q_2 & q_1 & q_0 \end{bmatrix}\begin{bmatrix} 0 \\ \boldsymbol{\omega}_{\mathbf{nb}}^{\mathbf{b}} \end{bmatrix} \tag{5-2}$$

After updating the previous attitude solution with the gyroscope measurements, the resulting estimation is corrected using an Extended Kalman Filter. The goal of this EKF is to estimate the attitude errors in the current attitude estimation to remove them. For this purpose, the attitude error is used as the state vector. Once the attitude error is estimated, the attitude solution is corrected to remove the error. After this, the attitude error can be assumed to be zero so the state vector is set to zero. The measurements of the attitude errors of the current attitude estimation are obtained using the measurements provided by the auxiliary sensors (i.e. the accelerometers and the magnetometer). The magnetometer measurements are used to calculate the yaw angle of the RPAS and the difference between this value and the current estimation is used as the measurement of the yaw error. In a similar way, the outputs of the accelerometers are used to calculate the measurements of the roll and pitch errors. Nevertheless, the accelerometers only can be used for this

calculation when the UAV is in a non-accelerated state, it is to say, a situation where the gravity is the only force that acts in the vehicle. When this condition is fulfilled, the measured acceleration in the body frame can be compared with the gravity acceleration in the navigation frame and then the roll and pitch angles are calculated. Hereby, EKF measurement cycle is always running for the yaw error component (obtained from the magnetometer), but it only runs for the roll and pitch error components when the measured acceleration in the navigation frame is close enough to the gravity.

The state vector of this filter is built using the Euler angular errors measured in the body frame. This formulation removes the angular rates from the state vector and neither requires the use of a dynamic model. These angular errors are expressed as $\varepsilon = [\delta\phi \quad \delta\theta \quad \delta\psi]^T$, so the state vector can be denoted as $x = \varepsilon$. By linearizing the kinematics equations of the Euler angles (eq. (5-3)) it is possible to obtain the dynamic matrix of the angular errors (eq.(5-4)).

$$\begin{bmatrix} \dot{\phi} \\ \dot{\theta} \\ \dot{\psi} \end{bmatrix} = \begin{bmatrix} 1 & sin\phi tan\theta & cos\phi tan\theta \\ 0 & cos\phi & -sin\phi \\ 0 & sin\phi/cos\theta & cos\phi/cos\theta \end{bmatrix} \boldsymbol{\omega}_{\boldsymbol{bn}}^{\boldsymbol{b}} \tag{5-3}$$

$$\boldsymbol{F} = \begin{bmatrix} tan\theta(\omega_y cos\phi - \omega_z sin\phi) & (1 + (tan\theta)^2)(\omega_y sin\phi + \omega_z cos\phi) & 0 \\ -(\omega_y sin\phi + \omega_z cos\phi) & 0 & 0 \\ (\omega_y cos\phi - \omega_z sin\phi)/cos\theta & tan\theta(\omega_y sin\phi + \omega_z cos\phi)/cos\theta & 0 \end{bmatrix} \tag{5-4}$$

Where sθ, cθ and tθ denote the sine, cosine, and tangent of the angle θ respectively while ω_x, ω_y and ω_z are the components of the angular velocity between the body and the navigation frame $\boldsymbol{\omega}_{bn}^{b}$.

In order to build the measurement vector of the Kalman Filter, it is used the difference between the estimated attitude angles ($\hat{\phi}$, $\hat{\theta}$ and $\hat{\psi}$) and the angles calculated through the accelerometers and magnetometers (ϕ_m, θ_m and ψ_m), so the measurement matrix is a 3x3 identity matrix. The measurement vector is expressed as:

$$\boldsymbol{z} = \boldsymbol{\varepsilon} = [\phi_m - \hat{\phi} \quad \theta_m - \hat{\theta} \quad \psi_m - \hat{\psi}] \tag{5-5}$$

Due to the attitude only can be calculated accurately from the accelerometers if there are no forces perturbing the aerial vehicle (excepting the gravity), when the

acceleration values are bigger than the gravity module plus a threshold parameter, only the heading is corrected. This threshold has been chosen through comparison of the results obtained reproducing a lot of real telemetry data using different values for the filter parameters. From these results, it has been obtained that the best value was 0.04g. The correction of the heading is performed by using the measures of the magnetometers m_x, m_y and m_z and the magnetic declination angle D :

$$\psi_m = -\tan^{-1}\left(\frac{m_y^b cos\phi - m_z^b sin\phi}{m_x^b cos\theta + m_y^b sin\theta sin\phi + m_z^b sin\theta c\phi}\right) + D \tag{5-6}$$

When the total acceleration module is under g + threshold ($|a^b| \leq g + 0.04$), the roll and pitch can be calculated from the accelerometers and included in the measurement vector. These angles can be calculated by using the components of the acceleration in the body frame a_x, a_y and a_z:

$$\phi_m = tan^{-1}(a_y^b/a_z^b) \tag{5-7}$$

$$\theta_m = tan^{-1}(a_x^b/\sqrt{\left(a_y^b\right)^2 + (a_z^b)^2}) \tag{5-8}$$

In the developed TWA algorithm, the difference between the acceleration module and the gravity is also used to weight the measurement matrix of the EKF. In this way, when the acceleration module is closer to the gravity vector, the filter confides more in the accelerometers measurements. On the other hand, if the difference between the module of the acceleration and the gravity is closer to the threshold, the correction of the filter is lower. In this way, the measurement matrix $\boldsymbol{R}_{TWA}$ is built following :

$$\begin{aligned} &\text{if } |a^b| - g > threshold \quad \xrightarrow{yields} \quad \boldsymbol{R}_{TWA} = r\psi \\ &else\ if\ |a^b| - g < threshold \quad \xrightarrow{yields} \quad \boldsymbol{R}_{TWA} = \begin{pmatrix} r_\phi \frac{|a^b| - g}{threshold} k_e & 0 & 0 \\ 0 & r_\theta \frac{|a^b| - g}{threshold} k_e & 0 \\ 0 & 0 & r_\psi \end{pmatrix} \end{aligned} \tag{5-9}$$

where r_ϕ , r_θ and $r\psi$ are constant values calculated using a normal tuning

procedure without using the weight parameters and k_e is a constant that allows weighting the result provided by $\frac{|a^b|-g}{threshold}$. These values have been chosen in a post-processing phase by using telemetry data obtained in real flights and comparing the results obtained by using for the different parameters.

Once the a-posteriori attitude error is obtained, the current attitude estimation is corrected by using the following equation:

$$\boldsymbol{R}_{\boldsymbol{n}}^{\boldsymbol{b}}(+) = (\boldsymbol{I} - \mathit{skew}(\hat{\boldsymbol{x}}(+)))\boldsymbol{R}_{\boldsymbol{n}}^{\boldsymbol{b}}(-) \tag{5-10}$$

In eq.(5-10), $\boldsymbol{R}_{\boldsymbol{n}}^{\boldsymbol{b}}$(-) and $\boldsymbol{R}_{\boldsymbol{n}}^{\boldsymbol{b}}$(+) are the rotation matrices corresponding to the current attitude estimation before and after the correction respectively, and $\mathit{skew}(\boldsymbol{v})$ denotes the skew-symmetric matrix of vector $\boldsymbol{v}$ which is given by

$$\text{skew}(\mathbf{v}) = \begin{bmatrix} 0 & -v_3 & v_2 \\ v_3 & 0 & -v_1 \\ -v_2 & v_1 & 0 \end{bmatrix} \tag{5-11}$$

5.1.1. Accuracy comparison of the TWA-AHRS

In this section, the TWA-AHRS presented previously is compared with other algorithms that are commonly used in navigation and with a commercial system. Comparison has been performed against the Setoodeh algorithm (Setoodeh, Khayatian and Frajah, 2004), the Han's AHRS algorithm(Han and Wang, 2011) and the Xsens MTi-G commercial AHRS system (XSENS, 2019).

For assessing the accuracy of the AHRS systems, their attitude estimations need to be compared with the attitude values that are considered to be a true reference. In this work, a multi-camera based location system from VICON Motion System Ltd (VICON, 2019) has been used to obtain the true attitude reference. This system is composed of 20 cameras installed in a 15m x 15m x 5m testbed (see Figure 5-3).VICON system estimates the attitude of the object from the infra-red radiation emitted by the cameras and reflected from passive markers which have been attached to the object. This system can estimate the position of each marker with sub-millimetric accuracy and the attitude of the object with an accuracy of less than a tenth of degree so it has been considered to be a good system for attitude true

reference.

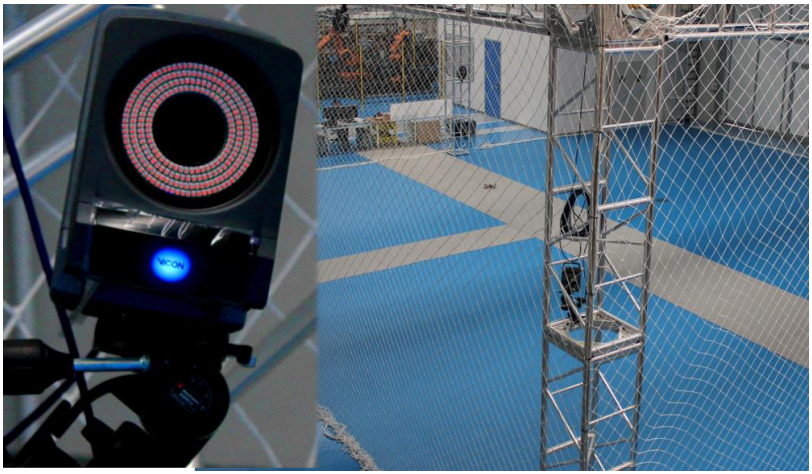

Figure 5-3: VICON camera and indoor testbed

To perform the comparison, the Xsens MTi-G was mounted on a rigid board to which VICON markers were attached. Tests consisted of moving this table by hand along the testbed for about ten minutes. These experiments were repeated ten times with different profiles of the acceleration and angular velocities. During these tests, it was logged the raw measurements and the attitude estimations provided by the Xsens MTi-G together with the attitude estimation provided by the VICON system.

The accuracy of the three tested AHRS algorithms and the AHRS algorithm of the Xsens MTi-G system are compared using the attitude estimation of the VICON system as the true reference. For obtaining the attitude solutions, the raw measurements of Xsens MTi-G inertial and magnetic sensors have been fed into Simulink implementations of the different AHRS algorithms. In this way, all the algorithms use the same sensors and the performance of the solution only depend on the filter implementation.

Figure 5-4 to Figure 5-6 show the attitude estimations obtained for the different algorithms during one experiment. These figures are only intended to provide visual information of the AHRS outputs. In these graphs the blue line is the VICON measurements (ground-truth), the green line is the Xsens attitude outputs, the red line is the attitude solution of the TWA-AHRS developed in this thesis, the cyan line is the Setoodeh AHRS solution and the purple line is the Wang AHRS solution.

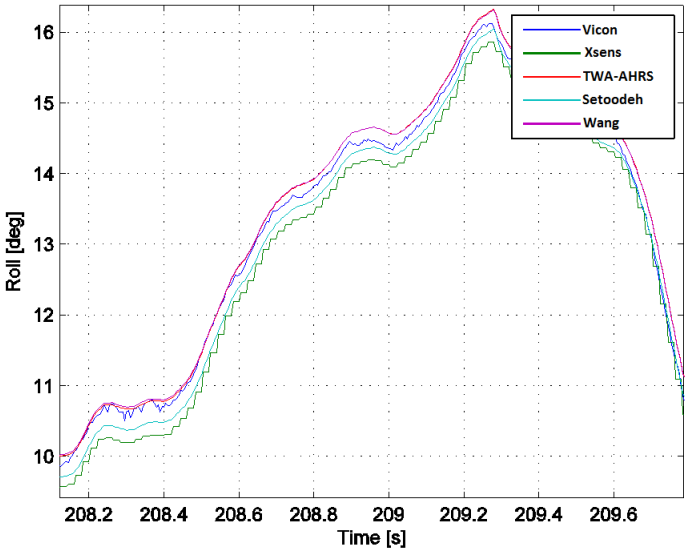

Figure 5-4 Roll comparison of the different AHRS algorithms.

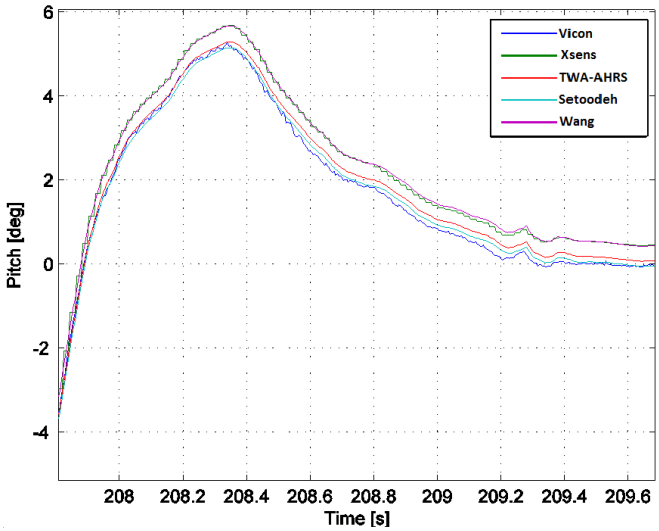

Figure 5-5 Pitch comparison of the different AHRS algorithms

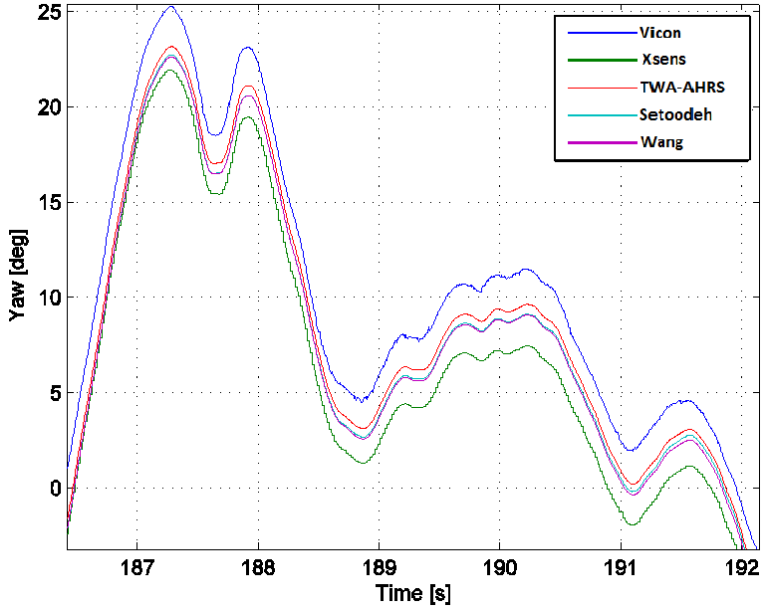

Figure 5-6: Yaw comparison of the different AHRS algorithms

Next, from Table 5-1 to Table 5-3, it is shown the root mean square (RMS) error and the standard deviation (STD) of the different solutions compared with the ground truth (VICON calculations).

AHRS	Roll accuracy of AHRS Algorithms	
	Mean error (RMS) [deg]	Standard deviation [deg]
TWA-AHRS	0.45	0.62
Setoodeh	0.50	0.72
Wang	0.43	0.63
Xsens MTi-G	0.54	0.67

Table 5-1: Comparison of the roll accuracy

AHRS	Pitch accuracy of AHRS Algorithms	
	Mean error (RMS) [deg]	Standard deviation [deg]
TWA-AHRS	0.55	0.67
Setoodeh	0.71	0.82
Wang	0.57	0.67
Xsens MTi-G	0.78	0.61

Table 5-2: Comparison of the pitch accuracy

AHRS	Yaw accuracy of AHRS Algorithms	
	Mean error (RMS) [deg]	Standard deviation [deg]
TWA-AHRS	1.23	0.99
Setoodeh	1.76	1.20
Wang	1.78	1.15
Xsens MTi-G	3.09	1.48

Table 5-3: Comparison of the yaw accuracy

It can be seen from Table 5-1 to Table 5-3 that the TWA-AHRS and the Wang algorithm provide better accuracies when estimating the roll and pitch angles than the obtained with the Setoodeh's algorithm and the one calculated by the Xsens MTi-G system. In addition, the TWA-AHRS algorithm provides the best accuracy in comparison with the other three algorithms in the heading estimation. Hence, through the results obtained in these experiments, it can be concluded that the algorithm developed in this thesis provides the best overall accuracy when it is compared with some of the most common AHRS used in navigation.

5.2. Conversión block: Tether Measurements

In order to obtain the measurement vector by using the tether, some calculations and transformation have to be performed over the raw measurements of the sensor. In Figure 5-7, it is shown the different elements that are used by the Tether Calculation Block (see Figure 5-1) for the computation of the vector **z**. In this figure:

the center of gravity of the RUAV is presented as CG; the contact point (CP) is the location where the tether system is installed in the fuselage of the UAV; h_{al} is the altitude above ground level (AGL) measured by the altimeter, h_{cp} is the AGL in the CP, l_t is the distance to the landing point O, l_{cg} is the lever arm between the CG and the CP, and l_{alt} is the lever-arm between the CP and the altimeter. For the sake of clarity, in Figure 3-1 it was shown a model of this device with the tether and body coordinate systems represented over it.

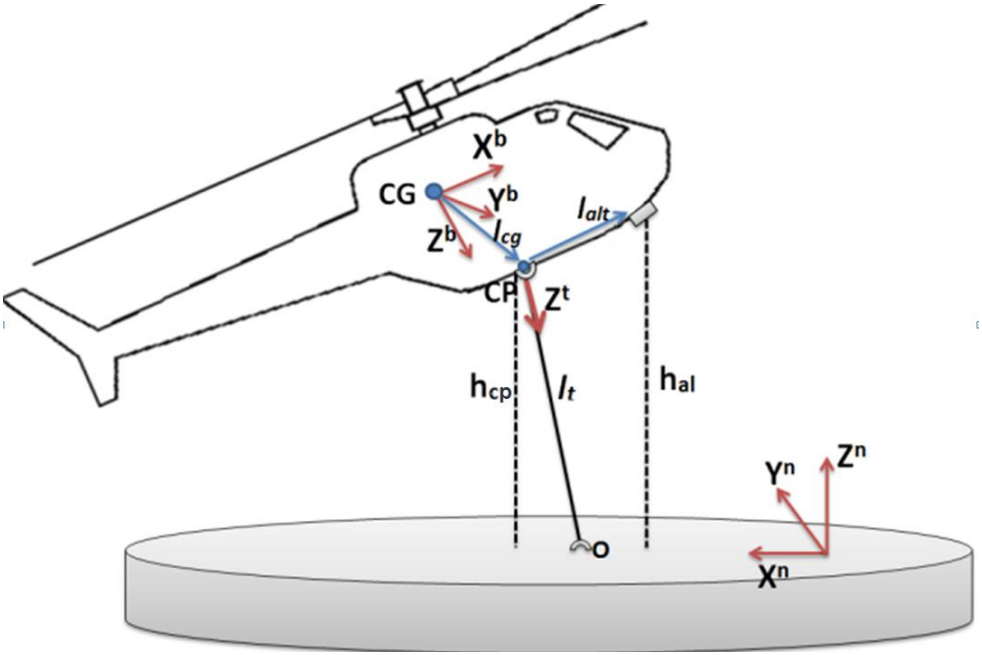

Figure 5-7: Landing scenario frames and elements that play a relevant role in the landing procedure based on the tether device.

The first step for obtaining the relative positioning measurements consists of calculating the altitude to the landing point from the contact point. Since the altimeter is not installed in the same location than the CP and looking for the highest possible accuracy, it is necessary to correct the lever arm according to the following equations:

$$\mathbf{R}_b^n = \left(\mathrm{R}_n^b\right)^t = \begin{pmatrix} c\theta c\psi & -c\phi s\psi + s\phi s\theta c\psi & s\phi s\psi + c\phi s\theta c\psi \\ c\theta s\psi & c\phi c\psi + s\phi s\theta s\psi & -s\phi c\psi + c\phi s\theta s\psi \\ -s\theta & s\phi c\theta & c\phi c\theta \end{pmatrix} \tag{5-12}$$

$$h_{CP} = h_{al} - \mathbf{R}_b^n(3,:)l_{alt} = h_{al} - s\theta l_x + s\phi c\theta l_y + c\phi c\theta l_z \tag{5-13}$$

where R_b^n is the rotation matrix from the body to the navigation frame calculated in the AHRS block and "c" and "s" denotes cosine and sine respectively. The cardan joint is rigidly attached to the helicopter and perfectly aligned with the X^b and Y^b body axes of the vehicle. This device rotates η and ϱ angles with respect to the helicopter fuselage around its X^b and Y^b axes respectively, so the rotation matrix from the tether to the body frame is

$$\mathbf{R}_t^b = \begin{pmatrix} c\beta & 0 & -s\beta \\ -s\alpha s\beta & c\alpha & -s\alpha c\beta \\ c\alpha s\beta & s\alpha & c\alpha c\beta \end{pmatrix} \tag{5-14}$$

Once the altitude h_{CP} has been calculated, it is necessary to compute the relative position in navigation axes from the CP to the landing point as:

$$\mathbf{p}_{CP}^n = \mathbf{R}_b^n \mathbf{R}_t^b \mathbf{p}_{CP}^t = \mathbf{R}_t^n \mathbf{p}_{CP}^t \tag{5-15}$$

where $\mathbf{p}_{CP}^n$ and $\mathbf{p}_{CP}^t$ are the positions vectors of the contact point in the navigation and the tether frames respectively. In the tether frame, the horizontal XY coordinates of the landing point are equal to 0, therefore the position vector in this location can be expressed as $[0, 0, z^t]$ and eq.(5-15) can be re-written as:

$$\begin{pmatrix} x_{CP}^n \\ y_{cp}^n \\ h_{CP} \end{pmatrix} = \mathbf{R}_t^n \begin{pmatrix} 0 \\ 0 \\ z^t \end{pmatrix} \tag{5-16}$$

By using the eq.(5-16), it is possible to obtain the relative coordinates of the contact point in the navigation frame as:

$$z^t = \frac{h_{CP}}{\mathbf{R}_t^n(3,3)} = \frac{h_{CP}}{s\theta s\beta - s\phi c\theta s\alpha c\beta + c\phi c\theta c\alpha c\beta} \tag{5-17}$$

$$x_{CP}^{n} = \mathbf{R}_{t}^{n}(1,3)z^{t} = (s\alpha c\beta(c\phi s\psi - s\phi s\theta c\psi) + c\alpha c\beta(s\phi s\psi + c\phi s\theta c\psi) - s\beta c\theta c\psi)z^{t} \quad (5\text{-}18)$$

$$y_{CP}^{n} = \mathbf{R}_{t}^{n}(2,3)z^{t} = (c\alpha c\beta(c\phi s\theta s\psi - s\phi c\psi) - c\theta s\psi s\beta - (c\phi c\psi + s\phi s\theta s\psi)s\alpha c\beta)z^{t} \quad (5\text{-}19)$$

The last step is to translate this relative position to the center of mass of the vehicle. This operation is done by applying another lever arm correction:

$$\mathbf{p}^{n} = \boldsymbol{p}_{CP}^{n} - \mathbf{R}_{b}^{n}\mathbf{l}_{CG} \quad (5\text{-}20)$$

5.3. Conversión block: Radio-beacon Measurements

In order to obtain the measurement vector by using the radio-beacon sensor, some calculations and transformation have to be performed over the raw measurements. The radio-beacon system provides relative positioning on its local north, which is determined by the location of the Ground Station Coordinates. This local north must be corrected for the estimation algorithm of the helicopter, which works in absolute North-West coordinates. Hence, the orientation of the platform should be provided during the whole operation to be able to correct and convert the relative positioning to the required navigational frame. For this purpose, different strategies are possible:

- An AHRS integrated on the landing deck sending through a radio channel the attitude of the landing platform to the UAV. In this way, the helicopter is able to compute the relative orientation of the ship and corrects the relative positioning measurement provided by the RBS. However, in this work, this approach has been discarded because the navigator of the RPA cannot rely on a communication channel.
- The relative orientation of the landing platform with respect the helicopter could be calculated by using vision algorithms. Comparing this orientation with the calculated by the onboard navigator, it should be possible to correct the relative measurements of the radio-beacon system. Although this is a suitable approach, and it could provide a very good performance, in this thesis vision techniques have not been taken into consideration.
- Integrating two antennas in the helicopter. In this way, the Range

Measurement Unit (see section 3.2.2) is able off computing the range measurements to the landing platform from both antennas and calculates the relative orientation between the ship and the helicopter.

Figure 5-8 presents the different relations used by the Calculation Block that was shown in Figure 5-2 for the computation of the vector **z**. In this figure, CG is the center of gravity of the helicopter, ψ^{rbs} is the angle between the radio-beacon system and the navigation frame, la_{rbs} is the lever-arm between the CG and the antenna of the radio-beacon receiver, and la_{alt} is the lever-arm between the CG of the vehicle and the altimeter sensor.

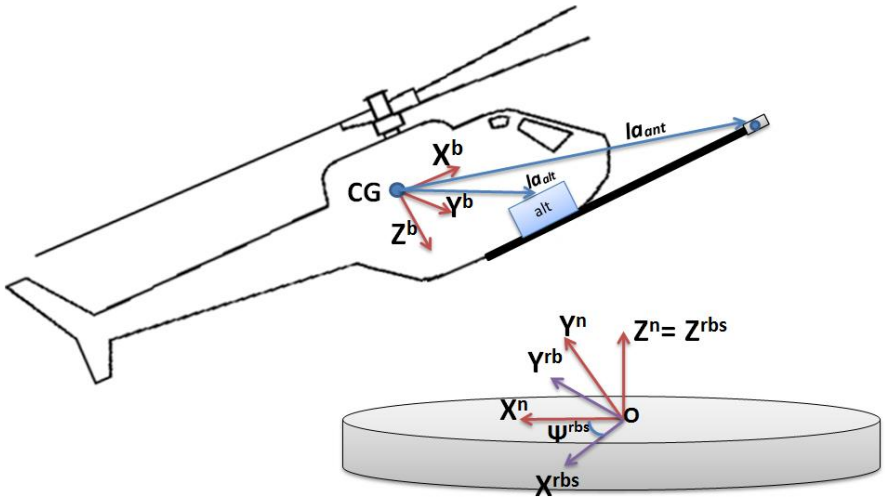

Figure 5-8: Landing scenario frames and elements that play an important role in the landing procedure based on the radio-beacon device.

For obtaining the relative positioning vector, it is necessary to calculate the relative position vector of the antenna radio-beacon receiver (p_{rbs}^{rbs}) in the navigation frame (p_{rbs}^{n}). In order to do this, it is necessary to rotate the measurements of the integrated device by the angle ψ^{rb} . This can be done solving the following equation

$$\boldsymbol{p}_{rbs}^{n} = \begin{pmatrix} c\psi^{rb} & sc\psi^{rb} & 0 \\ -c\psi^{rb} & c\psi^{rb} & 0 \\ 0 & 0 & 0 \end{pmatrix} \boldsymbol{p}_{rbs}^{rbs} \tag{5-21}$$

Once the antenna's position has been expressed in the navigational frame, it is necessary to apply lever-arm corrections to the radio-beacon calculated position and to the altimeter sensor for obtaining the relative distance of the landing point to the helicopter 's CG. In the particular case of this work, this step is essential due to the radio-beacon antenna receiver was integrated with a separation from the CG greater than one meter. In this way, the relative vector used by the fusion algorithm can be calculated as:

$$\mathrm{x_{CP}} = \boldsymbol{x}_{rbs}^{n} - \mathrm{c\theta c\psi l_{rbs,x}} + (-\mathrm{c\phi s\psi} + \mathrm{s\phi s\theta c\psi})\mathrm{l_{rbs,y}} + (\mathrm{s\phi s\psi} + \mathrm{c\phi s\theta c\psi})\mathrm{l_{rbs,z}} \tag{5-22}$$

$$\mathrm{y_{CP}} = \boldsymbol{y}_{rbs}^{n} - \mathrm{c\theta s\psi l_{rbs,x}} + (\mathrm{c\phi c\psi} + \mathrm{s\phi s\theta s\psi})\mathrm{l_{rbs,y}} + (-\mathrm{s\phi c\psi} + \mathrm{c\phi s\theta s\psi})\mathrm{l_{rbs,z}} \tag{5-23}$$

$$\mathrm{h_{CP}} = \mathrm{h_{al}} - \mathrm{s\theta l_{alt,x}} + \mathrm{s\phi c\theta l_{alt,y}} + \mathrm{c\phi c\theta l_{alt,z}} \tag{5-24}$$

5.4. Fusion Filter block: System model

In this section, it is presented a new system model for the estimation of relative motions. The developed model has used a Singer model as a basis and has extended and improved it for the application treated in this thesis. The Singer acceleration model (Singer, 1970) is a popular model (see (Cloutier, Evers and Feeley, 1989), (Blackman and Popoli, 1999) and (Bar-Shalom, Li and Kirubarajan, 2001)) for target maneuvers that characterizes the unknown target acceleration as a time-correlated stochastic process. It was the first model in characterizing the unknown target acceleration as a time-correlated (i.e., colored) stochastic process. It is an a priori model since it does not use online information about the target maneuver, although it can be made adaptive through an adaptation of its parameters. In the Singer model, the acceleration is modeled as a zero-mean first-order stationary Markov process with an autocorrelation function (Rong Li and Jilkov, 2003):

$$R_a(\tau) = E[a(t+\tau)a(t)] = \sigma^2 e^{-\alpha|\tau|} \tag{5-25}$$

where σ^2 is the variance process noise and α is the reciprocal of a maneuver time constant τ that depends on how long the maneuver lasts. For instance, in a slow turn of an aircraft $\tau \sim 60s$ and in an evasive maneuver $\tau \sim 10 - 20s$ (see (Singer, 1970)). In a Markov process, the value at a given time depends on values at other times only through its nearest neighbors. In this work, in order to provide values for these parameters, some assumptions for the ship model were taken (see(Rapatz, 1991) and (Price and Bishop, 1974)): Regarding the landing platform, it is supposed that it follows a straight trajectory with (nearly) constant velocity. Regarding the helicopter, it is assumed that the autopilot is able of following the ship in a soft way during the maneuver (this last assumption was proved through the results of the tests campaigns that are described in chapter 6).

One of the shortcomings of the Singer model is that the acceleration has a zero mean at any moment (Rong Li and Jilkov, 2003). However, due to in our application is possible to use the information of the inertial sensors onboard the RUAV, this model has been modified in a new way that overcomes this limitation and improves the results obtained in the estimation module. In the landing scenario, as the ship is assumed to have a slow dynamic, most of the changes in the relative velocity between both vehicles are due mainly to the accelerations of the helicopter. These accelerations are not zero and can be measured by the accelerometers onboard. Hence, the Singer model is modified to have a non-zero mean of the acceleration. This approach is more effective than the Singer model because it includes in the model most of the dynamics of the relative motion, which is that associated with the helicopter accelerations. In this way the acceleration model satisfies:

$$a(t) = \tilde{a}(t) + \bar{a}(t) \tag{5-26}$$

where $\bar{a}(t)$is the mean acceleration of the helicopter in the navigation frame, which is assumed to be constant during the sampling period. On the other hand $\tilde{a}(t)$is the zero-mean Markov process of the Singer model, with the autocorrelation function showed in eq.(5-25) and it satisfies

$$\dot{\tilde{a}}(t) = -\alpha\tilde{a}(t) + w(t) \tag{5-27}$$

In eq.(5-27), w(t) is modeled as a zero-mean white noise. If $\tilde{a}(t)$ is expressed in eq. (5-26) and plugged in eq.(5-27), it is possible to obtain

$$\dot{\tilde{a}}(t) = -\alpha a(t) + \alpha \bar{a}(t) + w(t) \tag{5-28}$$

If we note from eq. (5-26) that $\dot{\tilde{a}}(t) = \frac{\partial}{\partial t}(a(t) - \bar{a}(t))$ and it is assumed that the acceleration of the helicopter $\bar{a}(t)$ is constant over a sampling interval Ts, we obtain:

$$\dot{a}(t) = -\alpha a(t) + \alpha \bar{a}(t) + w(t) \tag{5-29}$$

Through eq.(5-29) it is possible to write the complete stochastic differential equation as:

$$\dot{\boldsymbol{x}}(t) = \begin{pmatrix} 0 & 1 & 0 \\ 0 & 0 & 1 \\ 0 & 0 & -\alpha \end{pmatrix} \boldsymbol{x}(t) + \begin{pmatrix} 0 \\ 0 \\ \alpha \end{pmatrix} \bar{a}(t) + \begin{pmatrix} 0 \\ 0 \\ 1 \end{pmatrix} \boldsymbol{w}(t) \tag{5-30}$$

In eq.(5-30), **x(t)** is the relative state vector [pr(t),vr(t),ar(t)] where pr(t), vr(t) and ar(t) are the relative position, velocity and acceleration respectively. By applying a standard discretization step in eq.(5-30)(5-43), it is possible to obtain the discrete state equation:

$$\mathbf{F}_\alpha = \begin{bmatrix} 1 & T & \frac{1}{\alpha^2}(\alpha T_s - 1 + e^{-\alpha T_s}) \\ 0 & 1 & \frac{1}{\alpha}(1 - e^{-\alpha T_s}) \\ 0 & 0 & e^{-\alpha T_s} \end{bmatrix} \tag{5-31}$$

$$\mathbf{U}_\alpha = \begin{bmatrix} \frac{-T_s + \frac{\alpha T^2}{2} + 1 - \frac{e^{-\alpha T_s}}{\alpha}}{\alpha} \\ T - \frac{1 - e^{-\alpha T_s}}{\alpha} \\ 1 - e^{-\alpha T_s} \end{bmatrix} \tag{5-32}$$

$$\mathbf{Q}(k) = E(\mathbf{w}(k)\mathbf{w}^T(k)) = 2\alpha{\sigma_\alpha}^2 \begin{bmatrix} q_{11} & q_{12} & q_{13} \\ q_{12} & q_{22} & q_{23} \\ q_{13} & q_{23} & q_{33} \end{bmatrix} \tag{5-33}$$

where the terms of the process noise covariance matrix (a similar methodology can be found in (Peng, Yang and Liu, 2015) and (Kristan et al., 2010) where a velocity

model is derived) are given by:

$$
\begin{aligned}
q_{11} &= \frac{1}{2\alpha^5}\left(1 - e^{-2\alpha T_s} + 2\alpha T_s + \frac{2\alpha^3 {T_s}^3}{3} - 2\alpha^2 {T_s}^2 - 4\alpha T_s e^{-\alpha T_s}\right) \\
q_{12} &= \frac{1}{2\alpha^4}\left(e^{-2\alpha T_s} + 1 + 2e^{-\alpha T_s} + 2\alpha T_s e^{-\alpha T_s} - 2\alpha T_s - \alpha^2 {T_s}^2\right) \\
q_{13} &= \frac{1}{2\alpha^3}(1 - e^{-2\alpha T_s} - 2\alpha T_s e^{-\alpha T_s}) \\
q_{22} &= \frac{1}{2\alpha^3}(4e^{-\alpha T_s} - 3 - e^{-2\alpha T_s} + 2\alpha T_s) \\
q_{23} &= \frac{1}{2\alpha^2}(e^{-2\alpha T_s} + 1 - 2e^{-\alpha T_s}) \\
q_{33} &= \frac{1}{2\alpha}(1 - e^{-2\alpha T_s})
\end{aligned}
\tag{5-34}
$$

In eq.(5-33), $\sigma_\alpha$is a conditional density modelled as a Rayleigh distribution variance of the acceleration for $a_{k+1}$and its equation is given by eq. (5-35)

$$
\sigma_\alpha^2 = \begin{cases} \frac{4-\pi}{\pi}(a_{max} - \hat{a}(t))^2, & \hat{a}(t) > 0 \\ \frac{4-\pi}{\pi}(-a_{min} - \hat{a}(t))^2, & \hat{a}(t) < 0 \end{cases} \tag{5-35}
$$

where $\hat{a}(t)$ is the current predicted acceleration and a_{max} and $a_{min}$are design parameters that correspond to the maximum and minimum accelerations respectively. In this equation, if the absolute values of the design parameters are small, the accuracy of the estimation will tend to be high, however, in cases where the changes of the relative motion are very aggressive, the filter will have a slow response. On the other hand, if the maximum and minimum values are larger, the model allows a quick response to the dynamics changes, but the tracking accuracy becomes lower. In this work, the helicopter can follow the mobile platform in a soft manner, so it has been preferred to model these acceleration parameters using a low profile and, in this way, to obtain more accurate estimations.

By generalizing the 1-dimension eq.(5-30), the equations of the model for three dimensions are given by

$$\mathbf{x}_{k+1} = \begin{pmatrix} \mathbf{F}_\alpha & \mathbf{0}_{3x3} & \mathbf{0}_{3x3} \\ \mathbf{0}_{3x3} & \mathbf{F}_\alpha & \mathbf{0}_{3x3} \\ \mathbf{0}_{3x3} & \mathbf{0}_{3x3} & \mathbf{F}_\alpha \end{pmatrix} + \begin{pmatrix} \mathbf{U}_\alpha & \mathbf{0}_{1x3} & \mathbf{0}_{1x3} \\ \mathbf{0}_{1x3} & \mathbf{U}_\alpha & \mathbf{0}_{1x3} \\ \mathbf{0}_{1x3} & \mathbf{0}_{1x3} & \mathbf{U}_\alpha \end{pmatrix} \tilde{\boldsymbol{a}}_k + \boldsymbol{w}_k \quad (5\text{-}36)$$

5.5. Fusion Filter block: Measurement model

Once the discrete-time dynamic equations have been modeled, the measurement equation of the discrete-time system is presented as

$$\boldsymbol{z}_k = \boldsymbol{H}_k \boldsymbol{x}_k + \boldsymbol{v}_k \quad (5\text{-}37)$$

where $\mathbf{z}_k$ is the measurement vector that contains the relative positions between the rotary-wing UAV and the landing point calculated using the relative system, $\mathbf{H}_k$ is the measurement matrix, and $\mathbf{v}_k$ is the noise in the measurements. In the relative estimator, a loosely couple scheme has been followed for both relative sensors, so the measurement matrix for the tether and radio-beacon based estimator is the same and is given by

$$\mathbf{H}_k = \begin{bmatrix} 1 & 0 & 0 & 0 & 0 & 0 & 0 & 0 & 0 \\ 0 & 0 & 0 & 1 & 0 & 0 & 0 & 0 & 0 \\ 0 & 0 & 0 & 0 & 0 & 0 & 1 & 0 & 0 \end{bmatrix} \quad (5\text{-}38)$$

Once the relative position vector has been computed from the sensors' outputs (this step is explained in section 5.1.1 and section 5.3), it can be used as the measurement vector $\boldsymbol{Z}_k$ of the eq.(5-37). Due to this vector has been calculated through rotations and translations in order to work in the navigation frame, the components of the measurement noise covariance become correlated. In order to calculate the terms of the covariance matrix, it is necessary to calculate the error propagation in a multi-input multi-output system. The measurement noise covariance matrix has the form:

$$\mathbf{R}_k = \begin{bmatrix} \sigma_{xx}^2 & \sigma_{xy}^2 & \sigma_{xz}^2 \\ \sigma_{xy}^2 & \sigma_{yy}^2 & \sigma_{yz}^2 \\ \sigma_{xz}^2 & \sigma_{yz}^2 & \sigma_{zz}^2 \end{bmatrix} \quad (5\text{-}39)$$

where the terms of the diagonal of the covariance matrix can be calculated as:

$$\sigma_{xx}^2 = \sum_i \left(\frac{\partial f}{\partial s_i}\right)^2 \sigma_i^2 + \sum\sum_{i\neq j} \left(\frac{\partial f}{\partial s_i}\right)\left(\frac{\partial f}{\partial s_j}\right)\sigma_{ij} \tag{5-40}$$

where f is the measurement function that is built with the sensors measurements (see section 5.1.1 and section 5.3), $\frac{\partial f}{\partial s_i}$ denotes the derivate of the function f with respect to the i^{th} sensor, σ_i^2 represents the variance of the i^{th} sensor and σ_{ij} is the covariance between the i^{th} and j^{th} sensors. In this case, the sensors are independent between them so the covariance σ_{ij} disappears and the resulting variance is

$$\sigma_{xx}^2 \sim \sum_i \left(\frac{\partial f}{\partial s_i}\right)^2 \sigma_i^2 \tag{5-41}$$

For the correlated terms of the covariance matrix, it is possible to calculate the terms solving the equation

$$\sigma_{xy}^2 = \sigma_{yx}^2 = \sum_i \left(\frac{\partial f}{\partial s_i}\right)\left(\frac{\partial g}{\partial s_j}\right)\sigma_i^2 + \sum\sum_{i\neq j} \left(\frac{\partial f}{\partial s_i}\right)\left(\frac{\partial g}{\partial s_j}\right)\sigma_{ij} \tag{5-42}$$

where the second term can be eliminated because the sensors are independent. Once solved the equations (5-41) and (5-42), the covariance matrix becomes extremely complex and it changes every time step, which involves a high computational cost because the functions that compound each term of the covariance matrix involve a lot of trigonometric operations.

After the preliminary experimental phases and through the processing of the real sensor data obtained during these flights, it was checked that this complexity was not necessary so, in order to reduce the computation cost of the algorithm and for having an easier to manipulate matrix, the noise covariance matrix was simplified and finally modeled as

$$\mathbf{R} = \begin{bmatrix} \sigma_h^2 & 0 & 0 \\ 0 & \sigma_h^2 & 0 \\ 0 & 0 & \sigma_v^2 \end{bmatrix} \tag{5-43}$$

where the values of σ_h^2 and σ_v^2 were given taking into account the accuracy of the relative measurements calculated during the laboratory tests.

Finally, for obtaining the solution of the estimation problem, it is used a linear Kalman filter (Falco et al., 2012), (Grewal, Lawrence and Angus, 2007) that makes use of the equations (5-30) and (5-37).). This filter has as output an accurate estimation of the relative state vector at 100 Hz, and it feeds the inputs of the autopilot 's control module.

5.6. Conclusions

In this chapter, the new T-GRANT and R-GRANT systems developed in this thesis are presented. These new navigators are used for the final approach of the UAV to the moving platform and also for the landing maneuver. Along this chapter, the different modules and elements that compound these navigators are explained.

Regarding the attitude calculation, in this thesis, it is developed a new algorithm called TWA-AHRS. This AHRS is based on an EKF and is able to change the measurement vector and the Kalman matrices in real-time depending on the acceleration module of the RUAV. After several comparisons with other AHRS and commercial systems, it is concluded that the new algorithm developed in this thesis improves the accuracy and is the most suitable for its use in our navigator modules.

Concerning the relative fusion filter, here it is developed a novel system model that takes as basis a Singer acceleration model and improves it by using some of the sensors onboard the helicopter. While the Singer model assumes that the acceleration is a zero-mean first-order stationary Markov process, in this thesis it is possible to use the UAV IMU measurements so that the relative acceleration vector is modeled to have an adaptive mean based on the accelerometers measurements.

Regarding the measurements, it is derived how to obtain the relative vector form both the tether device and the radio-beacon system. Due to the fusion filter is based on a Loosely coupled architecture, the measurement matrix can be created by using directly the calculations performed in the Conversion block of the navigator. Here it is also presented how to calculate the measurement noise covariance matrix of the Kalman Filter taking into account that the measurements are the result of several rotations and translations (the error becomes correlated). However, after a

processing phase of the data obtained from the first campaign of experiments, it is concluded that it is possible to use a simplified matrix where the value of the components are chosen from the analysis of the logged data.

6. EXPERIMENTAL RESULTS

6.1. EIRE Navigator Flight Tests

This section presents the experimental results related to the EIRE navigator tests. Real flights have been performed to obtain as much data as possible from multiple experiments to verify that the navigator systems based on EGNOS is able to improve the accuracy of those estimators whose positional solution is based only on the solution provided by the GPS constellation. In order to increase the variability of the data obtained, the tests campaigns were planned on two different dates and scenarios.

6.1.1. Configuration

The tests carried on along this work pursue the objective of testing if the accuracy of the positional solution calculated by the navigator is improved when the EGNOS capability of the GNSS receiver is enabled and used in the fusion algorithm. In order to obtain the necessary data for comparing the different configurations, three GNSS receivers were used and logged with the following configuration:

- Ublox receiver with EGNOS enabled.
- Ublox receiver with EGNOS disabled.
- AsteRx4 with raw measurements for Post Processing Kinematics (PPK) and PL calculation.

In order to quantify how EGNOS improves the navigational solution in a real environment, the estimations calculated using both Ublox sensors (same sensor with different configuration and sharing the same antenna) are compared with the PPK solution obtained from the AsteRx. The PPK solution has an accuracy of 1cm, so it has been taken as the true position of the experiments.

6.1.2. Scenarios and Flight Plans

The experimental flights were conducted during two different campaigns, each of them in a different scenario. The first flight zone was ATLAS [1] (Air Trafic Laboratory for Advanced unmanned Systems), a Test Flight Centre located in Villacarrillo (Jaen, Spain) which is equipped with technological-scientific facilities and airspace ideally suited to the development of experimental flights with unmanned aerial vehicles. The second campaign was carried out in a rural area of Kirkkonummi, located at 26 km from Helsinki. Figure 6-1 shows satellite images of the different flight zones.

(a) (b)

Figure 6-1: Test areas. (a)ATLAS Runway and (b) Kirkkonummi flight zone

For covering the largest possible casuistry within the data collection campaigns, the flight plans were created following different profiles (different locations, velocities, altitudes, etc). The flight procedures created are the following:

- **ATLAS FP1**: This flight procedure consists of a 6 km route with 12 waypoints. This procedure was conducted just one time because of its large length and the limited UAV operation time.
- **ATLAS FP2:** This procedure corresponds to a medium-size route of approximately 2 km, formed by four-segment legs deployed around the departing point. It aims to emulate a reduced version of the ATLAS FP1, allowing performing multiple flights without operation time limitations. This procedure was conducted 8 times at different velocities and altitudes.
- **FINLAND FP1:** This flight procedure corresponds to a short route of

approximately 300m, composed of five waypoints deployed at the north of the HOME point. It was carried out 5 times.

- **FINLAND FP2:** This flight procedure of 1075 m is formed by six waypoints. It was conducted 2 times.

These flights profiles are shown in Figure 6-2. In this picture, it is shown in orange the route commanded to the RPA with its different waypoints. Also, it is depicted in blue and grey the data recorded by the AsteRx4 and Ublox receivers respectively during one of the flights performed in these routes

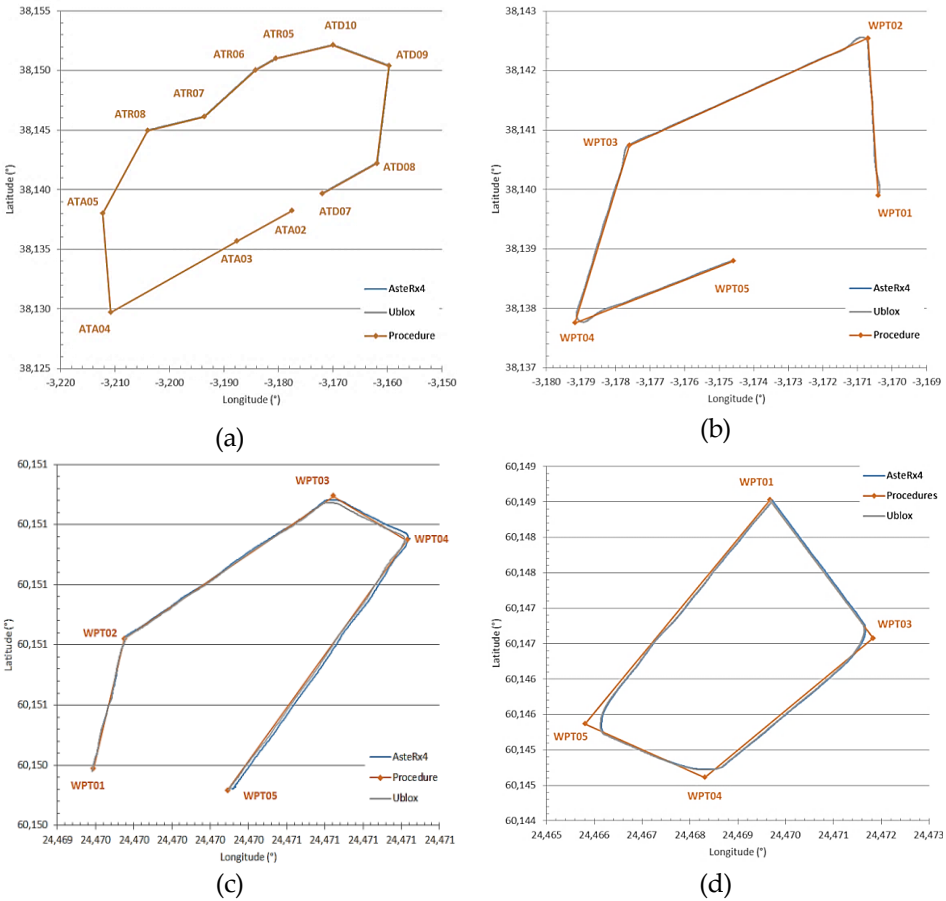

Figure 6-2: Flight plans created for data collection: (a) ATLAS FP1, (b) ATLAS FP2, (c) FINLAND FP1, (d) FINLAND FP2

6.1.3. Flight Data Analysis

This section presents an analysis of the flight data logged during the different campaigns of flights. Aiming to assess the benefits provided by EGNOS, two different navigation solutions have been computed in post-processing for comparison purposes:

- The first one has been calculated by using the EIRE navigator developed in this thesis and detailed in chapter 4. It uses the data logged with the ublox sensor that was configured for receiving the SBAS constellation, and also the protection levels calculated with the AsteRx4. In this chapter, this solution will be represented in black.
- The second solution is calculated with the same navigator scheme than the first one (based on a loosely coupled architecture), but in this case the estimation algorithm uses as its measurement vector the solution computed by the ublox receiver that was configured with the EGNOS constellation disabled. In this case, the Q and R matrices of the EKF are static with the values obtained by the preliminary tunning process (see section 4.5). This solution will be represented in red color through this chapter.

In order to assess which are the real differences between both solutions, the precise trajectory followed by the UAV has been computed in post-processing using the raw data measurements (pseudo-range, Doppler, carrier phase, phase lock and signal quality) logged by the AsteRx4 for generating a RINEX multi-GNSS observation file. This solution has been obtained through a post-processed kinematic (PPK) assessment, performed in differential processing mode using GPS, GLONASS and Galileo constellations when available. Two base stations and precise GNSS files were used for each trajectory processing. Solutions in forward & reverse directions were calculated and combined. This solution will be represented along this chapter using the color blue.

6.1.3.1. First campaign: ATLAS

To study the performance of the EIRE navigator developed during the first test campaign, one flight per route is analyzed in this section.

The first step for comparing the accuracy obtained with the different approaches is

to compare their calculated trajectories. Figure 6-3 presents the horizontal trajectories calculated in the navigational frame (North-East), where the origin is the take-off location.

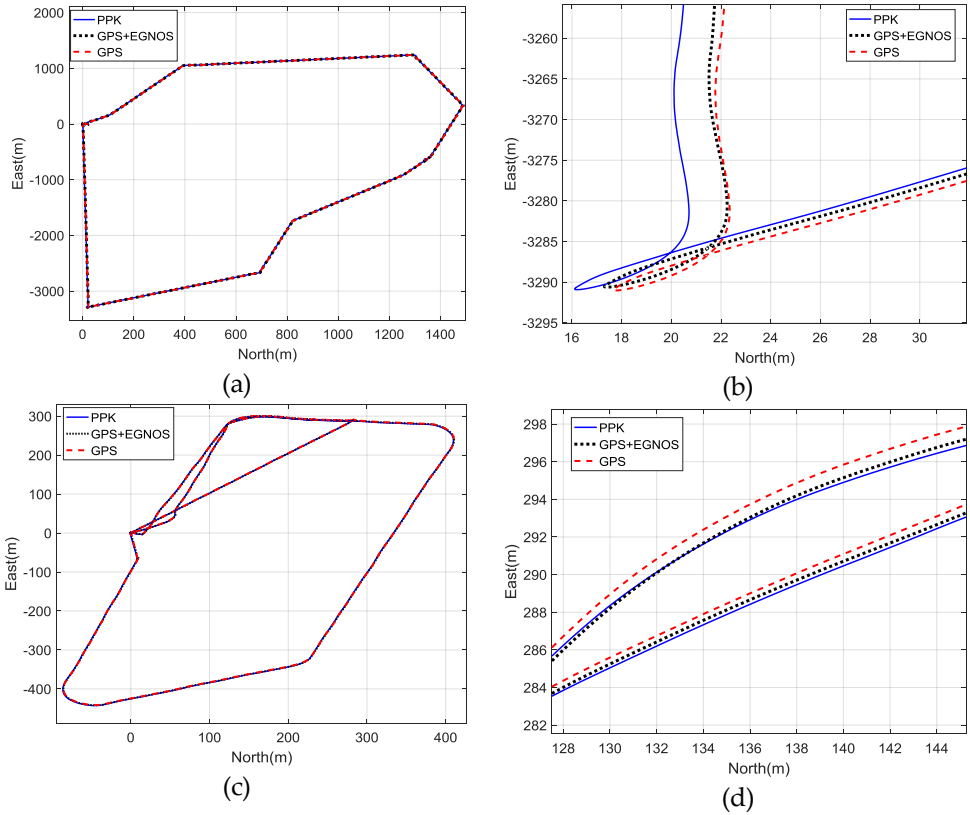

Figure 6-3: Comparison of the trajectories in North-East axes in the first campaign of flights. (a) ATLAS FP1 complete trajectory (b) Zoom of the ATLAS FP1 trajectory (c) ATLAS FP2 Complete trajectory, (d)) Zoom of the ATLAS FP2 trajectory.

As it is possible to see in (a) and (c), the lateral solution is very similar for both navigators, so that a zoom of a slice of the trajectory is presented in (b) and (d). In these pictures, it is shown how the EIRE algorithm (in black) follows the true trajectory more accurately than the solution based only in the GPS satellites (red line). To study this behavior over time, Figure 6-4 compares the North coordinates obtained from the different navigators.

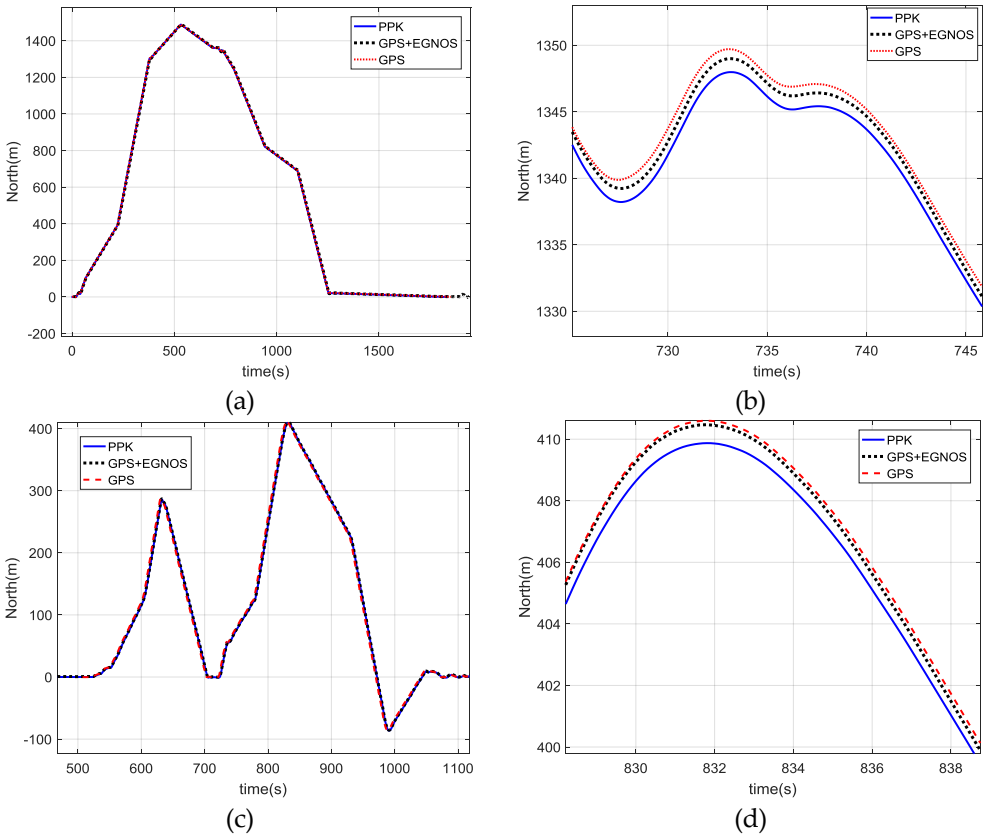

Figure 6-4 :Comparison of the North position over the time in the first campaign of flights. (a) ATLAS FP1 North position trajectory (b) Zoom of the ATLAS FP1 North position trajectory (c) ATLAS FP2 Complete North position trajectory, (d)) Zoom of the ATLAS FP2

In Figure 6-4,the zoom applied to (a) and (c) shows how the EIRE navigation solution is, in general, more accurate than the GPS one. Here, the convergence of the EIRE algorithm is faster, allowing to be closer to the real trajectory more quickly than the solution obtained with the GPS sensor. Through Figure 6-3 and Figure 6-4, it is demonstrated that the horizontal performance is improved using the EGNOS services in the estimation filter; however, this improvement is under one meter, so it is possible to say that both solutions will have a very similar performance in missions where it is not necessary to dispose of centimeter accuracy. Most relevant results can be found in the vertical axis. Figure 6-5 shows the altitudes over the

ground followed by the UAV during this flight campaign.

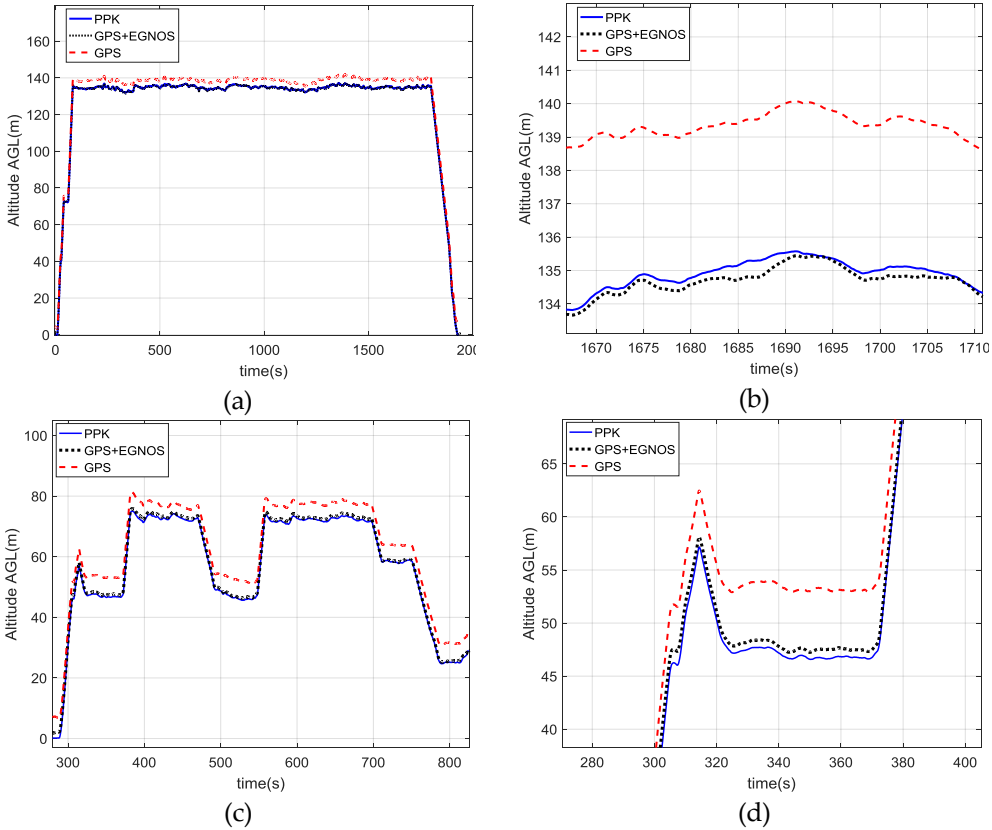

Figure 6-5:Comparison of the Altitude over the time in the first campaign of flights. (a) ATLAS FP1 Altitude position trajectory (b) Zoom of the ATLAS FP1 Altitude trajectory (c) ATLAS FP2 Complete Altitude trajectory, (d)) Zoom of the ATLAS FP2 Altitude trajectory

In the first route, all the waypoints were planned to have the same altitude while in the ATLAS FP2, the route was configured to have different altitudes, allowing to study the performance of the estimators when the dynamic in the Z axis changes. As it is shown in Figure 6-5, the solution provided by the GPS estimator has higher errors than the obtained using the EIRE architecture. In this case, this behavior can be also seen in the complete trajectories (a) and (c). In (b) and (d), it is shown how the new navigator is able of following the true

trajectory more accurately and with a time convergence faster than the architecture that only relies on the GPS positioning source. In that way, it is validated that it is possible to improve the altitude accuracy in some meters by using the new navigator. Figure 6-6 shows the errors over the time obtained from the different navigators when they are compared with the PPK solution.

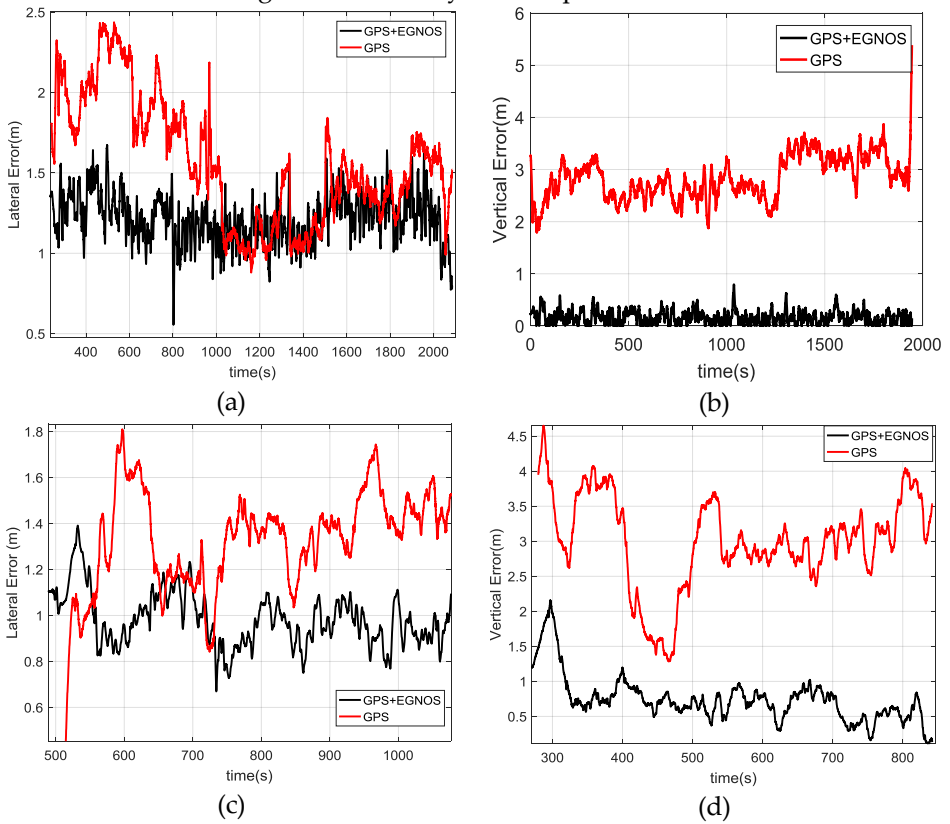

Figure 6-6: Errors obtained from the different navigation solutions during the first campaign of flights. (a) ATLAS FP1 horizontal errors (b) ATLAS FP1 vertical errors (c) ATLAS FP2 horizontal errors (d) ATLAS FP2 vertical errors

In Figure 6-6 it is possible to see that the new approach improves the solution in both horizontal and vertical axes. As it was presented previously, in the horizontal axis, the error committed by both estimators is very similar. It is in the vertical axis where the EIRE navigator improves the behavior of the estimation solution in some meters, allowing the UAV to have a better

knowledge of its real position. To quantify and compare the errors in both configurations, Table 6-1 and Table 6-2 shows some results of the accuracy obtained during these flights and some additional information as the velocity, protection levels and satellites used during these tests.

	Difference between EIRE navigator and PPK solution		Difference between EGNOS disabled navigator and PPK solution		RPA's Horizontal Speed (m/s)	Satellites Used
	Lateral	Vertical	Lateral	Vertical	Total	
Maximum	1,677	0,79	2,286	4,66	6,675	16
Minimum	0,554	0,002	0,355	1,9	0,024	14
Average	1,203	0,171	1,218	3,339	5,79	15,056
Percentile 95%	1,465	0,391	1,653	3,972	6,221	16

Table 6-1: ATLAS FP1 Errors obtained from the comparison of the PPK solution and the different navigator configurations, RPA's speed, protection levels and satellites used.

	Difference between EIRE navigator and PPK solution		Difference between EGNOS disabled navigator and PPK solution		RPA's Horizontal Speed (m/s)	Satellites Used
	Lateral	Vertical	Lateral	Vertical	Total	
Maximum	1,826	2,159	1,824	5,471	6,948	12
Minimum	0,665	0,001	0,425	0,001	3,347	10
Average	1,037	0,753	1,001	2,722	6,004	11,638
Percentile 95%	1,178	1,226	1,505	4,241	6,384	12

Table 6-2: ATLAS FP2 Errors obtained from the comparison of the PPK solution and the different navigator configurations, RPA's speed, protection levels and satellites used.

The diagrams and tables below aim to present the differences between the precise trajectory and the positioning solution computed by using the EIRE navigator and the GPS solution. As can be observed, lateral deviations from both solutions are similar on the average values; however, in EIRE solution, the dispersion is slightly lower, obtaining a small decrement in the 95th percentile. On the other side,

noticeable differences are obtained in the vertical axis, where the EIRE solution improves the error between 2m and 3m with respect to the GPS-based solution.

6.1.3.2. Second campaign: FINLAND

The second campaign of flights allowed collecting more real data under a different scenario, date and weather conditions. These changes have allowed analyzing the data obtained under different constellations geometries and with EGNOS receiving corrections from different base stations. In that way, it has been possible to check if the results obtained during the first campaign can be replicated under different test conditions. As it was done in the study of the first campaign, inFigure 6-7 and Figure 6-8 , the trajectories calculated by the different navigators are compared with the true solution obtained through the PPK algorithm.

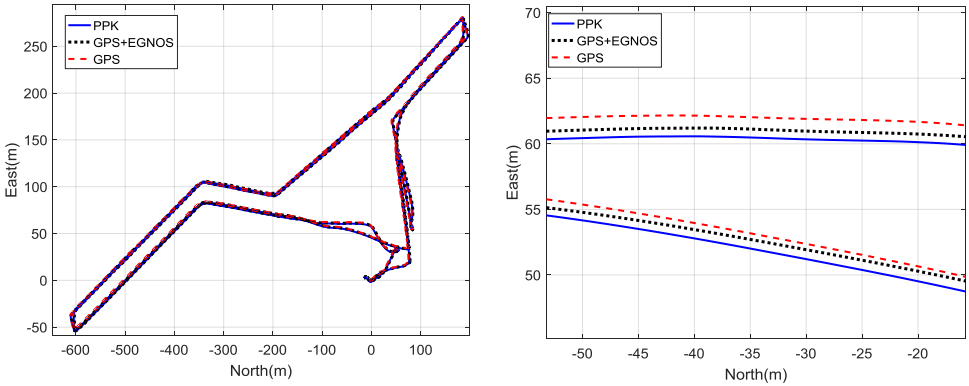

Figure 6-7: Comparison of the trajectories in North-East axes in the second campaign of flights. (a) FINLAND FP1 complete trajectory (b) Zoom of the FINLAND FP1 trajectory

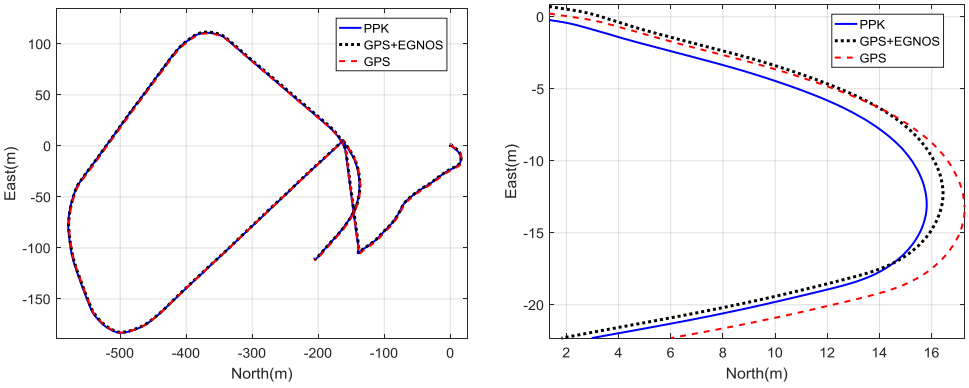

(a) (b)

Figure 6-8: Comparison of the trajectories in North-East axes in the second campaign of flights. (a) FINLAND FP2 Complete trajectory, (b) Zoom of the FINLAND FP2 trajectory.

In the flights presented in Figure 6-7 and Figure 6-8, the results obtained from the different fusion filters are again very similar in the horizontal plane, so it is necessary to make a zoom on both figures (a) to be able to appreciate the differences in the behavior of the estimations. Once the zoom is applied, (b) figures show how the EIRE navigator solution follows the true trajectory more accurately. However, it is important to note that the solution of the navigator that only relies on the GPS constellation also seems to have a good performance with errors under three meters. To study this behavior in a more detailed way, Figure 6-9 shows the North position over time in two of the flights performed during the second campaign.

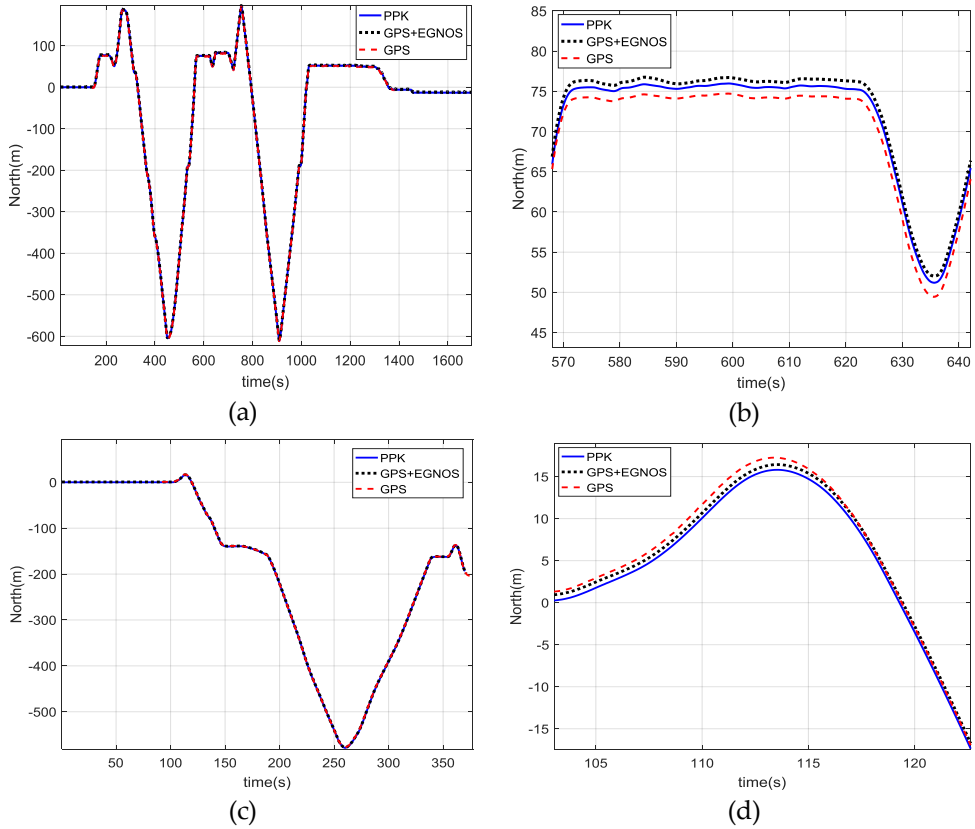

Figure 6-9: Comparison of the North position over time in the first campaign of flights. (a) FINLAND FP1 North position trajectory (b) Zoom of the FINLAND FP1 North position trajectory (c) FINLAND FP2 Complete North position trajectory, (d) Zoom of the FINLAND FP2

If a zoom is performed in (a) and (c), it is possible to check that effectively the EIRE solution has a lower error than the other configuration. Also, in (b) and (d) it is shown how in the straight sections of the trajectory, the new navigator use to be faster in its approach to the true position than the other solution. However, in these figures, it is again confirmed that both behaviors are quite similar. In order to see a more relevant improvement in the comparison of the new navigator with the GPS estimator, it will be necessary to study the vertical solution obtained during these tests. Figure 6-10 presents the results obtained in the vertical plane for both flight plans. While in (a) the waypoints of the flight plan had different altitudes, in the

second flight (c) the altitude was maintained at 60 m approximately during the whole operation.

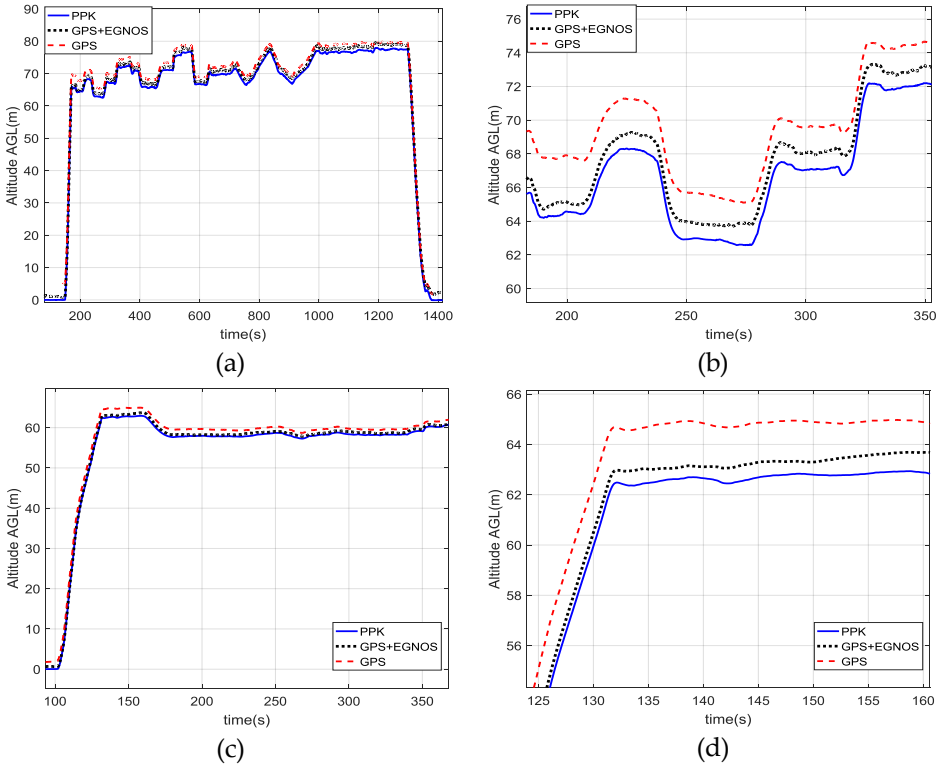

Figure 6-10: Comparison of the Altitude over the time in the first campaign of flights. (a) FINLAND FP1 Altitude position trajectory (b) Zoom of the FINLAND FP1 Altitude trajectory (c) FINLAND FP2 Complete Altitude trajectory, (d) Zoom of the FINLAND FP2 Altitude

As it happened in the first campaign, the altitude calculated by the estimator that does not make use of EGNOS in the fusion filter has an error of several meters. This error uses to have a constant part (like a bias) and another one that changes continuously along the time due to the corrections performed by the Extended Kalman Filter in the measurement phase of the filter. The EIRE navigator departs with a lower constant error due to the corrections that EGNOS provides to the GNSS filter. Also, the magnitude of the variating error is lower because the estimation filter is receiving more accurate corrections so it is able to converge to a

lower error quickly. Finally, Figure 6-11 shows the errors obtained in the lateral and vertical planes during two of the flights performed in this campaign

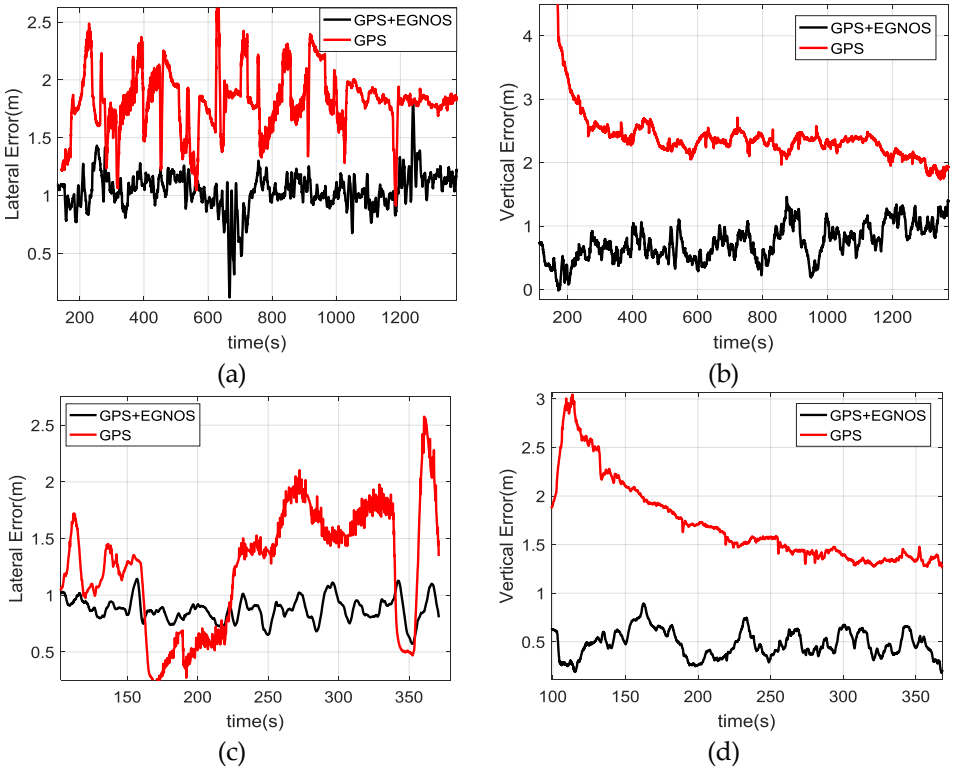

Figure 6-11: Errors obtained from the different navigation solutions during the first campaign of flights. (a) FINLAND FP1 lateral errors (b) FINLAND FP1 vertical errors (c) FINLAND FP2 lateral errors (d) FINLAND FP2 vertical errors

Through these graphs, it is easy to check how the performance obtained with the EIRE navigator allows improving the solution in both vertical and horizontal axes. As in the first campaign, the filter that only relies on the GPS has a larger constant error, which is more significant in the vertical axis. The dynamic behavior of the error has faster changes than in the solution obtained using the EIRE algorithm; this can be seen more quickly in the lateral error graphs (a) and (c).

Finally, Table 6-3 and Table 6-4 show the calculated errors during these flights.

	EIRE		GPS		RPA's Horizontal Speed (m/s)	Satellites Used
	H	V	H	V		
Maximum	1,43	1,32	2,57	4,88	8,725	7
Minimum	0,14	0,04	0,95	1,33	0,122	7
Average	1,12	0,66	1,83	2,61	5,204	7
Percentile 95%	1,27	1,15	2,47	3,03	8,231	7

Table 6-3: FINLAND FP1 Errors obtained from the comparison of the PPK solution and the different navigator configurations, RPA's speed, protection levels and satellites used.

	EIRE		GPS		RPA's Horizontal Speed (m/s)	Satellites Used
	H	V	H	V		
Maximum	1,23	0,96	2,56	3,06	8,725	7
Minimum	0,53	0,22	0,05	1,34	0,122	7
Average	0,75	0,53	1,47	1,74	5,204	7
Percentile 95%	1,16	0,71	1,93	2,28	8,231	7

Table 6-4: FINLAND FP2 Errors obtained from the comparison of the PPK solution and the different navigator configurations, RPA's speed, protection levels and satellites used.

As in the first campaign, numeric results demonstrate that the solutions are similar on the average error values of the horizontal axis. However, on the vertical axis, noticeable differences are obtained, and it is presented how the EIRE navigator improves the solution error approximately in 2m with respect the GPS-based navigator.

Through the more than 30 flights performed through both experimental campaigns, it has been demonstrated that the navigator developed in this thesis is able to improve the results obtained with those that only make use of the GPS constellation in their estimation algorithms.

6.2. R-GRANT Flight Tests

The real tests performed with the R-GRANT module have been focused on the approach and landing phases of the autonomous mission. The initial state of this scenario is the rotary-wing UAV flying autonomously with GNSS before the switch to relative coordinates navigation.

This section describes and analyzes the flight tests that were carried out to validate the developed navigation system. Using this technology, more than 25 successful autonomous landings have been performed. Below, telemetry results logged during the tests will be presented in order to illustrate the performance of the system. In (EC-SAFEMOBIL, n.d.), it is shown a video that summarizes the tests performed during the last campaign of flights.

6.2.1. Experimental Setup

The experimental setup is quite complex due to the interaction of many systems which were specifically designed for these tests. The complete setup is composed by:

- a ***moving platform:*** mounted on a trolley towed by a vehicle with a rope. The platform moves vertically by means of an elevator frame pushed by an electric engine (see section 3.2.4).
- a ***towing car***: which tows the trolley with a rope,
- a ***rotary-wing UAV***: with avionics equipment.
- ***RBS beacons***: Ground Station Units (namely GSU) which are placed on the moving platform with a certain pattern, which are used for the relative positioning (see section 3.2.2)
- ***Ground Control Centre*** which includes the Ground Control Station for the UAV and the Ground Control Unit of the platform, since the platform can be remotely controlled
- human resources for the complete operation.

Figure 6-12 shows the complete setup and actors during one of the landing tests performed in ATLAS.

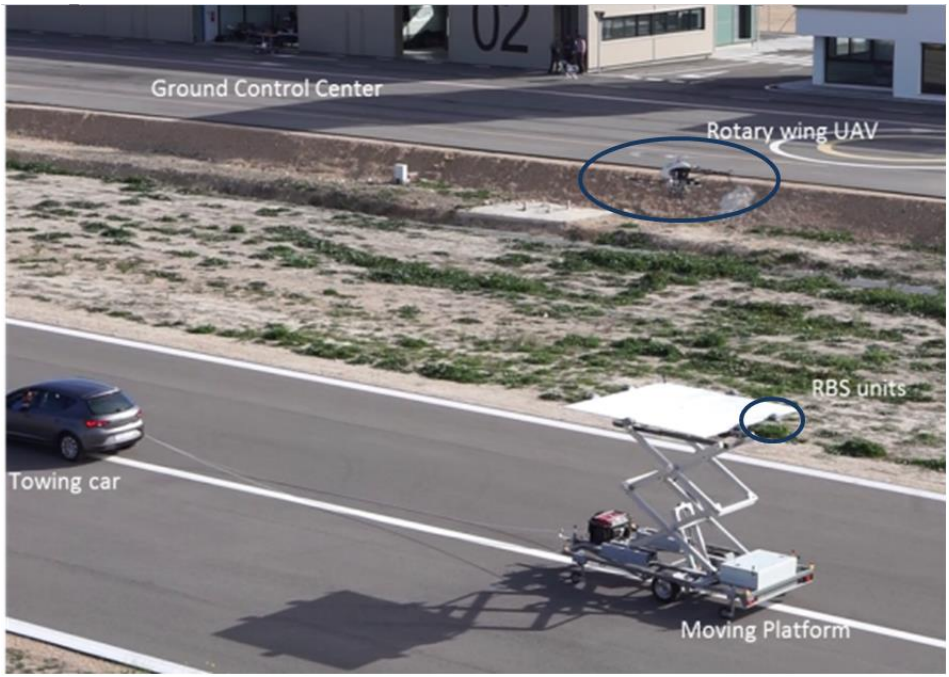

Figure 6-12: Complete experimental setup

As can be seen in Figure 6-12, the setup is quite complex, with lots of systems to be controlled and many interactions between them. Apart from that, there is an inherent risk in the operation which must be diminished. For that purpose, many safety mechanisms were designed in order to have safe operations.

The experimentation phase has been divided into several steps, increasing the difficulty in each step. These phases were based on the following stages:

- Approaches in manual flights: firstly, the ground antennas were placed on the ground and remained static. In this phase, experimental flights consisted of approaches in order to determine the RBS performance and coverage.
- Vertical landing with static platform: the GSUs were installed on the moving platform. This phase consisted of vertical landings of the rotary-wing UAV using relative coordinates. In this stage, the landing platform remained completely static.

- Landing with platform moving vertically: in this phase, the relative navigator is used to perform the approach and autonomous landing over the platform, which in this case is moving vertically.
- Landing with platform moving horizontally: landing of the rotary wing UAV on the platform which now moves horizontally (towed by a vehicle), using relative coordinates.
- Following the platform and landing combining all movements: tests in which the rotary-wing UAV follows the platform using relative coordinates and guided by RBS relative position data, and landing on the platform when it is moving both vertically and horizontally.

6.2.1.1. Rotary-wing UAV

The tests were performed with a rotary-wing unmanned helicopter based on the LOGO-800 RC helicopter. This UAV has a very good performance due to low level of vibrations in the airframe, large payload capacity (take-off weight of 15 Kg approximately), and high power to weight ratio which implies a very good dynamic response. The helicopter has a rotor diameter of 1.8 m and a main rotor speed of approximately 1400 rpm powered by a 4.8 kW electrical engine. These aspects make this UAV very suitable for the tests, which require powerful and agile maneuvers. However, it is important to notice that for safety reasons, this helicopter must not be flown with wind velocities over 25 km/h. In order to land in a more demanding scenario, it should be necessary to fly with another aerial platform.

The avionics equipment in the rotary-wing UAV includes an IMU for rates and accelerations measurements, a high precision radar altimeter for measuring relative altitude, a GNSS for the position and velocity calculation during the first phase of the flight and the RBS equipment. Due to the small size of the helicopter, a special structure was integrated in order to ensure the minimum distance between the two airborne antennas for the right performance of the system. Figure 6-13 shows the aforementioned equipment in the unmanned helicopter.

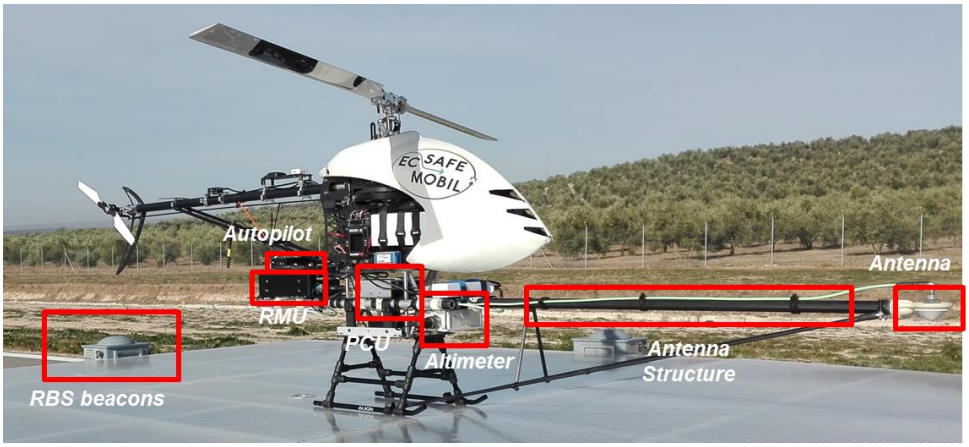

Figure 6-13: Integration of main RBS equipment in the helicopter research platform

The integration of the RBS sensor in this kind of helicopter is quite complex, being necessary an in-depth study of structure performance. Some problems arose at the beginning of the experimentation regarding ground resonance, a typical effect which appears in many helicopters. So it was decided to perform additional modifications in the structure where the antennas and the avionics equipment were installed. However, during the flight campaigns, it was not possible to obtain the heading measurements from the RBS sensor by using the multi-antenna approach. Therefore, the tests were carried out without having measurements of the relative heading between the landing platform and the UAV. In those tests where the platform remained static or it was moved following a straight line, this information was introduced manually in the autopilot by knowing the real orientation of the RBS beacon structure and the landing runway.

6.2.2. Description and analysis of the experiments

This section describes and analyzes the tests related to the RBS system performed through this thesis. Results will show that the navigation technique developed is reliable enough for the guidance of an unmanned rotary-wing UAV when it is approaching to a moving platform. Here, it is also demonstrated that the R-GRANT estimator allows autonomous landing maneuvers in some specific scenarios.

6.2.2.1. Sequence of steps

The complete experiment comprises both the approach and the landing of the rotary-wing UAV to the moving platform. The following lines explain the sequence of steps followed during the operations:

- ***Initial condition***: the rotary-wing UAV flies autonomously with the global navigator inside the RBS coverage.
- ***Step 1:*** check that the UAV is inside the RBS area, so the relative positioning solution is valid and consistent. Guide the rotary-wing UAV in relative coordinates so that it goes over the landing platform, always inside the RBS area.
- ***Step 2***: when the rotary-wing UAV is located over the platform, the altimeter starts to control the height AGL (in this case above platform level). When activating the altimeter, the relative height to the platform is maintained.
- ***Step 3***: command a horizontal displacement in relative coordinates to the origin of the platform (0,0). In this phase, the relative height commanded over the platform is maintained, so if the landing platform is in movement, the helicopter must follow the platform maintaining the relative horizontal position and height.
- ***Step 4***: once the rotary-wing UAV is above the origin, the descent to the landing platform is commanded, with a certain velocity, until the helicopter touches down.

6.2.2.2. Approaches in manual flights

In this stage, flights were carried out manually. They consisted of multiples approaches to the landing platform at different angles and heights in order to study the performance of the RBS and the estimator at different distances from the landing platform where the GSUs were installed. In these operations, the landing platform remained completely static. In order to be able of obtaining the accuracy of the solution calculated with the developed navigation system, the position calculated with the relative estimator will be compared with the data collected from the GPS RTK sensor installed in the setup.

One of the main objectives of these flights was to test the operational distance

under the RBS works correctly and is able of providing an accurate enough solution for the approaching and landing procedures. Figure 6-14 shows the distance from the helicopter to the landing platform (LP) and the quality status of the RBS system during one of these tests.

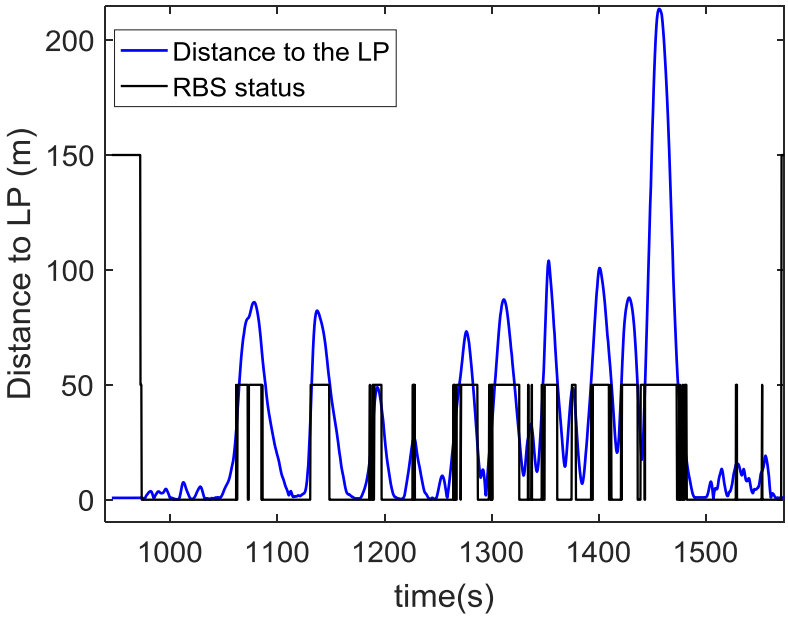

Figure 6-14: Distance to the landing platform and RBS status during the manual flight experiment.

The RBS quality status is a signal that indicates the quality in the solution of the radio-beacon sensor. When this signal is equal to 0, it indicates that the solution quality is the best than the sensor can provide. If its value is 50, the radio-beacon system does not assure to provide an accurate solution. In other cases, the solution is degraded and it is not recommended its use. As it is possible to see in Figure 6-14, the status of the sensor uses to change its value when the distance to the platform is larger than 50 meters approximately. In Figure 6-15, it has been zoomed the flight graph in two approach maneuvers. In this picture, it has been marked with a red cross the points in which the sensor switches to another state.

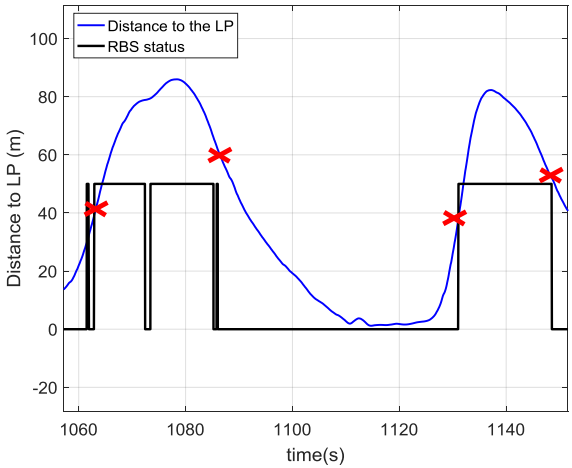

Figure 6-15: RBS status changes with the distance.

In order to study the effect of the RBS status in the accuracy solution of the navigator estimation, Figure 6-16 presents the position North (a) and altitude (b) calculated by the navigator in some of the slots of time in which the RBS switches its quality signal. In this case, the navigator has used the RBS sensor in both horizontal and vertical axes (altimeter was not used).

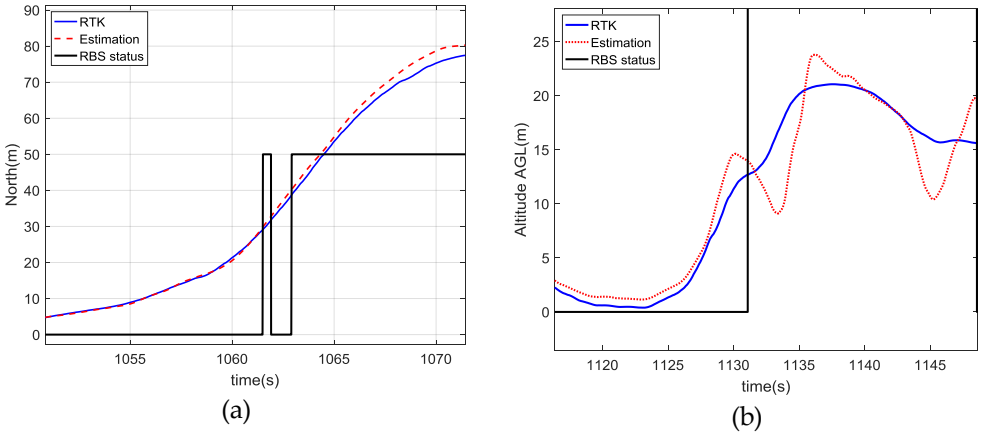

Figure 6-16: Effect of the sensor status in the accuracy of the positioning solution of the navigator in the (a) North axis and (b) altitude.

As it is possible to check in Figure 6-16, the error grows up when the helicopter gets away from the landing platform (where the GSUs are installed). This error is more

appreciable in the altitude, where the behavior of the solution does not follow the real trajectory.

Figure 6-17 shows another manual flight with several approaches to the landing platform where the RPA flew at a distance lower than 30m from the radio beacon infrastructure on ground and the RBS quality signal was the best possible during the whole maneuver. In this case, the R-GRANT estimation solution is more accurate and there are not important deviations from the RTK solution, being the error in the horizontal axes under 1 m.

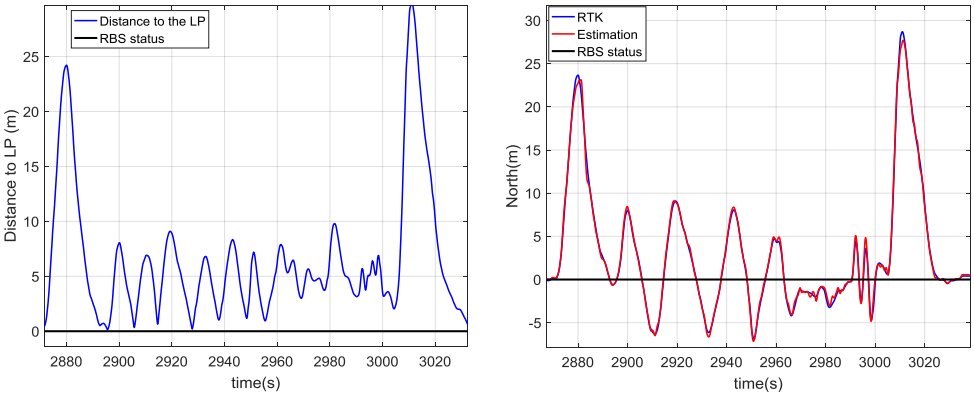

(a) (b)

Figure 6-17: Manual approaches with distances to the LP shorter than 30m.

In order to quantify the error of the estimator at different distances from the landing platform, Table 6-5 summarizes the results of this first campaign of flights.

		Distance to the landing point			
		< 15 m	**<30 m**	**< 60 m**	**> 60 m**
RMS	**North**	0.1945	0.6948	0.9888	2.2287
	East	0.2562	0.5842	1.1647	2.2161
	Altitude	0.8724	1.4605	3.0370	7.0861
STD	**North**	0.3071	0.7249	1.2254	3.3620
	East	0.4407	1.0008	1.5722	3.4795
	Altitude	0.4793	1.8442	3.9172	9.5538

Table 6-5: Accuracy of the navigational solution regarding the distance to the platform

From these results several considerations were taken into account for the following tests:

- Horizontal accuracy is enough for the approach phase of the RPA to the landing platform once it is at a distance lower than 60 m. From the results obtained in the different flights, it is possible to conclude that this solution could be used for performing the approach phase without problems; even it could be possible to carry out the autonomous landing maneuver if the landing platform is not under movement. However, for performing this last step, it is advisable to improve the accuracy of the final solution. In order to do this, the data logged during these tests was used for tunning the filter's parameters and improving the overall performance of the autopilot.
- The altitude accuracy provided by the RBS system is not enough for performing the landing maneuver or the tracking procedure safely. Due to the variations in this variable, it was decided to use the altimeter installed in the RPA as the main sensor used by the navigator for calculating the relative altitude to the landing point.

6.2.2.3. Autonomous Landing with the platform static in the horizontal plane

From the results obtained in the previous step, the estimator was tunned and it was possible to create a guidance strategy based on the distances of the helicopter to the landing platform. Tests presented in this section consist of performing autonomous landing procedures by using the radio-beacon sensor as the position source of the navigation algorithm and feeding the controller with the outputs of the relative estimator. In this scenario, the landing platform remains static during the whole operation in the horizontal plane. Regarding the vertical plane, first landings were performed with the platform also static. However, once it was checked that the helicopter was able to land correctly without human intervention, the platform was commanded to move in the vertical axis.

Figure 6-18 shows the comparison between the position and velocity solutions of the R-GRANT module and the RTK sensor in the horizontal plane during a landing with the platform completely static. At the beginning of this test, the helicopter is at 14 meters from the landing point. At time 870s, the approach is commanded and, once the RPA is over the platform at 935s, the descent starts.

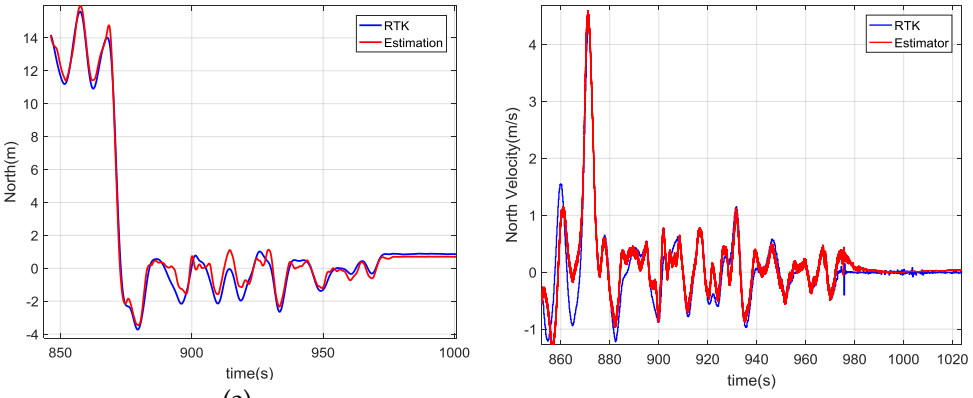

Figure 6-18: horizontal position and velocity during an autonomous landing with the platform static in both axes.

These pictures show how the horizontal position and velocity calculated with the estimator are very similar to the solution obtained with the RTK sensor. The accuracy uses to be under one meter. However, there are some slots of time (for example from 900 to 950) where the RBS sensor fails and the accuracy of the estimator gets worst. Due to this behavior depends only on the RBS sensor, it is not advisable to perform the landing maneuver in scenarios with complex conditions like could be a landing procedure over a ship with strong sea dynamic.

In these tests, the altitude measurement used by the estimator is the provided one by the altimeter. In Figure 6-19, it is shown as the vertical position and velocity solutions of the navigator have good accuracy and follow the measurements provided by the RTK sensor. In this graph, the difference between the estimator and the RTK sensor flight at the beginning of the flight is due to, at this time, the RPA was not flying over the platform, so the altimeter was measuring the distance to the ground and not to the landing platform. Once the RPA is on the top of this platform (at 870 s approximately), the altimeter is able to measure the distance directly to the landing point (in this case the platform was elevated approximately 2 meters AGL).

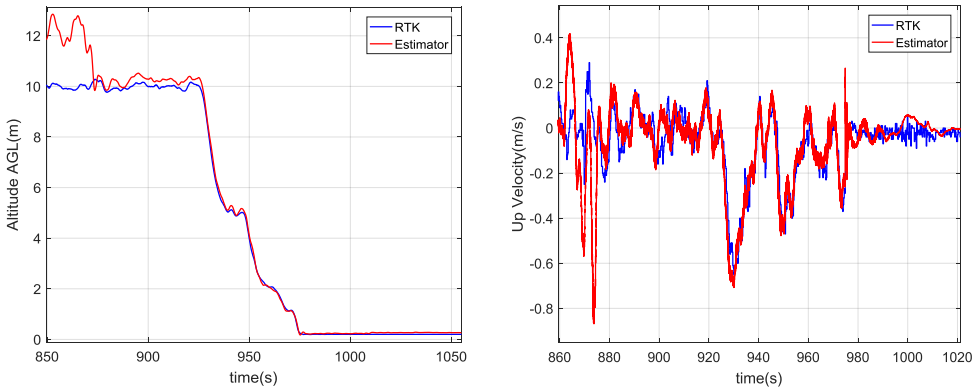

Figure 6-19: Altitude during an autonomous landing with the platform static in both axes.

Once several landings were performed successfully, it was started a new phase where the landing platform was commanded to move in its vertical axis. During these tests, it was checked that the accuracy of the R-GRANT module had not variations with respect to the scenario in which the landing platform remained completely static. It means that the vertical movements do not substantially affect the calculations that the RBS sensor performs in the horizontal plane. Figure 6-20 shows an interval of time of one flight where the moving platform is oscillating in the vertical axis and the UAV has been commanded to maintain the relative vertical altitude over the landing point.

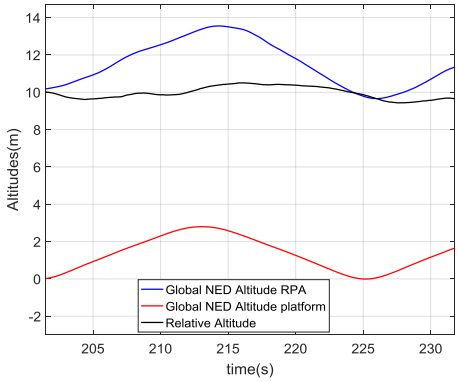

Figure 6-20: RPA maintaining the relative altitude to the landing platform which is in movement in the vertical axis

Table 6-6 presents the RMS errors and the standard deviation of the navigator solution in both position and velocity. As it is possible to see, the error in the horizontal plane is less than 0.7 meters. Although this accuracy is better than the obtained with a typical GNSS sensor, it would be advisable to improve it in order to be able of performing the final maneuver in any platform and scenario safely. The performance in the vertical axis is very good, obtaining an accuracy of 10 cm approximately.

	Position			Velocity		
	North	**East**	**Altitude**	**North**	**East**	**Up**
RMS	0.4182	0.3945	0.1098	0.4287	0.5338	0.0512
STD	0.7273	0.4524	0.2522	0.7535	0.8152	0.0681

Table 6-6: Navigator accuracy in the autonomous tests experiments with the platform static in the vertical plane

6.2.2.4. Landing with horizontal displacement

In this phase of the tests, both guidance and navigation filters were tested over operations where the unmanned helicopter was commanded to land on the landing platform when it was moving horizontally and vertically. Figure 6-21 shows the trajectory in Google Earth of both the helicopter and the moving platform during the operation.

Figure 6-21: Rotary wing UAV trajectory (blue) landing on the moving platform (red)

Figure 6-22 shows the relative vertical position, the platform local altitude and the platform North position during a complete test. These experiments were composed of two different phases: static and dynamic. At the beginning of the first phase, the landing platform is static in the horizontal plane. Once all the systems are ready and the UAV has taken off (t=370s), the GCS commands the vertical movement to the driver of the platform and it begins to oscillate in the vertical axis (t=435 s). Once the helicopter is in the air and the landing platform oscillating, the second phase starts. In this phase, the landing platform begins its movement also in the horizontal plane (t=538 s) until the helicopter lands (t=610).

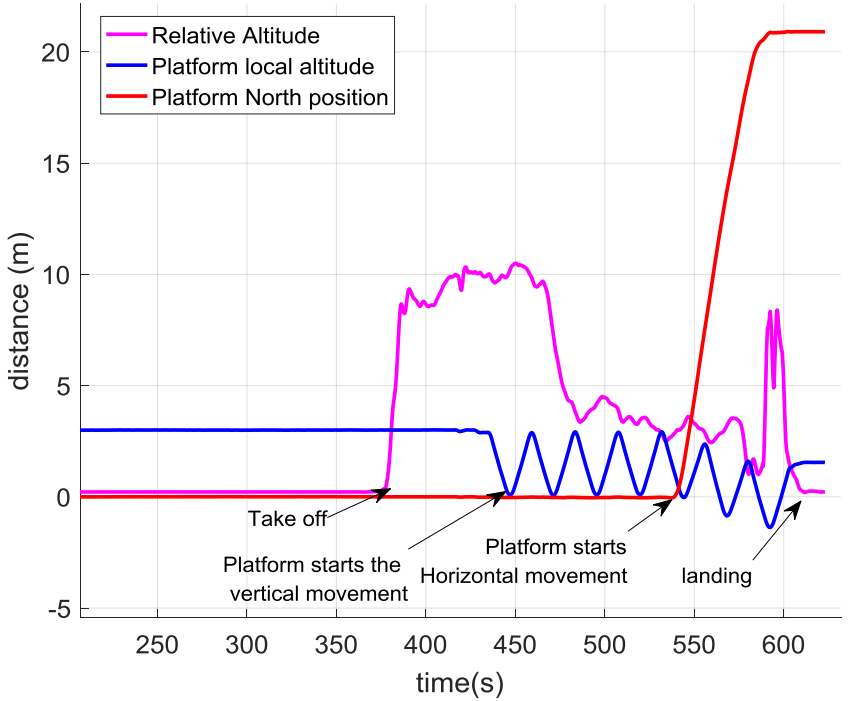

Figure 6-22: UAV Relative vertical position, platform altitude and North position during the straight movement test using the Radio-beacon based navigator and different phases of the operation

In order to study the estimation accuracy achieved during these tests, Figure 6-23 shows a comparison between the relative position calculated with the GNSS-RTK system (used again as ground-truth) and the relative position solution obtained with the radio-beacon based navigator.

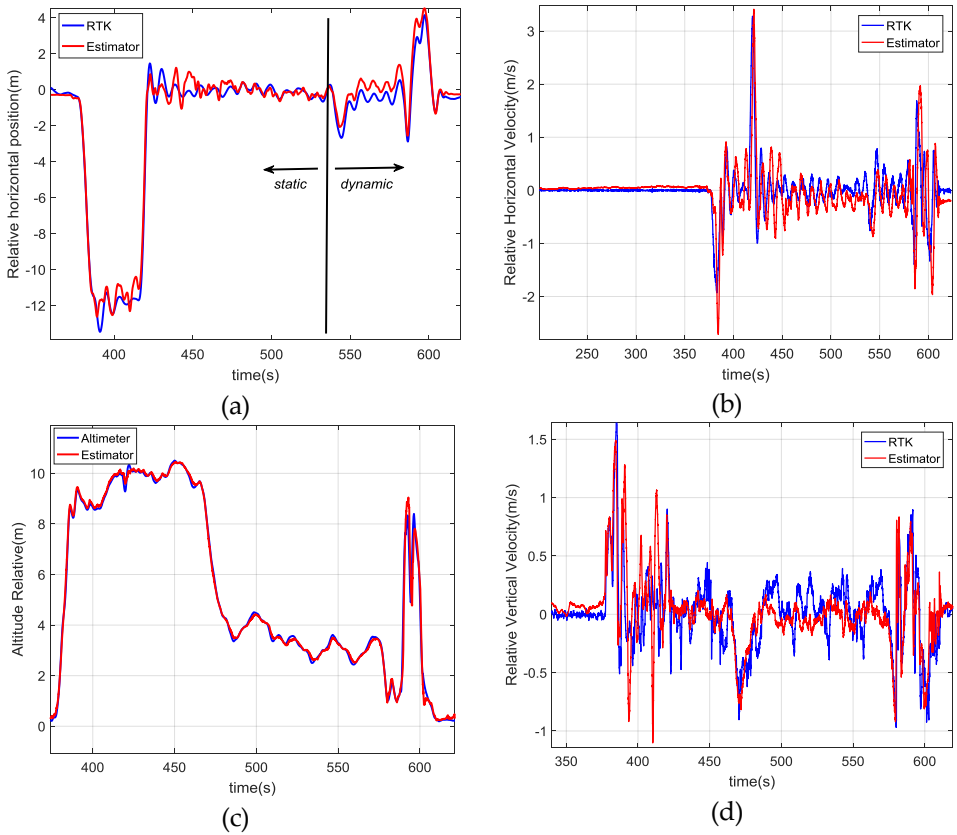

Figure 6-23: Comparison among the R-GRANT solution (red) and the GNSS-RTK measurements (blue) during a test where the landing platform is moving following a straight trajectory: (a) position in the horizontal plane, (b) velocity in the horizontal plane, (c) relative altitude, and (d) relative vertical velocity.

Figure 6-23 shows how in the dynamic phase of the operation, when the landing platform starts the horizontal movement, the error in the position estimation grows. This error appears if the helicopter does not have information about the landing platform orientation. In those cases, when the RBS measurements (in the body frame of the landing platform) are converted to the navigation frame, the relative heading error is translated to errors in the relative position and velocity estimated in the horizontal plane. The magnitude of these errors depends on the relative orientation error and the distance to the platform. In this experimental phase, the platform was moved following a straight line parallel to the ATLAS

runway, so this error was minimized and was approximately constant. As a consequence, the mean error was under 1.3 m, allowing the RPA to land safely in the landing platform. Table 6-7 presents the computed errors for the static and moving stages of the operation.

		Position			Velocity		
Platform	**Accuracy**	**X North**	**Y West**	**Altitude**	**X North**	**Y West**	**Vertical**
Static	**RMS error**	0.341	0.452	0.112	0.343	0.249	0.051
	STD	0.551	0.779	0.034	0.451	0.340	0.057
Moving	**RMS error**	0.652	0.882	0.172	0.402	0.442	0.098
	STD	0.961	1.197	0.210	0.621	0.632	0.211

Table 6-7: RMS error and Standard Deviation of the position (m) and velocity estimation solution (m/s) during a landing over a platform that is following a straight trajectory. Calculations have been performed using the RTK-GNSS system as ground truth.

From the results presented in this table, it can be seen that the performance of the R-GRANT filter gets worst during the movements of the landing platform having a horizontal error of about 1 meter in position and 0.55m/s in velocity. These errors could be reduced to have the same accuracy than in the static case if the orientation information of the mobile platform were calculated. In Figure 6-24, it is presented the descent phase of the landing maneuver. As it is possible to check in (a) and (b), the descent starts at t=597, and the helicopter gets closer to the platform (c). Regarding the vertical velocity, it decreases slowly from 1 m/s when the platform is at 9 m, to 0.2 m/s when the RPA is over the landing point and the altitude is approximately 2 meters. In this way, the descent is safely controlled by reducing the velocity in the final phase of the landing and making the helicopter to move softer.

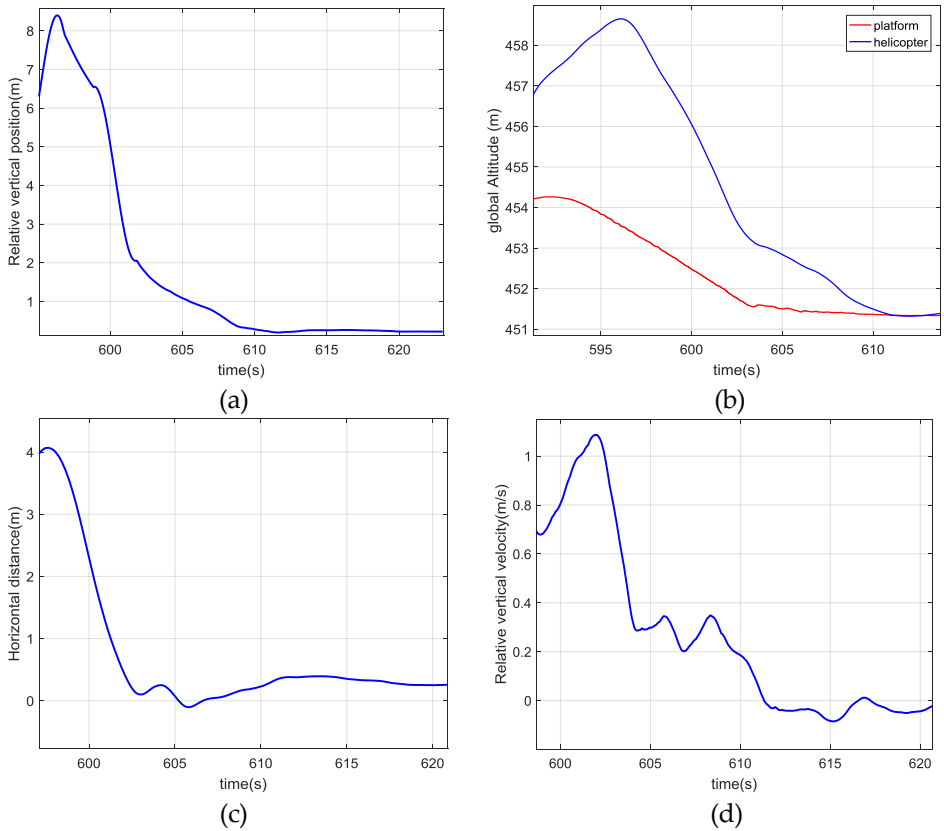

Figure 6-24: Helicopter descent phase in the straight movement test: (a) shows the altimeter measurements of the relative altitude, (b) compares the AGL of the RUAV and the moving platform, (c) shows the horizontal distance between the helicopter and the landing point, and (d) represents the vertical velocity during the descent.

In this phase, the UAV was able to track the platform in all the flights; in fact, the radio-beacon sensor has proven to be a very good option for performing this task. Taking into account that the accuracy calculated during the experiments and presented in the Table 6-7 is around 1 meter, the final landing was possible in the 70% of the cases, which is a good percentage if it is taken into account that the navigator did not have access to the landing platform orientation during the experiments. In Figure 6-25 it is shown the UAV at the moment in which it is landing over the mobile platform.

Figure 6-25: RPA with radio-beacon based navigator performing a landing.

6.2.2.5. Non-straight maneuver

In this scenario, the car towes the trolley along curvilinear paths (see Figure 6-26). The goal of this phase is to test the performance of the R-GRANT module in those cases where the trajectory of the landing platform is not entirely straight and it is performing more complex maneuvers.

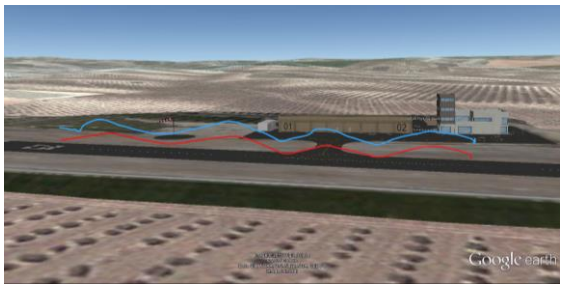

Figure 6-26: Curvilinear trajectories. Blue line: helicopter. Red Line: moving platform.

The procedure for the operation is the same as in the previous cases, but with the difference of the curvilinear path of the car. As can be seen in Figure 6-27, in the vertical axis, the performance is quite similar to the obtained in the straight movement scenario. As the previous flights, the relative height is quite well maintained using the altimeter (see (a)). In (b), it is shown how the platform oscillates around a line which has a certain positive slope, meaning that the platform is climbing a little bit. This effect is due to the slope of the runway. Regarding the relative positioning, in (c) can be seen as the rotary-wing UAV maintains its flight over the vertical of the landing platform quite well, being able of

following the vehicle at a distance lower than 2 meters during the whole operation. In (d) it is shown the groundspeed of the landing, which was approximately constant with a mean of around 5 km/h.

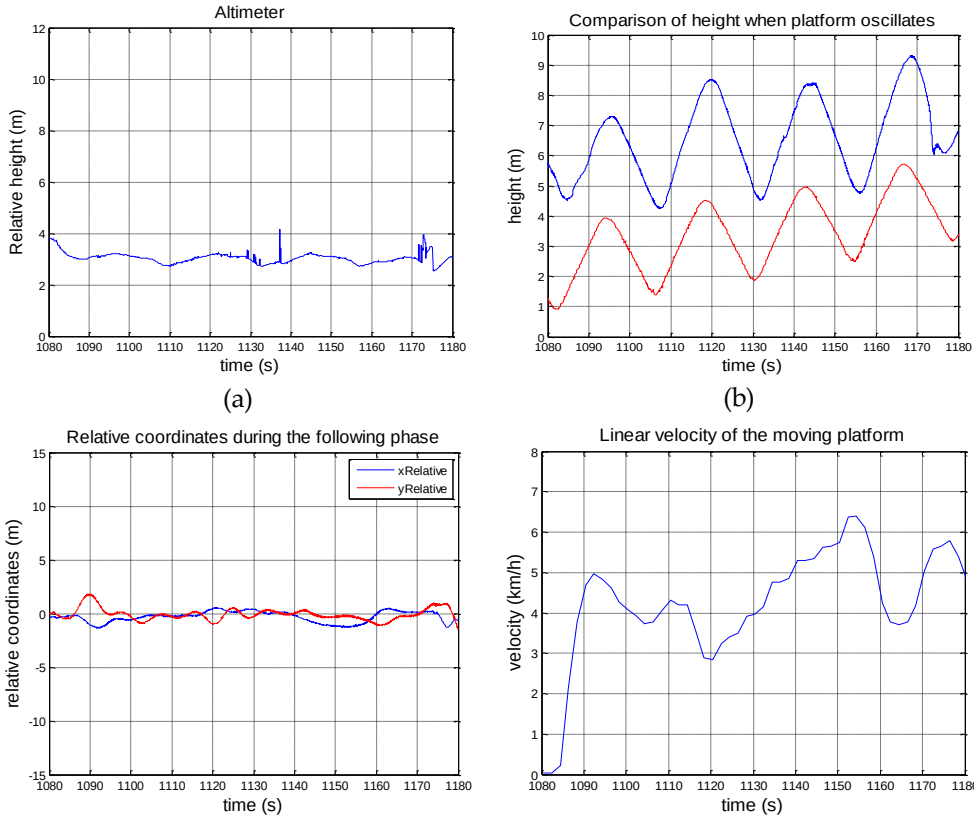

Figure 6-27: Landing manoeuver data regarding curvilinear paths using the R_GRANT module: (a) Relative altitude measured by the altimeter, (b) comparison between the AGL of the RUAV and the moving platform, (c) relative distance in the horizontal plane between the helicopter and the landing point, and (d) linear velocity of the moving platform during the test.

Figure 6-28shows the trajectory in a XY graph with some time marks. From the linear velocity of the moving platform that was shown in Figure 6-27, it can be seen that the trolley starts moving at *t=1080s* approximately

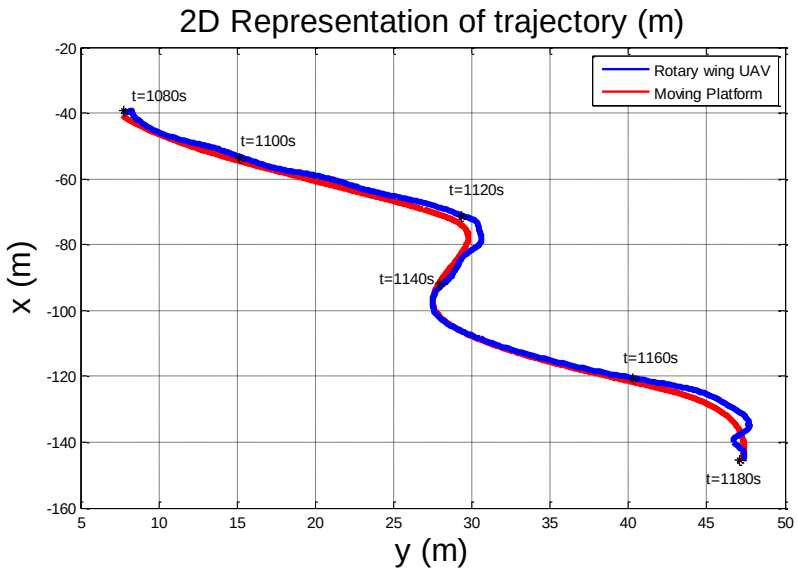

Figure 6-28: XY representation of trajectory in time

In this case, the test also has a static and a moving phase. Figure 6-29 shows the comparison between the radio-beacon based relative estimator and the RTK solution. As can be seen in (c) and (d), both position and velocities estimations in the vertical plane are very accurate and follow the dynamics of the real relative vector. However, as it is shown in (a) and (b), the accuracy in the horizontal plane when the platform starts moving is worse than in the previous tests. The increase in the error during these operations is due to the lack of knowledge of the orientation of the landing platform. When the ground vehicle is turning, the heading changes, so the conversion of the RBS sensor coordinates to the navigational axes adds an error that is proportional to the distance to the platform and to the difference between the helicopter and the landing platform heading. For this reason, for this type of movements, if the RBS is the chosen sensor to land, it will be crucial that the navigator can access to the landing platform orientation information.

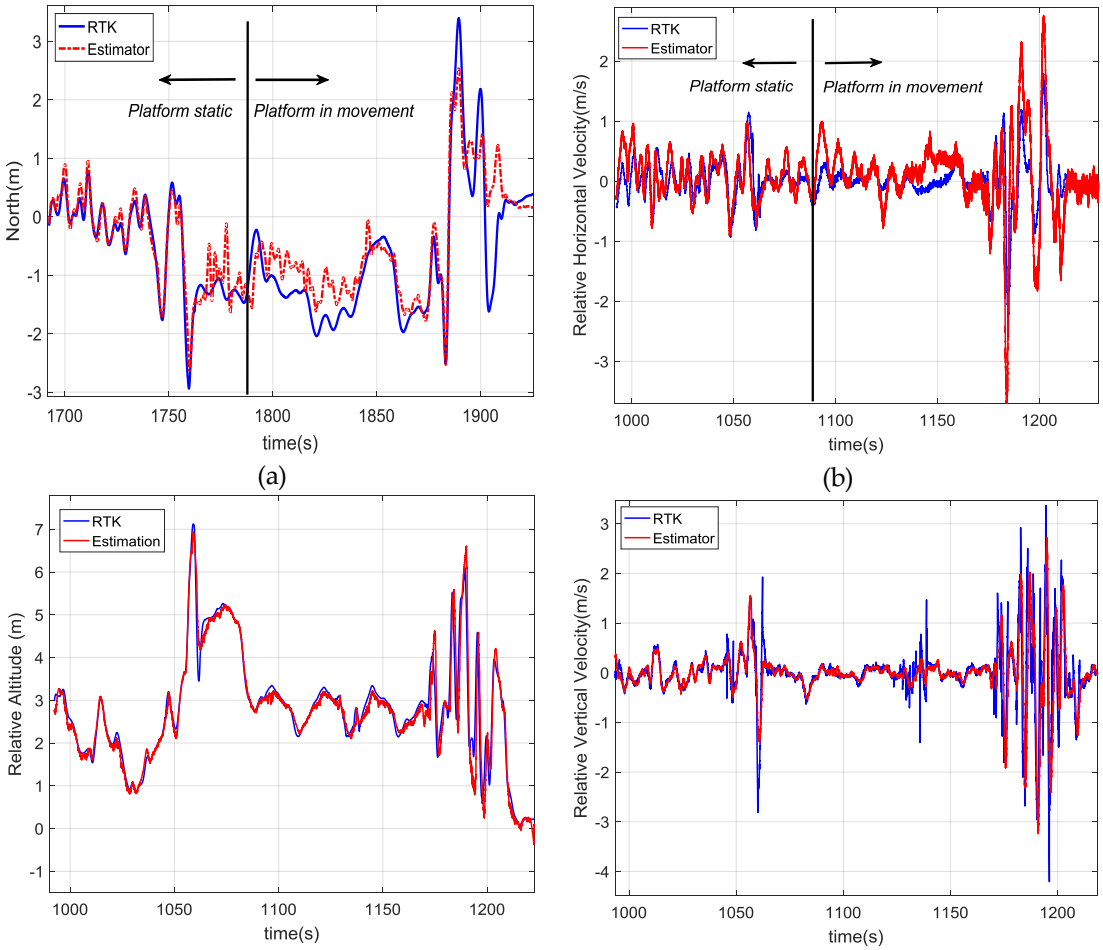

Figure 6-29: Comparison among the R-GRANT solution (red) and the GNSS-RTK system (blue) during a test where the landing platform is moving following a curvilinear trajectory: (a) measurements of the position in the horizontal plane, (b) relative velocity in the horizontal plane, (c) relative altitude and (d) relative vertical velocity.

Table 6-8 shows the calculated errors during the static and dynamic phases of this test.

		Position			Velocity		
Platform	**Accuracy**	**X North**	**Y West**	**Altitude**	**X North**	**Y West**	**Vertical**
Static	**RMS error**	0.302	0.361	0.092	0.257	0.322	0.103
	STD	0.451	0.579	0.104	0.483	0.513	0.109
Moving	**RMS error**	1.452	1.182	0.212	0.602	0.723	0.178
	STD	1.725	1.467	0.301	0.861	1.102	0.241

Table 6-8: RMS error and Standard Deviation of the position (m) and velocity estimation (m/s) solution of the radio-beacon based sensor during a landing over a platform that is following a curvilinear trajectory. Calculations have been performed using the RTK-GNS

As it is possible to see in the Table 6-8, the mean error in the moving phase of this test is around 2 m. This error depends on the relative orientation error and the distance to the platform. Although in the majority of these tests was possible to land, this maneuver has some risks and is not advisable to perform an autonomous landing for safety reasons. From the data obtained in these flights, it can be concluded that for this kind of maneuvers, if it is intended to perform an autonomous landing, it will need to know the real orientation of the RBS sensor or, if this is not possible, to perform this last maneuver using another method, for example by using the rope device presented in this thesis. However, also it is possible to conclude that the R-GRANT module has been proved to be valid to follow the mobile platforms during the approach procedure.

6.3. T-GRANT Flight Tests

The real tests with the tether device have been focused on the landing phase of the mission. Hence, the initial state of the system is the rotary-wing UAV flying autonomously with GNSS and the tether locked in the platform ready to be stretched before the switch to relative coordinates navigation.

The key of the operation is to have the tether taut when navigating with relative coordinates so that the tether accurately represents the straight line which connects

the helicopter and the origin of the platform from which the tether is pulled. If the tether is not tense, the cardan angles data will not be representative of the direction vector of the straight line which connects the helicopter and platform, so the relative position estimation is wrong. Figure 6-30 shows the tension and switching signals logged during one test. As can be seen, only when the tension of the tether is at its maximum value, the relative mode turns on.

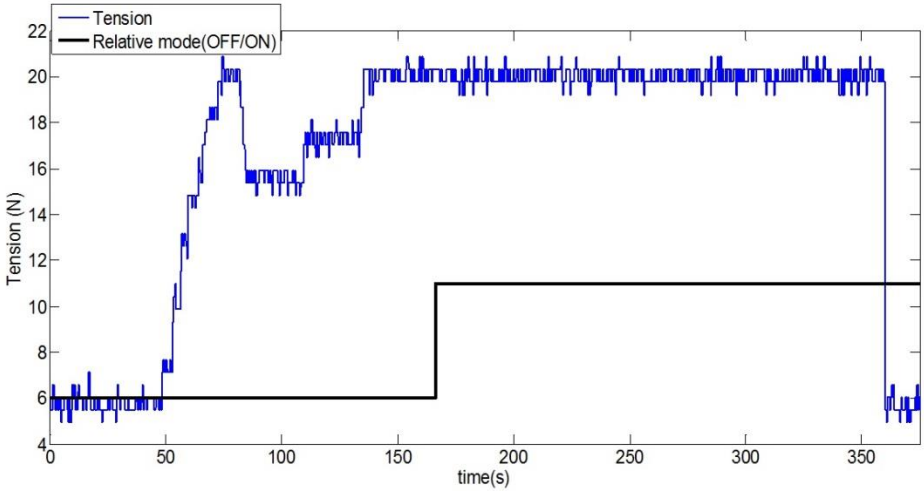

Figure 6-30: Relative mode is switched on if the tension is bigger than a threshold value during a predefined time interval.

This section is focused on the description and analysis of the tests that have been performed to validate the developed tether-based navigation system. The obtained results will show that the technique is robust. In fact, the autonomous landing of a rotary-wing UAV guided with a tether on a moving platform is demonstrated with more than 30 successful landings during two different testing campaigns. Some telemetry results will be presented in the following in order to illustrate the performance of the developed system. A video that summarizes the tests performed during the last campaign of flights can be found at (CATEC, 2019).

Tests were carried out in two different epochs of the year (October and June) and in two different locations giving place to perform the flights under different environmental conditions. This helped to check that the Guidance, Navigation and Control system is robust under different conditions. The range of the wind speed

during the tests was from 5 to 20 km/h, so according to the Beaufort scale (see Appendix A) the helicopter flew under wind conditions that reached up to sea 3 (Gentle Breeze). It is also interesting to point out that the average temperature in October was 12°C while in June it was approximately of 30°C. Changes in temperature are important since the density and pressure of the air are key factors for the lift capacity of the helicopter rotor blades. On a warm day, the density is low and the collective pitch for the rotor blades in order to keep hovering position is higher than on a cold day, with a higher density of air. Hence, it was also tested that this architecture is robust under different temperature conditions.

The tests have been performed in two different airfields. The preliminary tests were carried out in an airfield located in Utrera (Sevilla, Spain: 37° 11'49.92"N, -5° 52'50.04"O). It has an unpaved landing strip with a North-South orientation (18-36). The first test exercises were simple subsets of the final tests. The final tests with the platform moving in all axes were performed in ATLAS aerodrome. Due to the intrinsic risk of the landing procedure and the characteristics of the small helicopter used, tests with wind velocities over the 20 km/h were not carried out.

6.3.1. Experimental Setup

The experimental setup is significantly complex due to the interaction of many systems which has been specifically designed for this research work. In this section, the setup will be explained with all the actors implied in the tests. Figure 6-31 shows the complete setup, which is composed by:

- A moving platform mounted on a trolley towed by a vehicle with a tether. The platform moves vertically by means of an elevator frame pushed by an electric engine. This structure also carries a tension controller with a PC unit powered by a generator.
- A car that tows the trolley with a tether.
- A rotary-wing UAV: with avionics equipment, and joined to the platform with the tether.
- Tether system: cardan sensor on-board the UAV and reel system in the platform.
- Ground Control Centre which includes the Ground Control Station for the

UAV and the Ground Control Unit of the moving platform, since the platform can be remotely controlled in both its vertical movement and the tether tension.

- Human resources for the complete operation

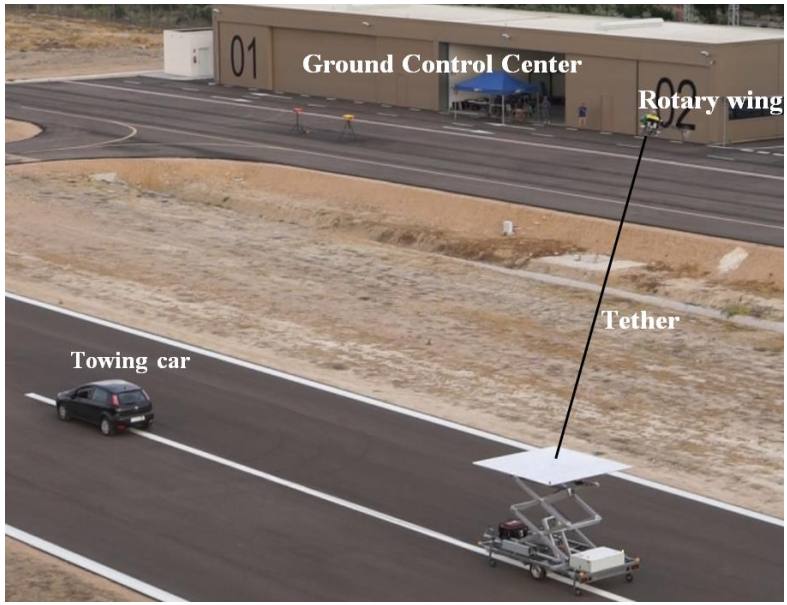

Figure 6-31: Actors of the complete experimental setup during a landing test.

The experimental phase had several stages. First of all, the rotary-wing platform with its avionics equipment was tested until a good autonomous performance was obtained. Later, the tests with the moving platform were split into the following stages:

a. Autonomous operation using relative coordinates: validation of relative coordinates navigation, being guided by the tether attached to the platform, which in this stage does not move.

b. Static landing: landing of the rotary-wing UAV on the platform using relative coordinates. In this phase, the platform also is completely static.

c. Landing moving horizontally: landing of the rotary-wing UAV on the platform using relative coordinates. The platform moves in the horizontal

frame (towed by a vehicle),

d. Landing moving vertically: landing of the rotary-wing UAV using relative coordinates on the platform which in this case it is moving in the vertical plane (pushed by an engine).

e. Landing combining all movements: landing of the rotary-wing UAV on the platform which is in movement both vertically and horizontally. This landing is guided by the tether using relative coordinates.

These steps have been followed sequentially, increasing gradually the level of difficulty in order to reduce the risks. The tests from a) to d) can be considered as initial tests for the final test (e) in which a combination of the previous tests is done.

6.3.2. Rotary wing-UAV for Tether landing tests

These experiments have been performed with the LOGO-800 RC helicopter that was introduced in section 6.2.1.1. The generic equipment consists of the autopilot developed for this work that uses a ten degrees of freedom Inertial Sensor (ADIS16407 from Analog devices) that measures angular velocities, accelerations and the magnetic field. In addition to these systems, some additional sensors have been installed in the rotary-wing UAV in order to be able to land safely by using the relative positioning navigation scheme presented previously.

- A ROKE MRII laser altimeter was equipped in order to have a centimeter-level of accuracy in the relative altitude between the RUAV and the landing platform.
- A centimeter precision Real Time Kinematics (RTK) GNSS system was also integrated into the RUAV in order to have a reference for the positioning and velocity solution obtained by using the relative configuration. These measurements were not used for estimation purposes, only as ground truth for comparison of the results obtained and benchmarking of the developed solution. The selected RTK board was the OEM628 model by Novatel. The accuracy calculated as the Root Mean Square (RMS) of this sensor in the horizontal plane is 1cm when the RTK is working and its solution is fixed.
- The cardan joint device introduced in section 3.2.3

Figure 6-32 shows the helicopter and its main components.

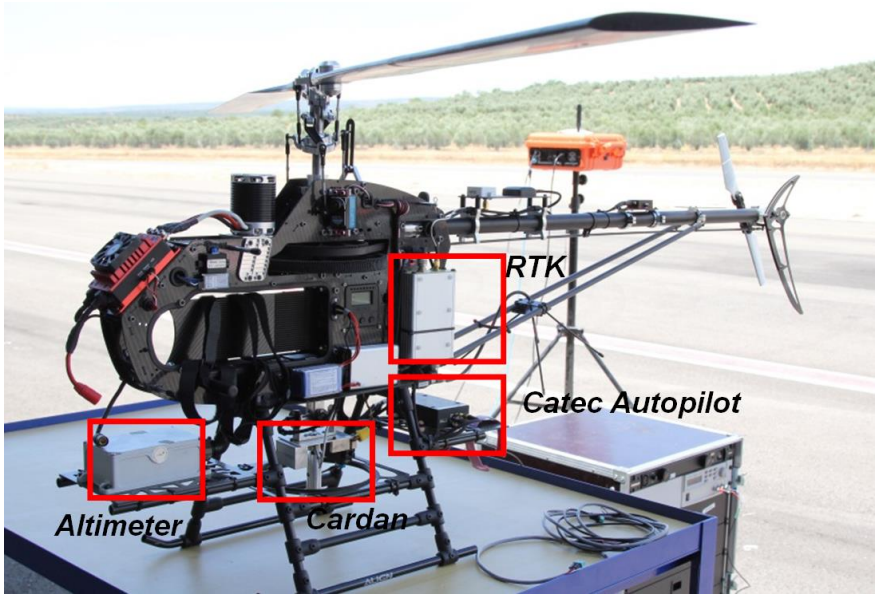

Figure 6-32: Rotary wing UAV LOGO 800 avionics

6.3.3. Analysis of the Results

This section aims to perform an analysis of the telemetry data collected during the different flight tests.

6.3.3.1. Landing on a static platform

In this scenario, the landing platform remains static, and the main goal is to land the helicopter using the relative coordinates obtained with the tether (without using GNSS). These tests were performed at the very beginning of this work in the Utrera airfield and allowed us to obtain sets of telemetry data for improving and tuning of the algorithms before starting the tests campaign in which the landing platform is in motion. All these tests start with the UAV taking off and the tether already attached but with a very low level of tension. Once the helicopter is close to the landing point, the operator commands to increase progressively the tension of the tether. Once an appropriate value of tension is reached, the helicopter starts its

landing procedure. Figure 6-33 shows some captures of the flights performed in Utrera.

Figure 6-33: Flight tests with the static platform in Utrera airfield.

Figure 6-34 shows telemetry data for a landing procedure that makes use of the relative navigation solution provided by the estimator. At the beginning of the landing, when the helicopter is hovering at 6m AGL, the error in horizontal relative navigation is larger than when the helicopter starts to descend. This fact is due to the "balloon effect" of the helicopter linked with the tether to the platform: while the tether is rolled up, the horizontal displacement of the helicopter becomes smaller helping the controller to guide the helicopter towards the relative coordinates (0,0) of the platform. This test was performed pulling the tether with the collective saturated, and increasing the tension of the tether. As it can be seen in Figure 6-34, the torque applied in the electric engine rolls the tether up and eventually defines the tension in the tether, when the tension increases (t = 968s approximately) the helicopter starts to descend, and it even reaches a descending velocity of 0.7 m/s. At this moment (t = 970s) the tension applied to the tether is decreased a little to descend more slowly. At the end of the operation, the helicopter touches down in the origin of the platform, with a very small error (less than 0.2m) and with very high tension in the tether to maintain the helicopter on ground until the engine is shut down.

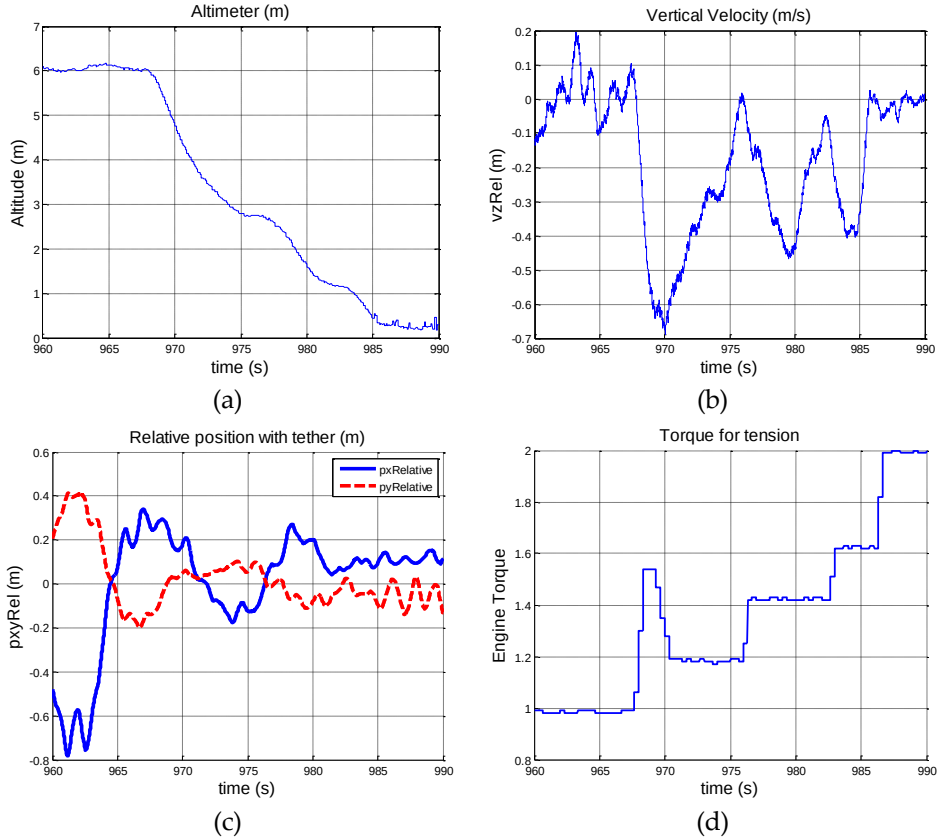

Figure 6-34: Relation between altitude (a), vertical velocity (b) and the horizontal relative position (c) with the torque (d) applied to the tether in a landing procedure over a static platform by using the developed T-GRANT module.

Another landing maneuver over the static platform is shown in order to study the accuracy of the relative estimation solution and to show that it is valid for performing an accurate and safe landing. Figure 6-35 and Figure 6-36 compare the position solution of the relative navigator with the measures of the RTK system. These plots show that the estimated relative position has centimeter level of accuracy similar to the RTK system.

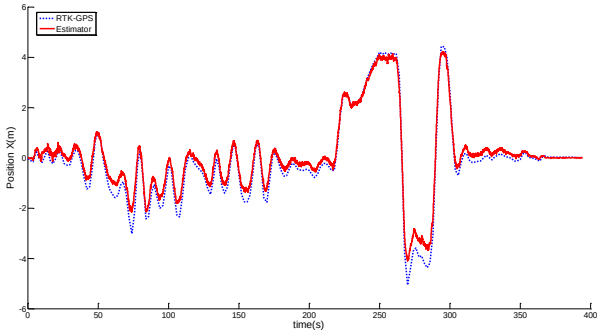

Figure 6-35: Comparison of the Horizontal Position solution obtained with the T-GRANT estimator (red line) and the RTK-GNSS sensor (blue line) during the complete test

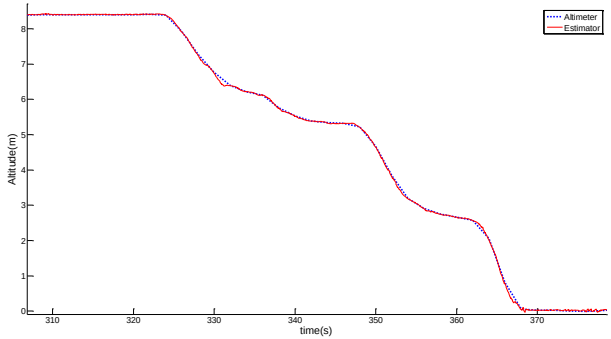

Figure 6-36: Comparison between the Vertical Position obtained with the T-GRANT estimator (red line) and the altimeter (blue line) in the last phase of the landing test.

Table 6-9 shows the root mean square error and the standard deviation (STD) of the estimated relative position. As can be seen, the positioning errors are below 20 cm, and hence the accuracy is good enough for landing safely in a platform without using a GNSS sensor.

Position	X North	Y West	Altitude
RMS error (m)	0.146	0.181	0.004
STD	0.345	0.389	0.016

Table 6-9: RMS error and Standard Deviation of the position estimation solution (m). Calculations have been performed using the RTK-GNSS system as ground truth

Figure 6-37 and Figure 6-38 compare the relative velocity solution of the relative estimator and the RTK-GPS measurements in the vertical and horizontal planes. As it can be seen, the velocity solution obtained by using the tether system is also very accurate. In Table 6-10, the calculated errors for the relative velocity are shown.

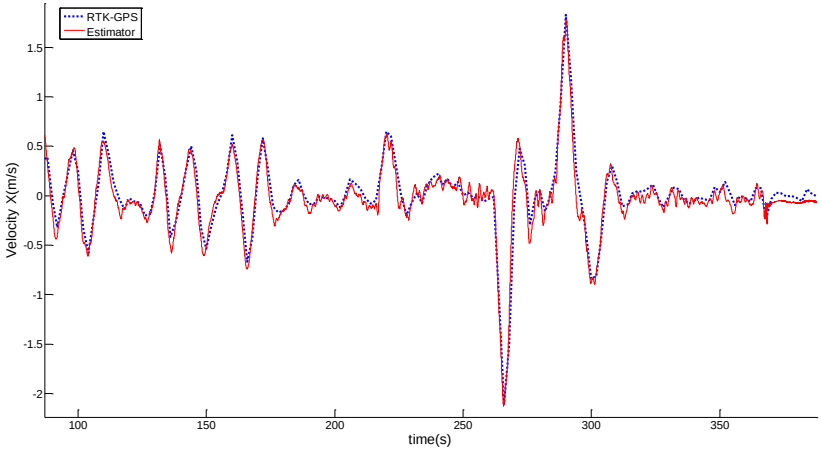

Figure 6-37: Comparison between the Horizontal velocity solution obtained with the T-GRANT estimator (red line) and the RTK-GNSS sensor (blue line) during the complete test.

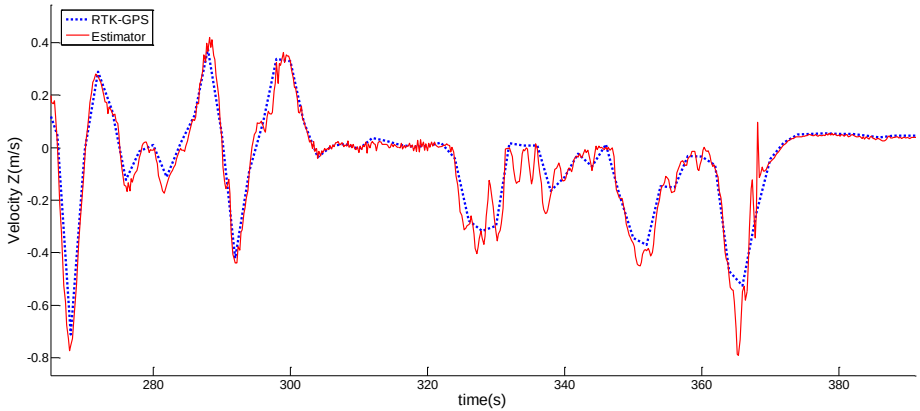

Figure 6-38: Comparison between the Vertical velocity solution using the T-GRANT estimator (red line) and the velocity solution o (blue line) during the complete test.

Velocity	X North	Y West	Altitude
RMS error (m/s)	0.077	0.073	0.056
STD	0.197	0.160	0.076

Table 6-10: RMS error and Standard Deviation of the velocity estimation solution (m/s). Calculations have been performed using the RTK-GNSS system as ground truth

Through these tests it has been also shown that another advantage of the tether is the capability of compensating the ground effect and the lift force of the helicopter when it is landed, allowing the RUAV to remain static over the landing platform until the avionics are switched off.

6.3.3.2. Landing on a moving platform: Straight maneuver

As it was commented before, during the first experimental phase, one of the objectives was to obtain telemetry data for improving the system performance through a post-processing work in our laboratory. With this feedback, the algorithms were tuned and some modifications in the code were inserted. Once these improvements were performed and implemented, it was started a second campaign of tests in the ATLAS airfield. Below, some of the tests carried out during this campaign will be described. In this campaign, the landing platform is moving with different velocities and following different types of trajectories in the horizontal and vertical planes. In this manner, it has been possible to test that:

- The autopilot can follow the landing platform in a safe and robust manner, allowing the RUAV to reach the references provided by the estimation module.
- The modified Singer model used in the navigation block provides an accurate solution also in scenarios where the landing platform is following trajectories or dynamics that are different to a straight route with constant velocity.

In this test, the landing platform is towed by a car following a straight line. It comprises two different phases: in the first one the car remains static, the helicopter takes off and the tether is tensed. The second phase starts with the movement of the car. Figure 6-39 shows these phases and makes a comparison of the relative vertical position obtained by using the developed estimator with the relative altitude obtained from the RTK sensors installed in the RUAV and the landing platform. In

this test, the UAV lands twice, and the second take-off was done during the movement.

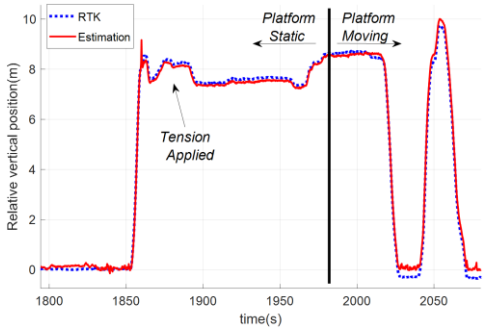

Figure 6-39: Relative vertical position during the straight movement test and its different phases: Static platform, tension applied to the tether, and start of the landing platform motion.

Here it is important to notice that when the platform oscillates vertically, the helicopter maintains the distance with respect to the moving platform. Figure 6-40 shows the relative altitude provided by the altimeter (black line), the altitude in the local navigation frame of the helicopter (blue line) and the moving platform (red line) during one oscillation of the platform. In this figure, it can be seen how the relative altitude state remains constant at the same time that the landing platform is oscillating in the z-axis. It is shown how the estimator allows flying autonomously at a constant relative altitude in scenarios where the landing platform is moving in the vertical axis.

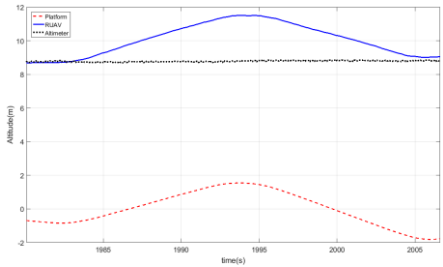

Figure 6-40: Rotary wing UAV keeps its relative altitude to the moving platform when it oscillates vertically. The altitude of the helicopter in NWU coordinates is shown in red, in blue the platform coordinates in NWU coordinates, and in black the relative altitude

between both systems measured by the altimeter.

In order to study the estimation accuracy in these tests, Figure 6-41 shows the comparison between the relative position calculated with the GNSS-RTK system (used again as ground-truth) and the relative position estimation obtained by using the tether.

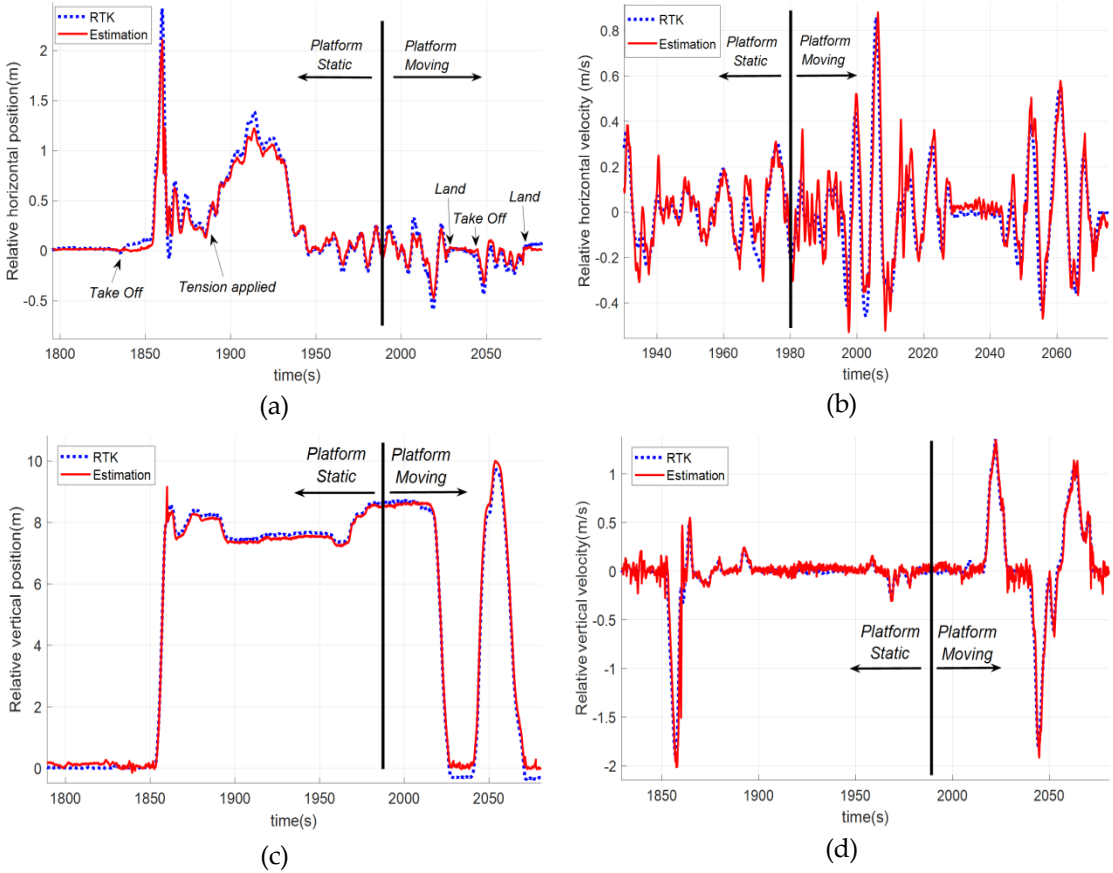

Figure 6-41: Comparison among the T-GRANT estimation solution (red) and the GNSS-RTK measurements (blue) during a test where the landing platform is moving following a straight trajectory: (a) position in the horizontal plane, (b) relative velocity in the horizontal plane, (c) relative altitude, and (d) relative vertical velocity.

In order to calculate the accuracy for the different dynamics, errors have been computed splitting the tests into the static and moving stages. In that way, it is

possible to obtain more precise knowledge about the performance of the filter for the different scenarios.

		Position			Velocity		
Platform	**Accuracy**	**X North**	**Y West**	**Altitude**	**X North**	**Y West**	**Vertical**
Static	**RMS error**	0.045	0.052	0.107	0.040	0.059	0.049
	STD	0.057	0.079	0.024	0.051	0.079	0.048
Moving	**RMS error**	0.057	0.082	0.156	0.069	0.089	0.068
	STD	0.061	0.074	0.148	0.061	0.108	0.091

Table 6-11: RMS error and Standard Deviation of the position (m) and velocity estimation solution (m/s) during a landing over a platform that is following a straight trajectory. Calculations have been performed using the RTK-GNSS system as ground truth.

From the results in Table 6-11, it can be seen that the performance of the filter in the static phase has been improved with respect to the first campaign of tests. In this case, the accuracy in both phases is better than 15 cm in position and 0.1 m/s in velocity, allowing the controller to perform the approach and land operations in a precise and safe manner. Figure 6-42 shows the trajectory of both the helicopter and the moving platform during the maneuver in the phases where the navigation module is using the tether information.

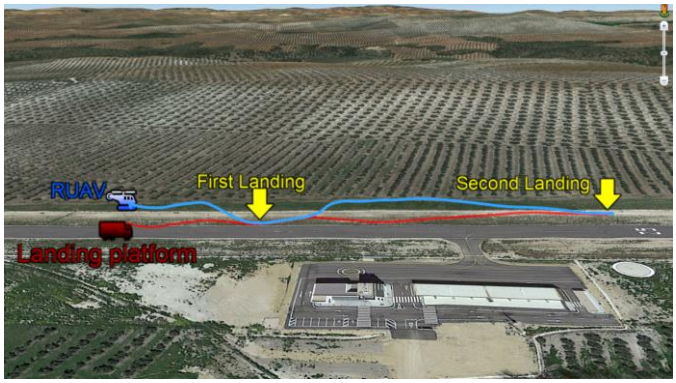

Figure 6-42: Rotary wing UAV trajectory landing on the moving platform using the tether in the straight trajectory test.

In order to analyze the behavior of the autopilot system during the approach maneuver, Figure 6-43 shows the descent phase of the first landing maneuver.

Relative altitude (a) is maintained until t=2017s approximately when the descent starts and the helicopter gets closer to the platform. Figure 6-43 also shows the vertical velocity relative to the moving platform (d), where it is shown that the maximum velocity reaches 1.5 m/s as maximun value and this value decreases slowly allowing a smooth landing. In this case, the descent was not performed pulling the RUAV by increasing the tether tension from the electric engine installed in the landing platform, but using the relative altitude information and keeping a constant value of tension. It was shown that descending using this methodology offers a more accurate and soft descent. Apart from that, the relative coordinates calculated with the tether show that the helicopter is maintained during the whole maneuver very close to the relative origin(c), so it keeps vertical to the platform.

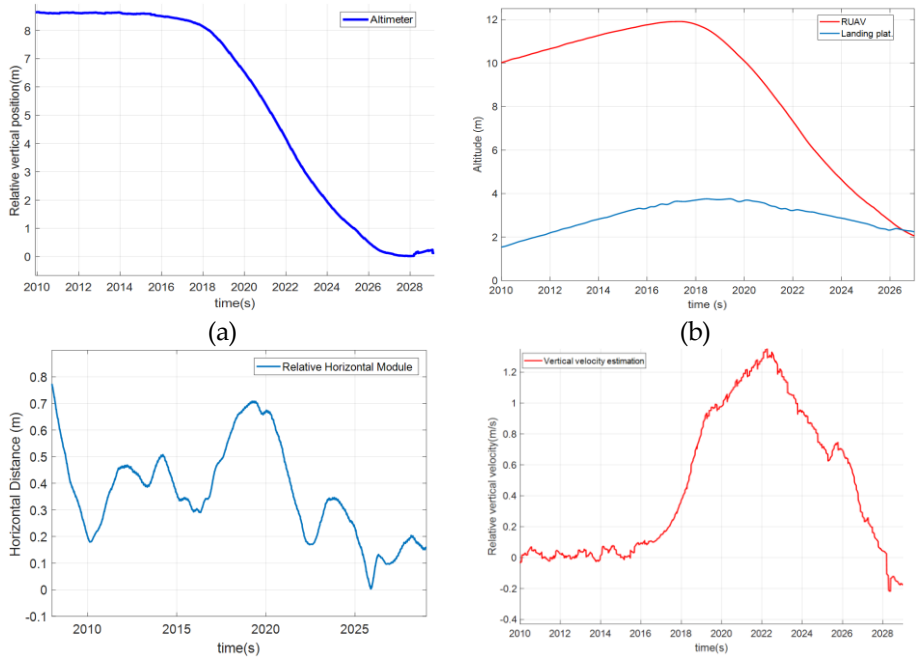

Figure 6-43: Helicopter descent phase in the straight movement test: (a) shows the altimeter measurements of the relative altitude, (b) compares the AGL of the RUAV and the moving platform, (c) shows the horizontal distance between the helicopter and the landing point, and (d) represents the vertical velocity during the descent.

Another fact that must be taken into account is the ground effect when the helicopter is close to the platform. At that moment, the tension applied to the tether increases very strongly since it has to compensate both the helicopter lift and the ground effect, which pushes the helicopter upwards. This last phase is critical in the operation since the aerodynamic disturbances in the helicopter rotor due to ground interaction make the control much more complicated.

About 20 landings were performed successfully showing the reliability of the maneuver using relative coordinates with the tether when the landing platform is following a straight trajectory. Figure 6-44 depicts one image taken from the helicopter some seconds before landing.

Figure 6-44: Helicopter goes downs vertical to the platform

6.3.3.3. Non-straight manoeuvers

In this scenario, the car towed the trolley along curvilinear paths, as it can be seen in Figure 6-45, and the goal was to test the performance of the model developed for the estimation filter in case that the trajectory of the landing platform is not straight. In this manner, it was possible to confirm that the helicopter was able to land also in vehicles that are performing more complex maneuvers.

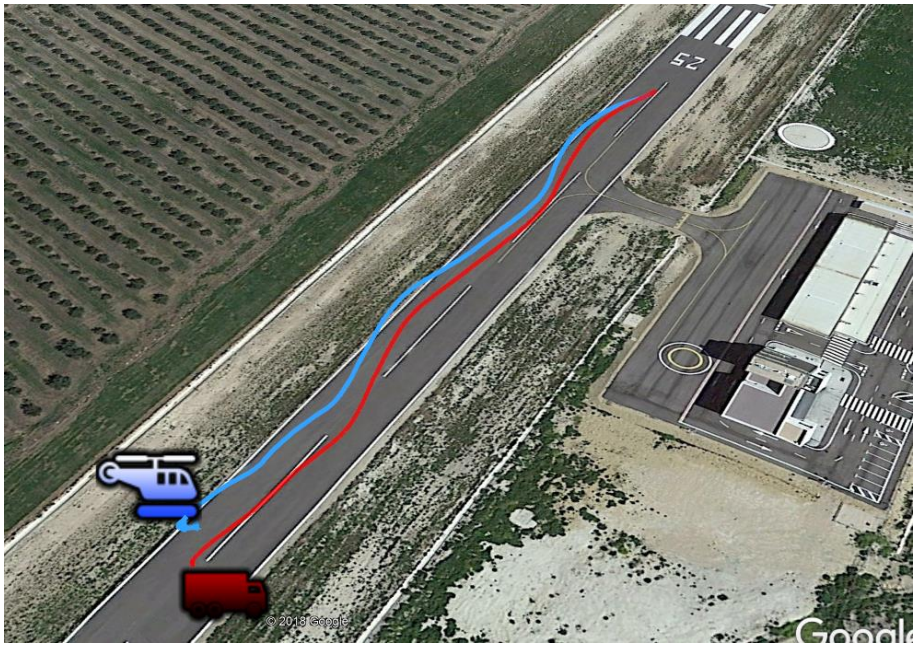

Figure 6-45: Curvilinear trajectory of the rotary-wing UAV for landing on the moving platform using the tether.

As can be seen in the following plots, the performance of the autopilot system is quite similar to the one obtained in the previous test. In, Figure 6-46 it is shown in (a) and (b) how the helicopter can maintain the relative altitude to the landing platform while this one is oscillating in the z-axis. Once the landing is commanded, the RUAV reduces this distance by performing a smooth descent until it touches the landing point. During the entire test, the UAV can closely follow the platform (c) maintaining its position over the vertical of the landing point. In this case,, the velocity of the moving platform reaches up to 18 km/h (d).

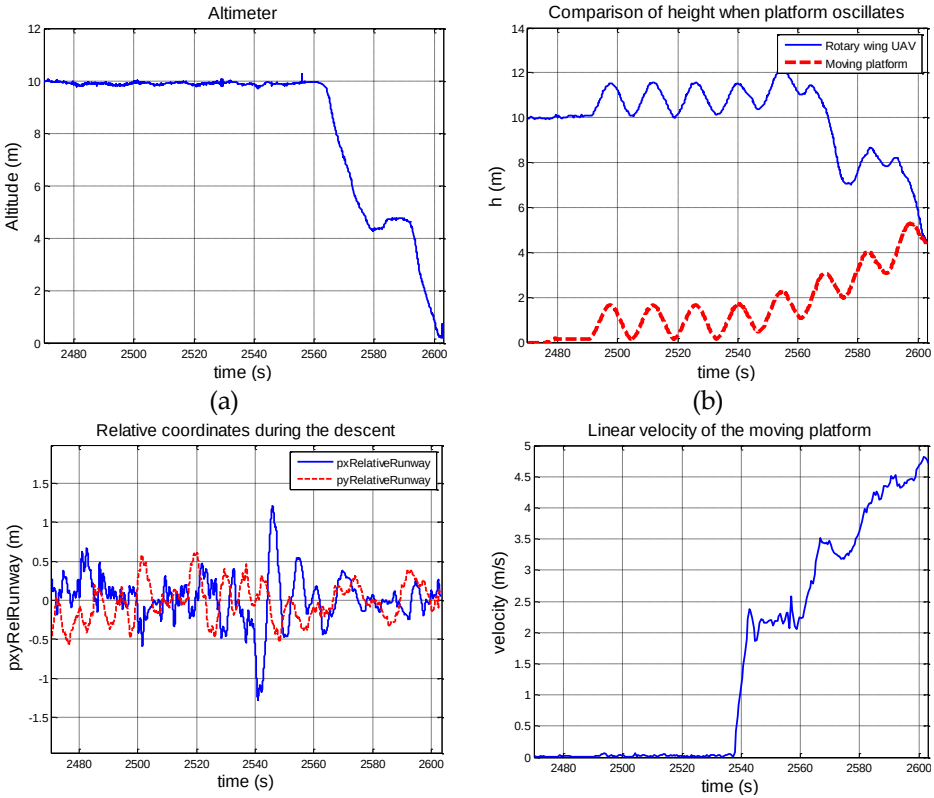

Figure 6-46: Landing maneuver data regarding curvilinear paths: (a) Relative altitude measured by the altimeter, (b) comparison between the AGL of the RUAV and the moving platform, (c) relative distance in the horizontal plane between the helicopter and the landing point, and (d) linear velocity of the moving platform during the test.

In this case, the test has also a static and a moving phase. Figure 6-47 shows the comparison between the tether based relative estimator and the RTK solution.

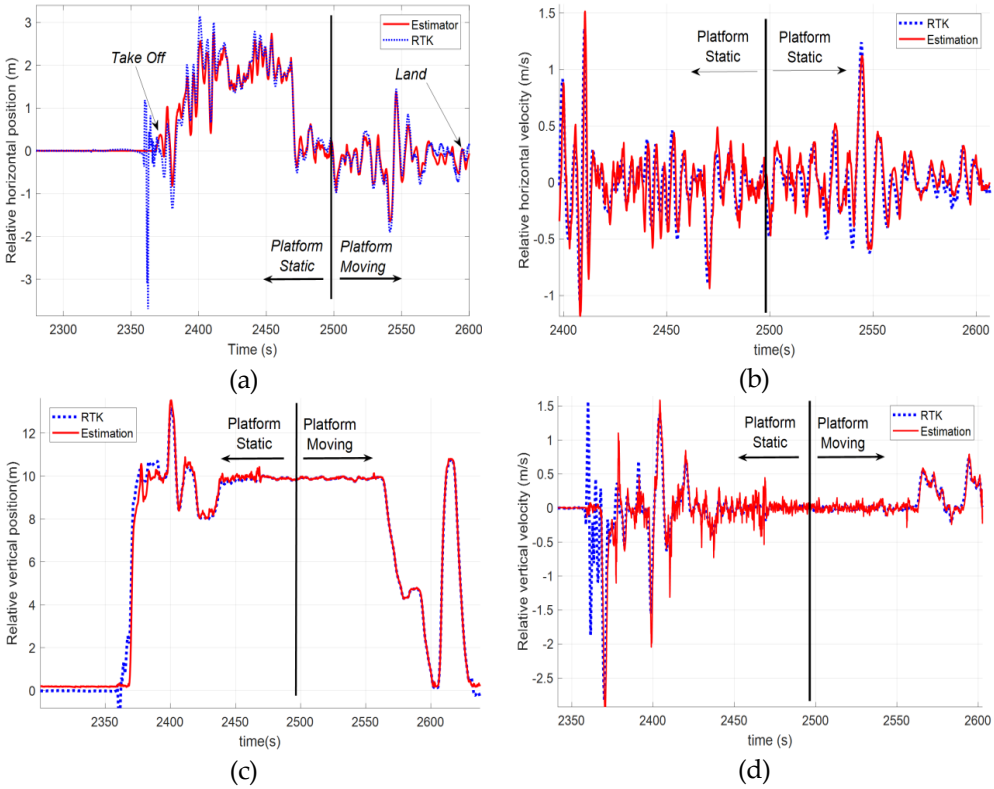

Figure 6-47: Comparison among the tether based estimation solution (red) and the GNSS-RTK system (blue) during a test where the landing platform is moving following a curvilinear trajectory: (a) measurements of the position in the horizontal plane, (b) relative velocity in the horizontal plane, (c) relative altitude and (d) relative vertical velocity.

As it can be seen in Figure 6-47, both position and velocities estimations are very accurate and follow the dynamics of the real relative vector. In the case of the relative vertical position, the output is a little bit noisy, but it does not affect the performance of the controller. Table 6-12shows the calculated errors during the static and dynamic phases of this test.

		Position			Velocity		
Platform	**Accuracy**	**X North**	**Y West**	**Altitude**	**X North**	**Y West**	**Vertical**
Static	**RMS error**	0.075	0.094	0.111	0.081	0.143	0.115
	STD	0.088	0.119	0.153	0.105	0.191	0.161
Moving	**RMS error**	0.099	0.157	0.079	0.092	0.122	0.097
	STD	0.097	0.189	0.121	0.104	0.167	0.149

Table 6-12: RMS error and Standard Deviation of the position (m) and velocity estimation (m/s) solution during a landing over a platform that is following a curvilinear trajectory. Calculations have been performed using the RTK-GNSS system as ground truth.

As can be seen in Table 6-12, the Standard deviation and RMS error have increased in the horizontal plane with respect to the straight-line movement scenario. However, the accuracy is better than 20 cm and the estimations allow the UAV to follow and land accurately in the moving platform. In this case, it has been also shown that the estimator module can provide very accurate estimations even in scenarios where the motion of the landing platform does not follow a straight line, an ideal condition that was imposed in the assumptions of the mathematical model of the estimation filter. These results confirm the robustness of the developed system, allowing its use in a wide spectrum of scenarios.

6.3.3.4. Approach and high-velocity landing

In this test, the goal was to force the helicopter to follow the moving platform at high linear velocity. The car velocity was constantly increasing with an approximate acceleration of 1.5 m/s^2 until a maximum linear velocity of approximately 10 m/s, at which the rotary-wing UAV landed. In the estimation model, it was assumed that the mean relative acceleration was due solely to the helicopter dynamics, and the rest of the accelerations were treated as a zero-mean Markov process. Thus, this test allowed the evaluation of the estimator performance in scenarios where the velocity of the landing platform is increasing at a constant rate. Figure 6-48 shows some data regarding the high-velocity tests:

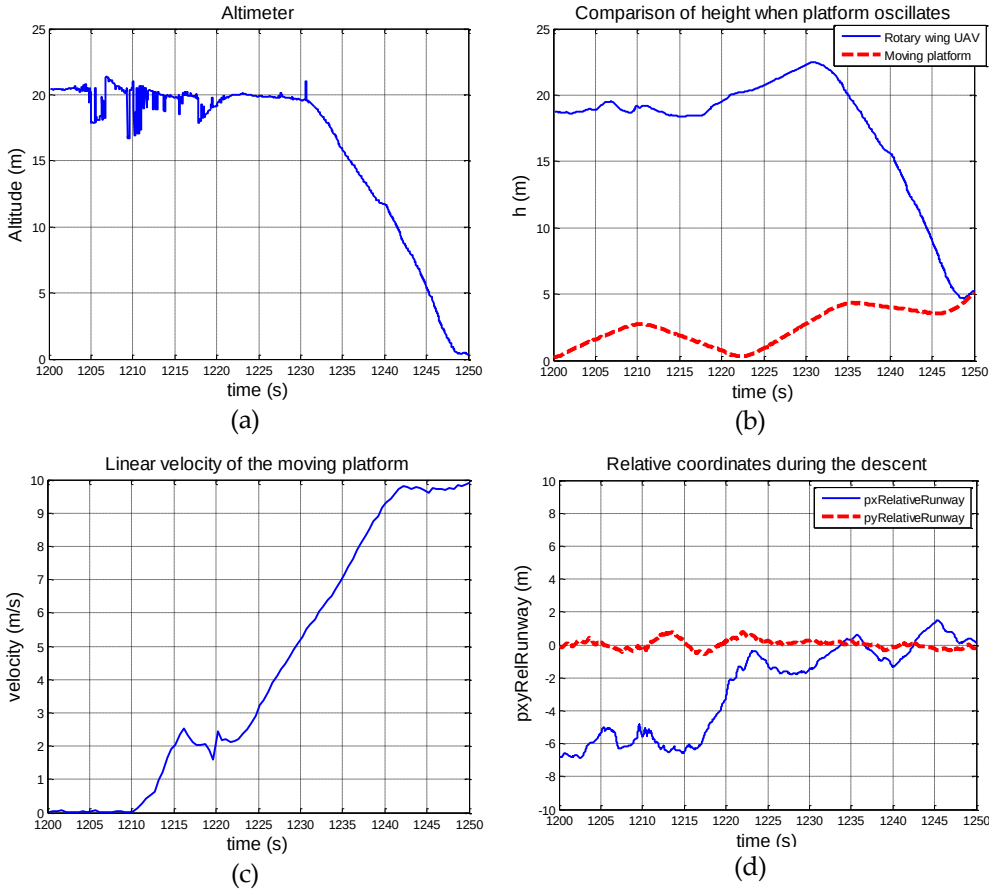

Figure 6-48: Landing maneuver data regarding high velocity test: (a) Altimeter readings during the landing procedure where it is shown the variations in the relative altitude caused by the displacement of the helicopter from a position that is over the ground to another that is over the platform, (b) AGL of the RUAV and the moving platform, (c) relative position in the horizontal axes, and (d) evolution of the landing platform velocity following a constant acceleration profile.

At the beginning of the maneuver, the rotary-wing UAV was commanded to be 5 meters behind the platform in the direction of motion in relative coordinates (see Figure 6-48) however, as it can be seen in (c), this distance appears to be larger than 6 meters. This error is due to the fact that the helicopter is not over the landing platform (whose dimensions are 3x3m). Hence, in this case, the altitude measured by the altimeter is relative to the ground. This causes an error in the equation eq.(5-13) that is propagated to the relative position measurement equations eq.(5-17)to eq. (5-19) causing the effect showed in (c). This fact suggests that during an operation, the altimeter must only be used when the UAV is over the platform in order to avoid errors in the estimations. At t=1215s the operator commands the approach to the relative origin and then the UAV reaches the vertical of the platform. From this moment it can be seen in (a) that the RUAV maintains the relative altitude to the landing platform by following its movement in the z-axis (b). At t=1231s the approach is commanded and the helicopter starts a soft descent until it lands. During this test, the car velocity was constantly increased until a linear velocity of 35 km/h (c), at which the rotary-wing UAV landed.

As in the other dynamic scenarios, this test also is compound by a static and a moving phase. Figure **6-49** shows the comparison between the tether based relative estimator and the RTK solution during the test. In all the plots it can be seen that the estimation improves at the instant in which the RUAV is over the platform (this moment is pointed in (c)). From that moment the obtained solution is very accurate and allows performing a safe landing by using these values as the state vector for the autopilot controller.

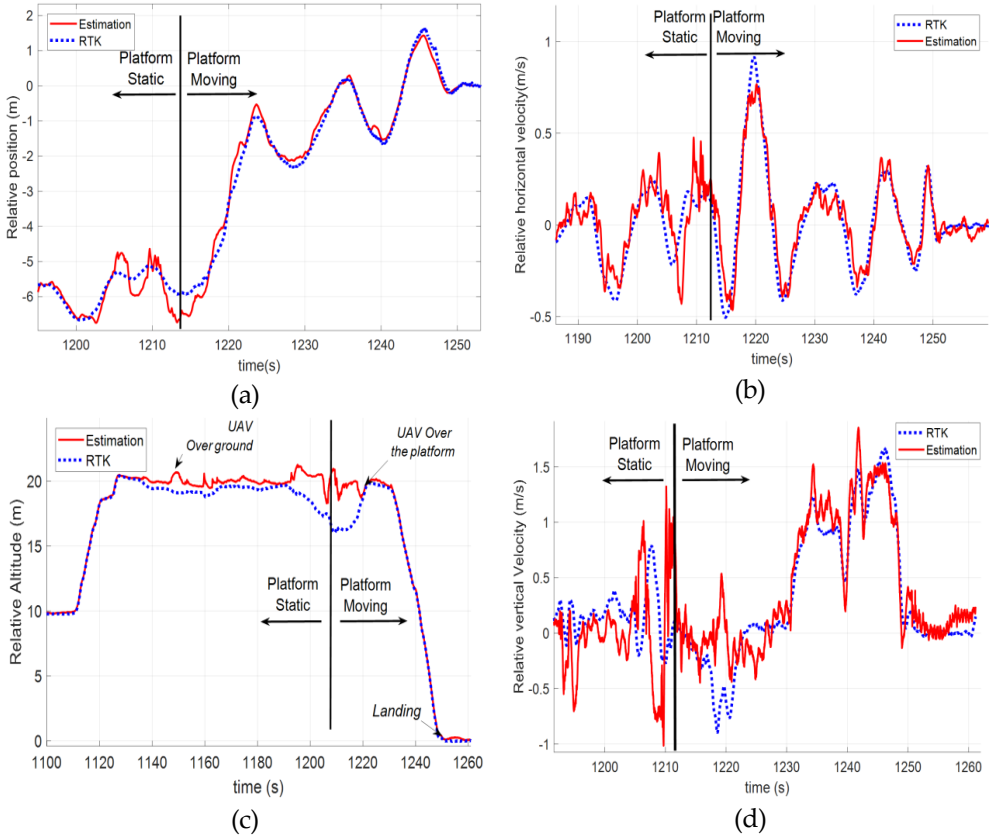

Figure 6-49: Comparison among the T-GRANT solution (red) and the GNSS-RTK (blue) measurements during a test where the landing platform is moving with a constant acceleration and reaches up to 35 km/h: (a) position in the horizontal plane, (b) relative velocity in the horizontal plane, (c) relative altitude and (d) relative vertical velocity.

Table 6-13 shows the errors in the static and dynamic phases of the test.

		Position			Velocity		
Platform	Accuracy	X North	Y West	Altitude	X North	Y West	Vertical
Static	RMS error	0.050	0.102	0.073	0.079	0.139	0.052
	STD	0.068	0.139	0.069	0.081	0.179	0.075
Moving	RMS error	0.091	0.197	0.141	0.079	0.233	0.137
	STD	0.119	0.274	0.101	0.114	0.261	0.179

Table 6-13: RMS error and Standard Deviation of the position (m) and velocity estimation (m/s) solution during a landing over a platform that is moving at high velocity with a constant acceleration. Calculations have been performed using the RTK-GNSS system as ground truth

In this case, the relative horizontal velocity estimations are a little less accurate than the obtained ones during the other tests. However, the accuracy of the velocity estimation is under 0.25 m/s and it is better than 30 cm in position. With this solution, the RUAV can perform a safe landing procedure at approximately 40 km/h over a platform that is under an accelerated movement. Also here, it is also interesting to note how the tethering mechanism facilitates to center the UAV right on top of the expected landing position, increasing the stability of the UAV during the first instants after contacting the landing platform and helping it to remain stopped.

6.4. Conclusions

This chapter describes the field experiments carried out for testing the developed navigation systems. Here, it is possible to note the strong experimental focus of this dissertation.

Regarding the experimental campaigns for testing the EIRE navigation system

developed in this thesis, this new navigator is compared with a GPS/INS navigator that does not make use of the EGNOS properties. From the results, it is possible to conclude that the average values of the lateral deviations from both solutions are similar. However, in the EIRE navigation solution, the dispersion is slightly lower. On the other side, noticeable differences are obtained in the vertical axis, where the EIRE solution improves the accuracy of the solution between 2m and 3m compared with the GPS-based solution.

Regarding the R-GRANT and the T-GRANT modules, both systems have been extensively tested in different conditions, scenarios, and under different profiles of movements of the landing platform.

From the results obtained with the R-GRANT system, it can be concluded that this navigator allows following the platform safely during the approach phase. The accuracy obtained is better than one meter and, in the nominal cases where the landing platform follows a straight trajectory, it is possible to land accurately. Another conclusion for the R-GRANT algorithm is that it would be convenient to include a method for measuring the relative heading between both platforms. In this way, it should be possible to improve the accuracy of the estimation solution an allow landing maneuvers on situations where the moving platform is performing non-straight trajectories.

Regarding the T-GRANT results obtained in the different experiments, it has been demonstrated how the helicopter is able to land safely under any movement profile of the landing platform. By analyzing the data logged during the different flights, it is concluded that the T-GRANT module is able to provide a cm accuracy solution to the controller and that the new fusion filter works correctly even in non-nominal situations that are not covered by the assumptions (non-straight trajectories and accelerated motions of the landing platform). In this way, the main conclusion is that this navigator is perfectly suitable for those landing applications that require a high level of accuracy, safety and where it is not possible to use GNSS and communication systems.

7. CONCLUSIONS AND FUTURE WORK

7.1. GNSS-free relative Navigation System

This research has presented a novel navigation architecture based on a tether and a radio-beacon system that allow a safe and accurate landing procedure of a rotary wing UAV over a moving platform. Tests in chapter 6 have demonstrated that this novel approach, with a new fusion algorithm that makes use only of local sensors for the relative position and velocity estimation, can provide centimeter accuracy in the absence of GNSS. At the same time, it has been implemented an acceleration model based on a time-correlated model of the acceleration with non-zero mean that has been shown to be robust against different trajectories and velocity profiles of the landing platform. This solution allows closing the UAV control system to carry out a safe landing on static and moving platforms and compensates perturbations or un-modeled behaviors of the landing platform during its movement. The obtained results are very promising as they offer an alternative positioning method to GNSS allowing to land in environments with low visibility of the GNSS constellations or where the satellite signals can be jammed.

7.1.1. T-GRANT system conclusions

Few references about tethered UAVs can be found in the existing literature. Many of these works describe the design of non-linear control system and the stabilization properties that the tether provides to the aerial platform, providing mainly simulation results. Few papers provide experimental results for the tethered landing UAV maneuver, and most of them are for static landing platforms in controlled indoor scenarios. Objectives on these tests are more focused on the hovering and stabilization capabilities of the UAV than in the landing procedure.

Through the real flights performed along this thesis, it has been proved that the T_GRANT system developed is able to provide relative measurements at 100Hz with centimeter accuracy, allowing the autonomous control of the helicopter in a huge variety of scenarios, especially in one of the most challenging ones: landing on a moving platform in absence of GPS.

In the two last test campaigns, approximately 90% of the autonomous landing procedures were completed successfully without the intervention of the remote pilot in any phase (about 30 landings). Problems in the remaining cases were due mainly to the fact that some experiments were carried on with strong decelerations in the car velocity: If the acceleration/deceleration occurs when the helicopter is descending to touch down and the relative altitude to the platform is very low, the helicopter may not be fast enough to compensate this acceleration/deceleration. However, in conventional operations, the dynamics of the RUAV are much faster than the landing platform's motion, so this issue would not represent any problem.

In the operation procedure for these tests, the helicopter took-off already attached to the platform by the tether; hence, the tether release from the helicopter and its attachment to the platform device to be rolled is not taken into account. Hence, the release of the tether from the helicopter can be a gap to be solved for real operations. The down-wash created by the helicopter can lead to undesired motion in the rope during the release.

7.1.2. R-GRANT system conclusions

The experiments presented in section 6.2 were intended to demonstrate the feasibility of guiding and landing a rotary wing UAV on a moving platform using data from the RBS sensor for obtaining the relative positioning vector. From the experimentation results, it can be concluded that the RBS-based navigator allows performing the final approach and the landing maneuver in those scenarios where a relative accuracy of approximately one meter is enough. However, some improvements should be done in the RBS performance in low relative velocities, so that the touchdown phase can be done even with more guarantees. RBS performance is much better when the relative velocity is not low, so the approach phase is expected to have better results than the final touchdown stage when the

relative velocity is low.

Regarding the integration of RBS equipment on the unmanned rotary wing UAV, some issues must be taken into account for the right performance. The airborne antennas must have direct line-of-sight with the GSU antennas, so they cannot be obstructed by any object either by high attitudes of the UAV or foreign objects which could appear in the area of operation. They must be consistently installed in the structure, avoiding vibrations of the structure.

7.2. EIRE Global Navigation System

In this thesis, it has been developed, integrated and tested a new navigation system that makes use of the EGNOS information for improving the navigation and guidance capabilities of a UAV. One of the novelties proposed in this research has been the use of the integrity information to improve the accuracy, robustness and safety of autopilot system even in cases of GNSS degradation. Based on the results obtained during the experiments presented in section 6.1, it is possible to conclude that using the SBAS corrections and the integrity information in the global navigator developed, the position and velocity accuracy of the estimation process is better than the obtained by those navigators that only rely on the GPS constellation. More specifically, by comparing the solution of the EIRE estimator developed in this thesis with the results obtained through the same navigation architecture but using only the GPS measurements, it has been identified that our navigator provides noticeable benefits, especially on the vertical axis where the error is reduced around 2m or 3m.

Additionally, the architecture developed also has proven to provide benefits in the UAV surveillance by providing the HPL, VPL and the state of the satellite constellations as additional information to the remote pilot during the whole operation. This information helps the remote pilot to have a more complete awareness of the operation status while flying the UAV. Here, the integrity information can be also used for preventing the complete loss of the satellite signals and, in this way, it is avoided that the UAV enters in an emergency state where there is not any positional source for controlling the aircraft.

7.3. Future Work

On one part, regarding the GRANT algorithms, future developments will involve the use of a 3D LIDAR sensor in order to have another source of relative position measurements and to provide the relative attitude between the RUAV and the landing platform. This will allow testing different estimation models and to land in more complex scenarios where the pitch and roll of the landing platform can change. More specifically, with respect to the R-GRANT algorithm, due to the relative heading information is required for obtaining the best accuracy possible from this system, future work could include the integration of visual algorithms or the use of two antennas for obtaining the heading of the landing platform. In this way, it will be possible to improve the accuracy of the R-GRANT system in those maneuvers where the landing platform is in motion, by minimizing the error to approximately 30 cm, which is the error obtained during the static experiments. Finally, in a future implementation of the GRANT estimation filter, a tightly coupled architecture can be implemented and tested in order to check if the accuracy of the estimations can be improved by introducing the raw measurements of the sensors in the measurement model of an EKF.

On the other hand, from the results obtained with the EIRE navigator, it has been detected that the protection levels could be used in a next step to increase the safety of the UAV operation with respect other airspace users. In this framework, one feasible solution could be to take advantage of the position integrity offered by EGNOS and use the computed PL's to create an area of uncertainty around the UAV. In this way, if this concept is added to the use of the ADS-B technology, it could ensure that all airspace users are aware of the position of all other in a more accurate way and using the Protection Level as additional information for improving the positional awareness of their guidance systems and helping to avoid collisions.

(...

REFERENCES

Acevedo, J. J., García, M., Pablo, R., Arrue, B., Ollero, A. (2018). Autonomous Landing of a Multicopter on a Moving Platform Based on Vision Techniques. In *ROBOT 2017: Third Iberian Robotics Conference,* pp. 272-282. Springer International Publish*in*g. DOI:10.1002/0471221279

Alarcón, F., Cordero, M., Wal, V, et al (2013). EGNOS-based navigation solution for RPAS in precision agriculture applications. In *European Civil RPAS Regulation Implementation & U-Space Integration Forum (RPAS 2013)*. Brussels. Retrieved from http://quantalab.ias.csic.es/pdf/Cordero-Miguel_CATEC_Spain_WP.pdf

Alarcón, F., García, M., Maza, I., Viguria, A., Ollero, A. (2019). A Precise and GNSS-Free Landing System on Moving Platforms for Rotary-Wing UAVs. *Sensors , 19* (4), doi: https://doi.org/10.3390/s19040886

Alarcón, F., Santamaría, D., Viguria, A. (2015). UAV helicopter relative state estimation for autonomous landing on moving platforms in a GPS-denied scenario. *IFAC-Papers Online , 48* (9), pp. 37-42.

Alarcón, F., Santamaría, D., Viguria, A., Ollero, A., Heredia, G. (2015). Helicopter GNC system for autonomous landing by using a tether in a GPS denied scenario. *2015 International Conference on Unmanned Aircraft Systems (ICUAS)*, pp. 1067-1073. Denver.

Bar-Shalom, Y., Li, X. R., Kirubarajan, T. (2001). *Estimation with Applications to Tracking and Navigation: Theory, Algorithms, and Software.* New York,NY: John Wiley and Sons. DOI: 10.1007/978-3-319-70836-2_23

Bijker's, J. (2006). *Development of an Attitude Heading Reference System for an Airship*. Thesis. MScEng Electrical and Electronic Engineering, University of Stellenbosch, 2006.

Blackman, S. S., Popoli, R. F. (1999). *Design and Analysis of Modern Tracking Systems.* Boston: Artech House. ISBN: 1580530060

Brown, R. G., Hwang, P. Y. (1997). *Introduction to random signals and applied Kalman Filtering.* New York, NY: John Willey & Sons. ISBN: 0–47152–573–1

Bruckner, D., Graas, F. v., Skidmore, T. (2011). Approximations to composite GPS protection levels for aircraft precision approach and landing. *GPS Solution*, 15(4), pp.333-344.

Caruso, M. J. (2000). Applications of magnetic sensors for low cost compass systems. *IEEE 2000.Position Location and Navigation Symposium*. San Diego, CA, USA, pp. 177-184.

Caruso, M. J. (1997). *Applications of Magnetoresistive Sensors in Navigation Systems.* SAE Technical Paper 970602, doi: https://doi.org/10.4271/970602. .

CATEC. (2015, 07). *Video Proyecto EC-SAFEMOBILE aterrizaje UAV*. Retrieved from https://www.youtube.com/watch?v=LdTiHJ5E0uo

Chiesa, S., Cresto, S., Di Meo, G., Fusaro, R., & Viola, N. (2014). Autonomous Take-Off and landing for Unmanned Aircraft System: Risk and Safety Analysys. *29th Congress of the International Council of the Aeronautical Sciences (ICAS 2014).* St. Petersburg.

Cloutier, J. R., Evers, J. H., & Feeley, J. J. (1989). Assessment of air-to-air missile guidance and control technology. *IEEE Control Systems Magazine* , vol. 9 (6), pp. 27-34

Colomina, I., Blázquez, M., Molina, P., Parés, M. E. (2008). Towards a New Paradigm for High-resolution Low-cost Photogrammetryand Remote Sensing. *Remote Sensing and Spatial Information Sciences. XXI ISPRS Congress,* Beijing (China),.

Ding, W. (2009). *Optimal Integration of GPS with Inertial Sensors:Modeling and implementation.* MSc Thesis, University of New South Wales. Surveying &Spatial Information Systems ,Sydney.

EC-SAFEMOBIL (2016, 03). *EC-SAFEMOBILE: Final Experiments of the 5 Scenarios.* Retrieved from https://www.youtube.com/watch?v=-xNBY21h0Yw

Erdelj, M., Natalizio, E., Chowdhury, K., Akyldiz, I. F. (2017). Help from the Sky: Leveraging UAVs for Disaster Management. *IEEE Pervasive Computing*, vol. 16 (1), pp. 24-32

ESA. (2011). *ESA Navipedia Integrity*. Retrieved from https://gssc.esa.int/navipedia/index.php/Integrity

ESA. (2009). *User guide for EGNOS application developers.* EU Publications, doi: 10.2769/22157

Esmat, B. (2007). *Introduction To Modern Navigation Systems.* Singapore: World Scientific Publishing. DOI: https://doi.org/10.1142/6481

European Global Navigation Satellite System Agency (2018,06). *What is EGNOS?* Retrieved from https://www.gsa.europa.eu/egnos/what-egnos

European Space Agency. (2019, 02). *About OS.* Retrieved from https://egnos-user-support.essp-sas.eu/new_egnos_ops/services/about-os

Falanga, D., Zanchettin, A., Simovic, A., Delmerico, J., Scaramuzza, D. (2017). Vision-based autonomous quadrotor landing on a moving platform. In *2017 IEEE International Symposium on Safety, Security and Rescue Robotics (SSRR),*Shangai, pp. 200-207.

Falco, G., Einicke, G., MAlos, J., Dovis, F. (2012). PErformance Analysis of Constrained Loosely Coupled GPS/INS Integration Solutions. *Sensors* 12(11), pp. 15983–16007, doi:10.3390/s121115983

Falco, G., Pini, M., & Marucco, G. (2017). Loose and Tight GNSS/INS Integrations: Comparison of Performance Assessed in Real Urban Scenarios. *Sensors* 17(2), doi:10.3390/s17020255

Ganesh, Y., Raju, R., Hegde, R. (2017). Surveillance Drone for Landmine Detection. *Chennai: 2015 International Conference on Advanced Computing and Communications (ADCOM),*Chennai, pp. 33-38.

Glick, T., Arogeti, S. (2018). Control of Tethered Drones with state and input Constraints - a Unified Model Approach. In *2018 International Conference on Unmanned Aircraft Systems (ICUAS)*, pp. 995-1002.

Grewal, M. S., Andrews, A. P. (2001). *Kalman Filtering: Theory and Practice Using MATLAB.* New York, NY: John Wiley & Sons, doi: 10.1002/9780470377819

Grewal, M. S., Lawrence, W. R., Angus, A. P. (2007). *Global Positioning Systems, Inertial Navigation, and Integration.* New York, NY: John Wiley and Sons, doi: 10.1002/0470099720

Han, S., Wang, J. (2011). A novel method to integrate IMU and Magnetometers in Attitude and heading reference systems. *Journal of Navigation , 64* (4), pp. 727-738.

José Santa, B. Ú. (2006). Monitoring the position integrity in road transport localization based services. *IEEE Vehicular Technology Conference.* Montreal, pp. 1-5.

Kim, E., & Choi, D. (2016). A UWB positioning network enabling unmanned aircraft systems auto land. *Aerospace Science and Technology , 58*, 410-426.

Kim, S. J., & Lim, G. J. (2018). Drone-Aided Border Surveillance with an Electrification Line Battery Charging System. *Journal of Intelligent & Robotic Systems,* 92(2),pp. 657-670

Kinsman, B. (1965). *Wind Waves Their Generation and Propagation on the Ocean Surface.* Prentice Hall, New Jersey, doi: 10.1126/science.150.3697.737-a

Kiribayashi, S., Yakushigawa, K., Nagatani, K. (2017). Position estimation of tethered micro unmanned aerial vehicle by observing the slack tether. *IEEE International Symposium on Safety, Security and Rescue Robotics (SSRR)*, Shangai, pp. 159-165.

Kristan, M., Kovacic, S., Leonardis, A., Pers, J. (2009). A local-motion-based probabilistic model for visual tracking. *Pattern Recognition*, 42(9),pp: 2160-2168.

Madwick, S. O., Harrison, A. J., Vaidyanathan, A. (2011). Estimation of IMU and MARG orientation using a gradient descent algorithm. 2*011 IEEE International Conference on Rehabilitation Robotics*, Zurich, pp. 1-7

Máthé, K., & Busoniu, L. (2015). Vision and Control for UAVs: A Survey of General Methods and of Inexpensive Platforms for Infrastructure Inspection. *Sensors, 15* (7), pp 14887-14916

McAree, O., AitKen, J. M., & Veres, S. M. (2016). A model based design framework for safety verification of a semi-autonomous inspection drone. *Belfast: 2016 UKACC 11th International Conference on Control (CONTROL)*, Belfast, pp. 1-6

Mcgeer, B. T., & Von Flotow, A. H. (2013). Method and apparatus for automated launch, retrieval, and servicing of a hovering aircraft. Underwood: *United States Patent 8453966.*

Merz, T., Duranti, S., Conte, G., Marcelo, A., Khatib, O. (2006). Autonomous Landing of an Unmanned Helicopter based on Vision and Inertial Sensing. *Experimental Robotics IX. Springer Tracts in Advanced Robotics,* 21, pp. 343-352. Springer Berlin Heidelberg.

Mfiri, J., T, Treurnicht, J., Engelbrecht, J. A. (2016). Automated landing of a tethered quad-rotor UAV with constant winching force. *2016 Pattern Recognition Association of South Africa and Robotics and Mechatronics International Conference (PRASA-*

RobMech) ,Stellenbosh, pp. 1-6.

Molina, P., Blázquez, M., Sastre, J., Colomina, I. (2015). A method for simultaneous aerial and terrestrial geodata adcquisition for corridor mapping. *Remote Sensing and Spatial Information Sciences,* XL-1/W4, pp. 227–232., doi: 10.5194/isprsarchives-XL-1-W4-227-2015

Molina, P., Colomina, I., Silva, P. F., Stebler, Y., Skaloud, J., kornus, W., et al. (2011). EGNOS-based multi-sensor accurate and reliable navigation. *Remote Sensing and Spatial Information Sciences, XXXVIII-1/C22, doi:* 10.5194/isprsarchives-XXXVIII-1-C22-87-2011

Molina, P., Colomina, I., Vitoria, I., Silva, P. F., et al (2011). Integrity Aspects of Hybrid EGNOS-based Navigation on Support of Search-And-Rescue Missions with UAVs. *Proceedings of the 24th International Technical Meeting of The Satellite Division of the Institute of Navigation (ION GNSS 2011)*, pp. 3773-3781.

Nicotra, M. M., Nald, R., & Garone, E. (2017). Nonlinear control of a tethered UAV: The taut cable case. *Automatica, 78*, pp. 174 - 184.

Noureldin, A., Karamat, T., Georgy, J. (2013). *Fundamentals of Inertial Navigation, Satellite-based Positioning and their Integratio*n. Springer. doi: 10.1007/978-3-642-30466-8

Oh, S.-R., Pathak, K., Agrawal, S. K., Pota, H., Garratt, M. (2006). Approaches for a tether-guided landing of an autonomous helicopter. *IEEE Transactions on Robotics, 22* (3), pp. 536-544.

Peng, X., Yang, K., & Liu, C. (2015). Maneuvering Target Tracking Using Current Statistical Model Based Adaptive UKF for Wireless Sensor Network. *Journal of Communications, 10* (8), pp. 579-588

Petovello, M. (2003). *Real-time Integration of a Tactical-Grade IMU and GPS for High-Accuracy Positioning and Navigation,* (Msc Thesis) University of Calgary-Canada.

Półłka, M., Ptak, S., Kuziora, Ł., & Kuczyńska, A. (2018). The Use of Unmanned Aerial Vehicles by Urban Search and Rescue. *Conference PROLOG 2018*. UK, doi: 10.5772/intechopen.73320

Polvara, R., Sharma, S., Wan, J., Manning, A., Sutton, R. (2018). Vision-Based Autonomous Landing of a Quadrotor on the Perturbed Deck of an Unmanned Surface Vehicle. *Drone*s, 2 (2), 15, doi: https://doi.org/10.3390/drones2020015

Price, R. G., & Bishop, R. E. (1974). *Probabilistic Theory of Ship Dynamics.* New york,

NY: John Wiley & Sons. ISBN: 0412124300

Rapatz, P. (1991). *Vessel Heave determination using the global positioning system*. Technical Report No. 155, Retrieved from: Department of Surveying Engineering, University of New Brunswick, Canada, website: http://www2.unb.ca/gge/Pubs/TR155.pdf.

Robotics vision and Control group. Retrieved from http://grvc.us.es/aware/videos/videos.shtml

Rong Li, X., & Jilkov, V. P. (2003). Survey of Maneuvering Target Tracking Part I: Dynamic Models. *IEEE Transactions on Aerospace and Electronic Systems, 39* (4), pp. 1333-1364.

RUAG (2012,03). *RUAG's Laser-Based Automatic UAS Landing System*. Retrieved from https://www.uasvision.com/2012/03/02/ruags-laser-based-automatic-uas-landing-system/

Rye, D. (1985). Longitudinal stability of a hovering, tethered rotorcraft. *Journal of Guidance, Control, and Dynamics ,8* (6), pp. 743-752

Salychev, O. S. (2004). *Applied inertial navigation problems and solutions*. BMSTU: Moscow.ISBN: 5703823951

Sandino, L. A., Santamaria, D., Bejar, Viguria, A., M., Kondak, K., Ollero, A. (2014). Tether-guided landing of unmanned helicopters without GPS sensors. *In Proceedings of the International Conference on Robotics and Automation*, pages 3096–3101. IEEE

Sandino, L. A.,Bejar, M., Kondak, K., and Ollero,A. (2015) A Square-Root Unscented Kalman Filter for attitude and relative position estimation of a tethered unmanned helicopter. *In Proceedings of the International Conference on Unmanned Aircraft Systems*, pages 567–576. IEEE

Sandino, L. A., Santamaria, D., Bejar, M., Kondak, K., Viguria, A., Ollero, A. (2016). First experimental results on enhancing hovering performance of unmanned helicopters by using a tethered setup. *Robotics and Autonomous Systems , 79*, pp. 147-155.

Sandino Velásquez, L. A. (2016). *Modeling and control techniques of autonomous helicopters for landing on moving platforms*, (MscThesis) Departamento de Ingeniería de Sistemas y Automática, Universidad de Sevilla, Sevilla.

Sandino, L. A., Santamaria, D., Bejar, M., Kondak, K., Viguria, A., Ollero, A. (2016).

First experimental results on enhancing hovering performance of unmanned helicopters by using a tethered setup. *Robotics and Autonomous Systems , 79*, pp. 147-155.

Saripalli, S., Montgomery, J. F., Sukhatme, G. S. (2003). Visually guided landing of an unmanned aerial vehicle. *IEEE Transactions on Robotics and Automation , 19* (3), pp. 371-380.

Saripalli, Srikanth, Sukhatme, Gaurav. (2006). Landing on a Moving Target Using an Autonomous Helicopter. *Field and Service Robotics: Recent Advances in Research and Applications*, pp. 277-286. Springer Berlin Heidelberg.

Schmidt, G., & Swik, R. (1974). Automatic hover control of an unmanned tethered rotorplatform. *Automatica*, 10 (4), pp. 393-394

Setoodeh, P., Khayatian, A., Frajah, E. (2004). Attitude Estimation By Separate-Bias Kalman Filter-Based Data Fusion. *Journal of Navigation, 57* (2), pp. 261-273.

Shin, E. H. (2005). *Estimation Techniques for Low-Cost Inertial Navigation,* (Msc Thesis) University of Calgary,Canada.

Sierra Nevada Corporation. *https://www.sncorp.com/media/1998/ucars-v2product-sheet.pdf*. Retrieved from https://www.sncorp.com/media/1998/ucars-v2product-sheet.pdf

Simpson, D. G. (2018). *Introductory Physics II: Waves, Acoustics, Electromagnetism, Optics, and Modern Physics.* Retrieved from : Department of Physical Sciences and Engineering,Prince George's Community College,Largo ,Maryland, website: http://www.pgccphy.net/1020/phy1020.pdf

Singer, R. A. (1970). Estimating optimal tracking filter performance for manned maneureving tragets. *Transactions on Aerospace and Electronic Systems* , AES-6 (4), pp. 473-483

Solimeno, A. (2007). *A Low-Cost INS/GPS Data Fusion with Extended Kalman Filter for Airborne Applications.* (M.Sc. Thesis) Universidad Tecnica de Lisboa, Lisboa, Portugal.

Stewart, R. (2009). *Introduction to Physical Oceanograph.* Orange Grove Books. ISBN: 1616100451

Stumberg, L. v., Usenko, V., Engel, J., Stükler, J., Cremers, D. (2017). From monocular SLAM to autonomous drone exploration. *Paris: 2017 European*

Conference on Mobile Robots (ECMR), pp. 1-8

Tamouridou, A. A., Alexandridis, T. K., Pantazi, X. E., Lagopodi, A., et al. (2017). Application of Multilayer Perceptron with Automatic Relevance Determination on Weed Mapping Using UAV Multispectral Imagery. *Sensors 17 (10)*, doi: 10.3390/s17102307

The Radio Technical Comission for Aeronautics. (2016). *RTCA DO-229 Minimum Operational Performance Standards for Global Positioning System/Satellite-Based Augmentation System Airborne Equipment.*

U.K National Meteorological Library and Archive. (2012). *The Beaufort Scale.* Retrieve from: National Meteorological Library and Archive Fact sheet 6 -. Technical Report, U.K., website: https://www.metoffice.gov.uk/binaries/content/assets/metofficegovuk/pdf/research/library-and-archive/library/publications/factsheets/factsheet_6-the-beaufort-scale.pdf

U.S. Department of Transportation. (2013). *Helicopter Flying Handbook.* Oklahoma City, USA: Createspace Independent Pub. ISBN: 1490465154

Vahidi, V., Saberinia, E. (2018). MIMO channel estimation and evaluation for airborne traffic surveillance in cellular networks. *Journal of Applied Remote Sensing, 12 (1),* doi: 10.1117/1.JRS.12.016034

VICON. (2019, 8 31). *https://www.vicon.com/*. Retrieved from https://www.vicon.com/

Weiwei, K., Hu, T., Zhang, D., Shen, L., Zhang, J. (2017). Localization Framework for Real-Time Autonomous Landing: An On-Ground Deployed Visual Approach. *Sensors, 17* (6), doi: 10.3390/s17061437.

Xiao, X., Fan, Y., Dufek, J., Murphy, R. (2018). Indoor UAV Localization Using a Tether. In *2018 IEEE International Symposium on Safety, Security, and Rescue Robotics (SSRR)*, pp. 1-6.

XSENS. (2019, 08). *MTI-G (legacy product)*. Retrieved from https://www.xsens.com/products/mti-g/

Appendix A

This appendix contains the assumptions and the constraints of the landing platform motion in order to study its similarities with the movement of a ship under different environmental conditions. Regarding the landing platform development, it is important to state that the objective was mainly to have a platform able of performing movements in the vertical axis in order to test automated landing maneuvers in scenarios where the vehicle not only moves horizontally but also it changes its position in altitude. It was not in mind to create a platform for emulating faithfully the dynamics of a ship, as this is a extremely complex task that was out of the scope of our research. However, providing to the platform of a sinusoidal movement along the vertical axis, the landing tests could be similar, in a qualitative way, to the maneuvers that would have to be carried out in a marine environment for landing on a ship's deck.

The first limitation of the platform is that it is not possible to control the roll and pitch angles during the tests. As the platform will be towed by a car in a runway, these angles will remain almost static during the whole experiment. Reference (U.S. Department of Transportation, 2013) describes that when the helicopter is in contact with the surface in the landing phase, it can be affected by a lateral rolling tendency that makes the helicopter to pivot laterally around its skid, and this tendency is called dynamic rollover. It may occur during flight operations on moving vehicles if the platform is rolling and pitching while the helicopter is trying to land. This behavior can be avoided by deploying a gyro-stabilized landing platform in the vehicle allowing a safer operation by achieving a horizontally stable landing surface that minimizes the risk of entering in a dynamic rollover. Hence, the first assumption taken in this appendix is that the landing surface will be leveled during the landing operation without changes in pitch or roll.

With this assumption in mind, it is important to notice that the vertical oscillation of a ship is mainly induced by the different sea states. The sea state is the effect that the local winds have on sea conditions. The Beaufort scale is an empirical measurement that relates wind speed to observed conditions at sea. This scale has been adjusted over the past 200 years, and currently the World Meteorological Organization recognizes thirteen classes, from zero to twelve. Part of the modern

Beaufort scale (U.K National Meteorological Library and Archive, 2012) is shown in Table A-1 .

Beaufort Scale	Wind Velocity (km/h)	Wave height (H)	Wind descriptive terms
0	<1	-	Calm
1	1-5	0.1-0.2	Light air
2	6-11	0.2-0.3	Light breeze
3	12-19	0.6-1.0	Gentle breeze
4	20-28	1.0-1.5	Moderate breeze
5	29-38	2.0-2.5	Fresh breeze
6	39-49	3.0-4.0	Strong breeze
7	50-61	4.0-5.5	Near gale
8	62-74	5.5-7.5	Gale
9	75-88	7.0-10.0	Strong gale
10	89-102	9.0-12.5	Storm
11	103-117	11.5-14.0	Violent storm
12	>118	>15.0	Hurricane

Table A-1: Beaufort scale which relates local wind with the sea state(U.K National Meteorological Library and Archive, 2012)

The vertical oscillation of a ship deck induced by the different sea states can be approximated by the motion of the waves. To this end and according to (Stewart, 2009) the sea-surface elevation z_w of a wave traveling in the X-axis is given by

$$z_w = A_w \sin\left(\frac{2\pi}{L_w} x - 2\pi f_w t\right) \tag{A-1}$$

where A_w is the oscillation amplitude, $f_w$is the wave frequency and f_w is the wave length. The wave length is the distance between two successive wave crests. Regarding the amplitude, it is possible to relate A_w with the Beaufort scale through the wave height H by

$$A_w = \frac{H}{2} \tag{A-2}$$

Concerning the derivation of the wave frequency f_w, reference (Simpson, 2018) establishes that the propagation velocity of a sea wave can be expressed as

$$v_w = \sqrt{\frac{gL_w}{2\pi}\tanh\left(\frac{2\pi D}{L_w}\right)} \tag{A-3}$$

where D is the sea depth and g the acceleration due to gravity. For deep water condition in which the depth is more than half the wavelength ($\frac{D}{L_w} > 0.5$) , it is possible to approach $\tanh\left(\frac{2\pi D}{L_w}\right) \approx 1$ resulting

$$v_w = \sqrt{\frac{gL_w}{2\pi}} \tag{A-4}$$

Finally, using $v_w = L_w f_w$, the wave frequency can be written as

$$f_w = \sqrt{\frac{g}{2\pi L_w}} \tag{A-5}$$

The former derivation allows rewriting eq.(A-1) as

$$z_w = \frac{H}{2}\sin\left(\frac{2\pi}{L_w}x - \sqrt{\frac{2\pi g}{L_w}}t\right) \tag{A-6}$$

Combining this new expression and the Beaufort scale, the vertical oscillation of a ship deck is finally linked to the particular sea state. However, the wave properties are not independent and they should fulfill two conditions. The first condition comes from (Kinsman, 1965): If we can determine the wavelength, the bounds on the wave height will be given by

$$0.008L_w < H < 0.1L_w \tag{A-7}$$

The second condition can be derived from eq.(A-4) and it defines the dispersion relation for deep water, quantifying the link between the period T_w and length of a

water wave. Substituting eq.(A-4) on the definition of wave speed $v_w = \frac{L_w}{T_w}$ yields:

$$T_w = \frac{L_w}{v_w} = \frac{L_w}{\sqrt{\frac{gL_w}{2\pi}}} \tag{A-8}$$

$$T_w{}^2 = \frac{L_w{}^2}{\left(\frac{gL_w}{2\pi}\right)} = \frac{2\pi L_w}{g} \tag{A-9}$$

$$L_w = \frac{g}{2\pi} T_w{}^2 \tag{A-10}$$

where T_w is the period of the waves (time between two consecutive waves). For the sake of simplicity, the second assumption is that the ship heave motion follows the sea surface elevation given by eq.(A-6). As it was pointed out in section 3.2.4, the maximum amplitude of the landing platform in vertical is 4 meters and the maximum velocity is 0.5 m/s. In order to study the similarities between the developed platform and the vertical movement of a ship, we will differentiate the following two scenarios.

Platform is moving only in the vertical axis:

If we neglect the longitudinal motion of the ship, from eq.(A-6)we could model the motion of a deck as:

$$z_w = \frac{H}{2} sin\left(\sqrt{\frac{2\pi g}{L_w}} t\right) = \frac{H}{2} sin\left(\frac{2\pi}{T_w} t\right) \tag{A-11}$$

By varying the control inputs of the platform for the amplitude (A_{cmd})and the vertical velocity ($v_{z,cmd}$),the period of the motion can be approximated by

$$T_p = \frac{2A_{cmd}}{v_{z,cmd}} \tag{A-12}$$

Then, assuming that the ship follows the sea surface, and taking into the account that the maximum amplitude for the platform is 4 meters and its maximum

velocity is 0.5m/s, from the dispersion relation in eq. (A-10)and the boundary equation (A-7) it can be computed that the maximum sea state mechanically possible to reach is five. It is true that the four meters altitude is inside of the sea state 6 in the Beaufort scale, but if the platform is commanded to reach 4 meters at 0.5 m/s, it will need approximately 16 seconds to complete a period. From the dispersion equation this implies that L_w should be 399 meters and if we use that data in eq. (A-7)we see that the condition is met.

Thus, under the assumptions done in this appendix, we can state that if the platform is moving only in the vertical axis, it would be possible to simulate the motion of a ship from sea 0 to sea 5. Figure A-1 and Figure A-2show the movement of the platform when the controller is referenced with the maximum height values presented in the Beaufort table for state 3, 4 and 5 with a vertical velocity of 0.2 m/s and 0.5 m/s respectively.

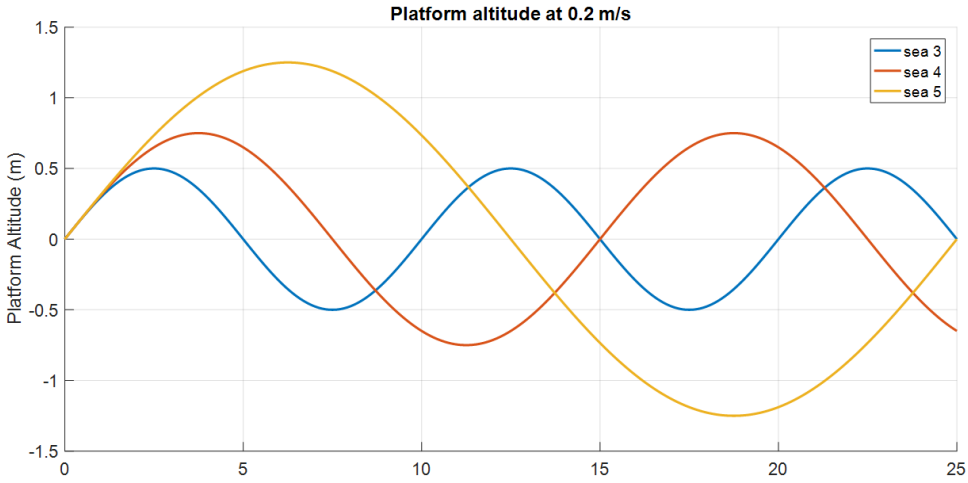

Figure A-1: Landing platform simulating vertical ship movements under sea 3, sea 4 and sea 5 at 0.2 m/s

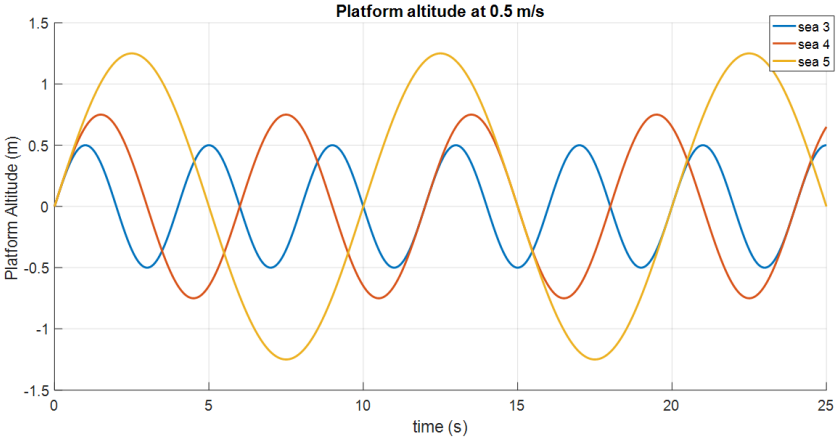

Figure A-2: Landing platform simulating vertical ship movements under sea 3, sea 4 and sea 5 at 0.5 m/s

Moving platform in vertical and horizontal axes:

In order to emulate the motion of a ship deck during a test, the pilot of the car that towes the platform should drive following a speed profile that should be related with the dispersion relation equation, the velocity of the ship, the vertical velocity of the landing platform and several more factors. However, although in these tests the vertical movement of the platform did not emulate the real dynamics of a ship's deck, from a qualitative and experimental point of view they provide a good starting point.

Appendix B

This appendix presents the main coordinated frames used along this thesis and how to perform the transformations between them.

Inertial frame (i-frame)

An inertial frame is a coordinate frame in which Newton's laws of motions apply. Therefore the inertial frame is not accelerating but can be in a linear motion. The origin of the inertial coordinate system is arbitrary, and the coordinate axis may point in any three perpendicular directions. In this case, this frame has its origin at the center of the Earth and axes are non-rotating with respect to distant galaxies. Its z-axis is parallel to the spin axis of the Earth, its x-axis points towards the mean vernal equinox and its y-axis completes a right-handed orthogonal frame as is shown in Figure B-1. The vernal equinox is the ascending node between the celestial equator and the ecliptic.

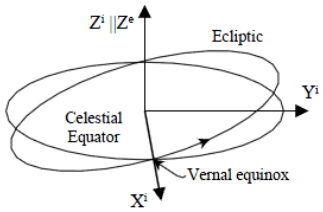

Figure B-1: Inertial Frame

Earth-centered earth-fixed frame (ECEF, e-frame)

This coordinate system has its origin at the center of the earth and rotates with the earth. The axes directions are defined as follows: the x-axis points towards the intersection between the prime meridian and the equator, the z-axis points in the direction of the mean polar axis and the y-axis completes the right-hand coordinate. ECEF coordinate system is depicted in Figure B-2.

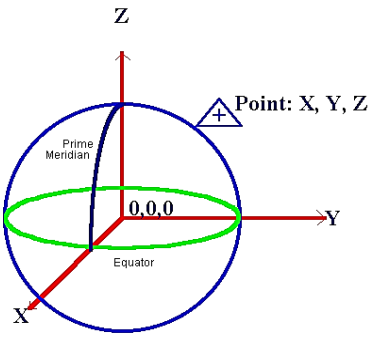

Figure B-2: ECEF coordinate system

LLA Coordinate System

Currently, the most commonly used coordinate system is the latitude, longitude, and altitude (LLA) system. Its origin is at the mass center of the earth. The Prime Meridian and the Equator are the reference planes used to define latitude and longitude. The geodetic latitude of a point is the angle from the equatorial plane to the vertical direction of a line normal to the reference ellipsoid.

The geodetic longitude of a point is the angle between a reference plane and a plane passing through the point, both planes being perpendicular to the equatorial plane. The geodetic altitude at a point is the distance from the reference ellipsoid to the point in a direction normal to the ellipsoid.

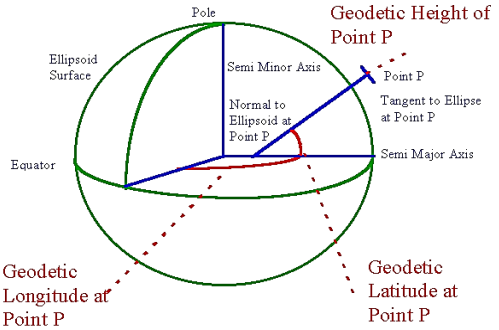

Figure B-3: LLA coordinate system

Local Tangent frame (n-frame)

This is the coordinate system often referred to in our daily life as the north, east and down or up direction. It will be denoted by the superscript t. It's determined by fitting at tangent plane to a fixed point of the geodetic reference ellipse. This point could be the origin of the coordinate system (others origins can be defined) and it is possible to determine two different frames:

- NED: the x-axis points towards the true north, the y-axis to the east and the z-axis completes the right-hand coordinate system by pointing towards the earth's interior.
- ENU: The y-axis points to the East, the y-axis points the true North and the z-axis points up.

In Figure B-4 a local geodetic frame and the ECEF frames are shown:

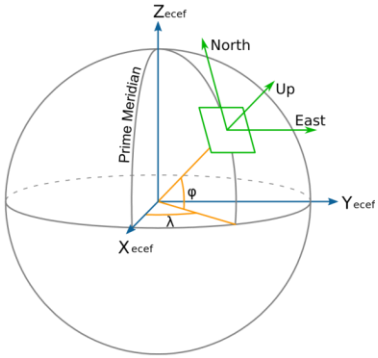

Figure B-4: Relations between ECEF and local tangent frames.

Body frame (b-frame)

The body frame is the coordinate system associated with the vehicle. This system has the origin at the center of gravity of the vehicle and the x-axis points in the forward direction, the z-axis down through the vehicle and the y-axis completes the right-hand coordinate system. In some applications, the instrumentation platform is not aligned with the body frame, and thus a platform frame is needed as well. The platform frame is the coordinate system of the platform in which the accelerometers and the gyros are mounted on. However throughout this thesis, the platform is assumed to have its coordinate axes perfectly aligned with the body coordinate axes, and therefore no distinction between the two frames will be taken

into account.

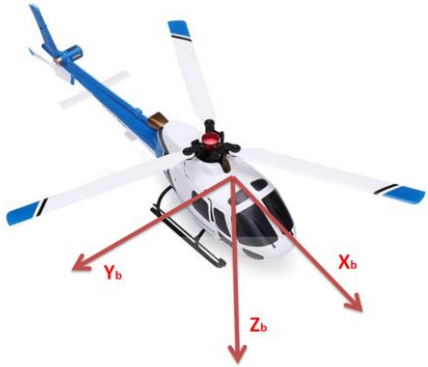

Figure B-5: Body frame

Coordinate Transformations

In this section, it is introduced the transformation relationships among the coordinate frames and some fundamental knowledge related to Cartesian-frame transformations. In navigation systems, it's frequently necessary to transform a vector from one coordinate system into another. Plane rotations are a convenient way to mathematically express the vector transformation between two coordinate frames with a common origin, where the second coordinate system can be related to the first by a rotation around a vector v.

The direction cosine matrix is a matrix that allows changing a coordinate system "b" to another "a".

$$\boldsymbol{C}_b^a = \begin{bmatrix} c_{11} & c_{12} & c_{13} \\ c_{21} & c_{22} & c_{23} \\ c_{31} & c_{32} & c_{33} \end{bmatrix} \tag{B-1}$$

To transform a vector of a coordinate system "b" to another "a", it is necessary to solve the next equation:

$$\begin{bmatrix} x \\ y \\ z \end{bmatrix}^a = \boldsymbol{C}_b^a \begin{bmatrix} X \\ Y \\ Z \end{bmatrix}^b \tag{B-2}$$

The definition of the DCM from the *b*-frame to the *n*-frame requires the introduction of the Euler angles: roll, pitch, and yaw. When using Euler angles it is always necessary to specify the order of rotations.

1. *Yaw*: rotation through the yaw angle Ψ about the vehicle yaw axis to the intended azimuth (heading) of the vehicle roll axis. Azimuth is measured clockwise from North.
2. *Pitch*: rotation through the pitch angle θ about the vehicle pitch axis to bring the vehicle roll axis to its intended elevation. Elevation is measured positive upward from the local horizontal plane.
3. *Roll*: rotation through the roll angle Φ about the vehicle roll axis to bring the vehicle attitude to the specified orientation.

The rotation matrix from the navigation frame to the body frame (rotation order: yaw, pitch, roll) is the following.

$$\boldsymbol{R}_n^b = \begin{bmatrix} cos\theta cos\psi & cos\theta sin\psi & -sin\theta \\ cos\psi sin\theta sin\phi - sin\psi cos\phi & cos\psi cos\phi + sin\psi sin\theta sin\phi & cos\theta sin\phi \\ cos\psi sin\theta cos\phi + sin\psi sin\phi & sin\psi sin\theta cos\phi - cos\psi sin\psi & cos\theta cos\phi \end{bmatrix} \tag{B-3}$$

This matrix satisfies the following property:

$$\boldsymbol{R}_b^n = (\boldsymbol{R}_n^b)^T \tag{B-4}$$

Where the superscript "T" is the transpose operator. From this matrix, the Euler angles can be calculated in the following way:

$$\emptyset = arctan2(\boldsymbol{R}_b^n[3,2], \boldsymbol{R}_b^n[3,3]) \tag{B-5}$$

$$\theta = arcsin(\boldsymbol{R}_b^n[3,1]) \tag{B-6}$$

$$\psi = arctan2(\boldsymbol{R}_b^n[2,1], \boldsymbol{R}_b^n[1,1]) \tag{B-7}$$

Figure B-6depicts the Euler angles (in red), the navigation frame (in bold) and the body axes XYZ.

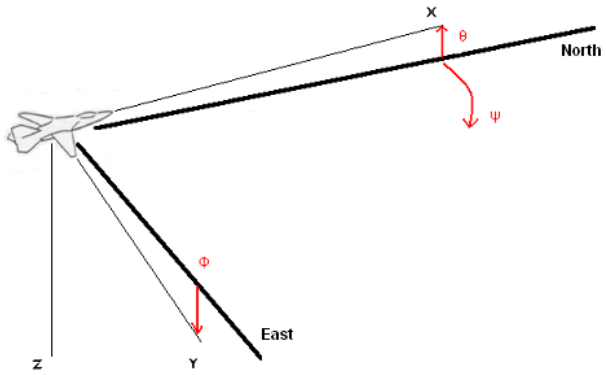

Figure B-6: Euler Angles

For some calculations of this thesis, it will be necessary to transform the rotation vector of the earth frame with respect the inertial frame projected on the earth frame($\underline{\boldsymbol{\omega}}_{ie}^{e}$).

$$\underline{\boldsymbol{\omega}}_{ie}^{e} = [0\ 0\ \omega_e]^T \tag{B-8}$$

Where ω_e is the module of the Earth rotation rate (≈7.2921155 x 10-5 rad/s). This vector is now projected in the navigational frame:

$$\boldsymbol{\omega}_{ie}^{n} = \boldsymbol{R}_{e}^{n}\boldsymbol{\omega}_{ie}^{e} = [\omega_e cos\varphi\ \ 0\ \ -\omega_e sin\varphi] \tag{B-9}$$

Where the DCM between the e-frame and the navigation frame is defined as:

$$\boldsymbol{R}_{e}^{n} = \begin{pmatrix} -sin\varphi cos\lambda & -sin\varphi sin\lambda & cos\varphi \\ -sin\lambda & cos\lambda & 0 \\ -cos\varphi cos\lambda & -cos\varphi sin\lambda & -sin\varphi \end{pmatrix} \tag{B-10}$$

Finally, the velocity of the Earth rotation with respect the Earth frame is expressed in terms of the velocity of change of the latitude and longitude

$$\boldsymbol{\omega}_{en}^{n} = \left[\dot{\lambda}cos\varphi\ \ -\dot{\varphi}\ \ -\dot{\lambda}sin\varphi\right] \tag{B-11}$$

The idea is to have everything related to the position and the velocity, so it will be

necessary to introduce the radii of curvature in the meridian (R_M) and prime vertical (R_N) at a given latitude

$$R_M = \frac{a(1-e^2)}{(1-e^2 sin^2\varphi)^{3/2}} \tag{B-12}$$

$$R_N = \frac{a}{(1-e^2 sin^2\varphi)^{1/2}} \tag{B-13}$$

Where:

- a = 6378137.0 is the semi-major axis length
- e = 0.0818 is the eccentricity of the WGS-84 ellipsoid.

Now it is possible to express the geodetic latitude and longitude rates as follows:

$$\dot{\phi} = \frac{v_N}{R_M + h} \tag{B-14}$$

$$\dot{\lambda} = \frac{v_E}{(R_N + h)cos\varphi} \tag{B-15}$$

Where:

- h is the geodetic height
- v_N and v_E are the velocities in the North and East direction in the navigation coordinate frame.

By substituting eq. (B-14)and (B-15) into eq.(B-8) it is possible to obtain an expression that is function of the position and velocity:

$$\boldsymbol{\omega}_{en}^{e} = \begin{bmatrix} \frac{v_E}{Rn + h} \\ \frac{-v_N}{R_M + h} \\ \frac{-v_E tan\varphi}{R_N + h} \end{bmatrix} \tag{B-16}$$

Finally, the two rotations can be summed to obtain the rotation vector of the navigation frame with respect to the inertial frame.

$$\boldsymbol{\omega}_{in}^{n} = \boldsymbol{\omega}_{ie}^{n} + \boldsymbol{\omega}_{en}^{n} = \begin{bmatrix} \omega_e cos\varphi + \dfrac{v_E}{R_N + h} \\ \dfrac{-v_N}{R_M + h} \\ -\omega_e sin\varphi - \dfrac{V_E tan\varphi}{R_N + h} \end{bmatrix} \tag{B-17}$$

Appendix C

Inertial Measurement Unit

Inertial navigation is a self-contained navigation technique which depends entirely on inertial measurements for navigation. It consists of accelerometers which measure the accelerations in the body axes of the vehicle and gyroscopes which measure the angular rotation of the system. This sensor array is called an Inertial Measurement Unit (IMU). The Inertial Navigation System (INS) is the combination of the IMU sensors and algorithms for determining all navigation states of a moving object, i.e. position, velocity and attitude. Figure C-1 shows the relationship between the INS and the IMU.

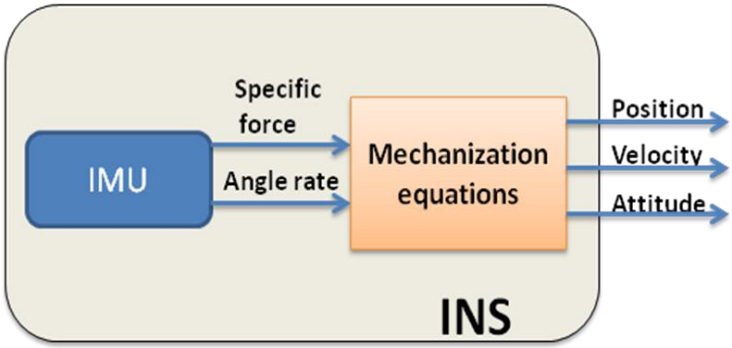

Figure C-1: Relationship between INS and IMU

In the IMU, the accelerometers measure the specific force, defined in the inertial frame as:

$$\boldsymbol{f} = \ddot{\boldsymbol{r}}^{i} - \boldsymbol{g} \tag{C-1}$$

Where:

- f is the specific force

- $\ddot{r}^i$ is the kinematic acceleration in the inertial plane
- g is the gravitational acceleration.

To obtain the velocity of the moving object, it is necessary to correct the specific force by subtracting the gravitational term. Then it can be integrated and the result is added to the initial velocity. Integrating the obtained velocity and adding the initial position, yields the final position. However, the INS is actually more complicated because the measured specific force is expressed in a frame different from the frame in which velocity and position are usually expressed (navigation frame). For this reason, the gyro triad is included in the IMU: gyros are able to measure angular rate with respect to the inertial frame, which, when integrated, provides the angular change with respect to the previous, supposed known, initial orientation. So gyros are used to transform the measured specific force in the navigation frame. It is common to categorize the IMUs based on their accuracy (or grade).

Low-cost MEMS-IMUs can be included in the automotive grade category, since their specifications hardly meet the requirements of a tactical grade unit. However, their considerably lower price, together with the physical characteristics of size and weight, justify the great interest and the huge amount of study and research that has been done on these sensors in the last few years. Due to the cost, size and weight, the MEMS-IMU technology was the chosen option for the autopilot developed in this thesis.

As a dead-reckoning system which determines the current navigation states from the knowledge of the previous states and the measurements of the motion, INS is affected by three types of errors: initial alignment error, inertial sensor error and computational error. These errors are passed from one estimate to the next and result in the overall navigation errors drifting with time. Thus, understanding the characteristics of these errors and developing methods to compensate them in the navigation computation is essential for INS implementation.

Initial Alignment Errors:

Initial alignment is the process whereby the initial attitude, velocity and position of an inertial navigation system are determined based on measurements from the inertial sensors and external sensors. Thus, the alignment accuracy is mainly limited by the effects of sensor errors. Initial alignment errors cannot be estimated

and calibrated because they are unobservable. Initial position errors cause constant position biases while the initial velocity and attitude errors result in position error drifting with time and the square of time, respectively.

Inertial Sensor Errors

Inertial sensors are subject to errors which limit the accuracy of the inertial measurements. The major error sources for inertial sensors are:

- Bias: it is defined as the average over a specified time of the sensor output measured at specified operating conditions that are independent of input acceleration or rotation.
- Scale factor: it is the ratio of a change in output to a change in the input to be measured.
- Random Noise.

These errors include some or all of the following components: fixed terms, temperature induced variations, turn-on to turn-on variations and in-run variations. The fixed component of the error is present each time the sensor is turned on and it is predictable. A large extent of the temperature induced variations can be corrected with a suitable calibration.

These errors can be modeled as:

- Accelerometers:

$$\Delta \boldsymbol{f}^{\boldsymbol{b}} = \boldsymbol{b}_{\boldsymbol{f},\boldsymbol{to}} + \boldsymbol{b}_{\boldsymbol{f}}(t) + \boldsymbol{S}_{\boldsymbol{f}}\boldsymbol{f}^{\boldsymbol{b}} + \boldsymbol{N}_{\boldsymbol{f}}\boldsymbol{f}^{\boldsymbol{b}} + \boldsymbol{\varepsilon}_{\boldsymbol{f}} \tag{C-2}$$

- Gyros

$$\Delta \boldsymbol{\omega}_{\boldsymbol{ib}}^{\boldsymbol{b}} = \boldsymbol{b}_{\boldsymbol{g},\boldsymbol{to}} + \boldsymbol{b}_{\boldsymbol{g}}(t) + \boldsymbol{S}_{\boldsymbol{g}}\boldsymbol{\omega}_{\boldsymbol{ib}}^{\boldsymbol{b}} + \boldsymbol{N}_{\boldsymbol{g}}\boldsymbol{\omega}_{\boldsymbol{ib}}^{\boldsymbol{b}} + \boldsymbol{\varepsilon}_{\boldsymbol{g}} \tag{C-3}$$

Where the different components can be defined as:

- $\boldsymbol{b}_{\boldsymbol{to}}$ **:** The turn-on bias errors vary each time the sensor is turned on but remain constant without power-off, so they can be obtained from laboratory calibrations or estimated during the navigation process and erase them in the navigational solution. This error is modeled with a random constant.

$$\dot{\boldsymbol{b}}_{\boldsymbol{to}}(t) = \mathbf{0} \tag{C-4}$$

- $\boldsymbol{b}(t)$: The in-run random errors are sensitive to dynamics changes and vibrations, so they are unpredictable and vary throughout the periods when the sensor is powered on. These errors cannot be removed from measurements using deterministic models and should be modeled by a stochastic process such as random walk process or Gaussian Markov process.

$$\dot{\boldsymbol{b}}(t) = -\frac{1}{T_b}\boldsymbol{b}(t) + \boldsymbol{w_b}(t) \tag{C-5}$$

where $T_{e,x}$ is the correlation time and $w_{e,x}(t)$ is a white noise process. The cross-coupling error is the error due to sensor sensitivity to inputs about axes normal to an input reference axis. Such error arises through non-orthogonality of the sensor triad and is usually expressed as parts per million (PPM). This error is usually relatively small and negligible compared to other error sources.

- $\boldsymbol{S_f f^b}$ y $\boldsymbol{S_g \omega_{ib}^b}$ are the scale factor error and they are deviations of the mean with respect to the real value that depend on the value of the variable to measure. Matrix $\boldsymbol{S}$ are diagonal matrix $\boldsymbol{S} = diag(S_x \quad S_y \quad S_z)$**.** They use to be assumed as constant during the sensor operation, but in some operations, they can be modelled as Gauss-firs order Markov processes:

$$\dot{\boldsymbol{S}}(t) = -\frac{1}{T_s}\boldsymbol{S}(t) + \boldsymbol{w_s}(t) \tag{C-6}$$

- $\boldsymbol{N_f f^b}$ y $\boldsymbol{N_g \omega_{ib}^b}$ are misalignment errors.
- $\boldsymbol{\varepsilon}(t)$: The random noise is an additional signal resulting from the sensor itself or other electronic equipments that interfere with the output signals being measured. It is often considered time-uncorrelated with zero mean and modeled by a stochastic process, generally a white noise. INS random

noise can be characterized by the average of the standard deviation of static measurements over few seconds.

Of the above error sources, the bias has the most substantial impact on INS navigation performance after the mechanization process. The accelerometer bias results in position error drifting with the square of time while the gyro bias leads to position error drifting with the cube of time. In order to summarize, Table C-1 shows the errors in the INS outputs.

Error	Consequence
Alignment Errors	Roll, pitch and heading errors
Accelerometer bias or o set	A constant o set in the accelerometer output that changes randomly after each turn-on.
Accelerometer scale factor error	Results in an acceleration error proportional to sensed acceleration
Non-orthogonality of gyros and accelerometers	The axes of accelerometers and gyros uncertainty and misalignment.
Gyro drift or bias (due to temperature changes)	A constant gyro output without angular rate presence.
Gyro scale factor error	Results in an angular rate error proportional to the sensed angular rate.
Random noise	Random noise in measurement

Table C-1: errors in the INS outputs

Magnetometer

Magnetometers measure the intensity of the Earth magnetic field. By using the information of the magnetic field in the three axes of the sensor, it is possible to obtain the orientation of the RPAS. Unfortunately, the measurements obtained from low-cost sensors are usually affected by drifts which accumulate in time. These sensors are also sensitive to the environmental parameters, so it is often necessary to perform a calibration just before using them. Measurements provided by a triaxial magnetometer (a set of magnetometers mounted orthogonally to each other) are expressed in the frame of reference defined by the sensors. These

measurements can easily be expressed in the body frame reference frame of the RUAV taking into account the orientation in which the magnetometer has been installed with respect to its body frame. Knowing the attitude of the helicopter, the measurements of the magnetometer can be expressed in the navigation reference frame.

In order to estimate the initial heading of the helicopter, it is defined as a new reference frame obtained from the navigation reference frame by mean of a rotation of the declination angle around the z axis. This will be the magnetic reference frame and it will be considered that aircraft is aligned with this new frame of reference. Under these conditions, the measurements of the magnetometer in the magnetic reference frame are given by:

$$\boldsymbol{m^m} = [m_x \quad 0 \quad m_z]^T \tag{C-7}$$

Here measurements can be obtained from those provided by the magnetometer in the body frame by means of the expression:

$$\boldsymbol{m}^m = \boldsymbol{R}_b^m \boldsymbol{m}^b = (\boldsymbol{R}_m^b)^{-1} \boldsymbol{m}^b = (\boldsymbol{R}_m^b)^T \boldsymbol{m}^b \tag{C-8}$$

Due to the matrix DCM $\boldsymbol{R}_m^b$ can be expressed as:

$$\boldsymbol{R}_m^b = \boldsymbol{R}(\phi)\boldsymbol{R}(\theta)\boldsymbol{R}(\Delta\psi) \tag{C-9}$$

And then the matrix $\boldsymbol{R}_b^m$ can take the following form:

$$\begin{aligned} \boldsymbol{R_b^m} = \big(\boldsymbol{R}(\phi)\boldsymbol{R}(\theta)\boldsymbol{R}(\Delta\psi)\big)^{\boldsymbol{T}} &= \boldsymbol{R^T}(\Delta\psi)\boldsymbol{R^T}(\theta)\boldsymbol{R^T}(\phi) \\ &= \boldsymbol{R}(-\Delta\psi)\boldsymbol{R}(-\theta)\boldsymbol{R}(-\phi) \end{aligned} \tag{C-10}$$

If eq.(C-10) is applied in eq.(C-7), it is obtained:

$$\boldsymbol{R}(\Delta\psi)\begin{bmatrix} m_x^m \\ 0 \\ m_z^m \end{bmatrix} = \boldsymbol{R}(-\theta)\boldsymbol{R}(-\phi)\begin{bmatrix} m_x^b \\ m_y^b \\ m_z^b \end{bmatrix} \xrightarrow{\textbf{yields}}$$

$$\begin{bmatrix} \cos(\Delta\psi)m_x^m \\ -\text{sen}(\Delta\psi)m_x^m \\ m_z^m \end{bmatrix} = \begin{bmatrix} \cos(\theta)m_x^b + \text{sen}(\theta)\text{sen}(\phi)m_y^b + \text{sen}(\theta)\cos(\phi)m_z^b \\ \cos(\phi)m_y^b - \text{sen}(\phi)m_z^b \\ -\text{sen}(\theta)m_x^b + \cos(\theta)\text{sen}(\phi)m_y^b + cos(\theta)\cos(\phi)m_z^b \end{bmatrix} \quad \text{(C-11)}$$

The initial heading of the helicopter with respect the magnetic north can be obtained from the following expression:

$$\tan(\Delta\psi) = -\frac{\cos(\phi)m_y^b - \text{sen}(\phi)m_z^b}{\cos(\theta)m_x^b + \text{sen}(\theta)\text{sen}(\phi)m_y^b + \text{sen}(\theta)\cos(\phi)m_z^b} \quad \text{(C-12)}$$

Finally, the heading of the RUAV with respect the geographic north can be calculated taking into account the magnetic deviation D of the location where it is performing the mission:

$$\psi = \Delta\psi + D \quad \text{(C-13)}$$

The performance of a magnetometer will greatly depend on its installation location in the vehicle. A compass depends on the earth's magnetic field to provide heading solutions. Any distortions of this magnetic field by other sources should be compensated in order to determine an accurate heading. Sources of magnetic fields include permanent magnets, motors, electric currents, either dc or ac, and magnetic metals such as steel or iron. The influence of these sources on compass accuracy can be greatly reduced by placing the compass far from them. Some of the field effects can be compensated by calibration. However, it is not possible to compensate for time-varying magnetic fields; for example, disturbances generated by the motion of magnetic metals, or unpredictable electrical current in a nearby wire (Caruso, 1997). When the measures of a magnetometer are represented on the y-axis and against the measures of the x-axis of the navigation frame, in the absence of magnetic perturbations unrelated to the geomagnetic field, the result must be a circumference whose origin is at point (0,0)(Caruso, 2000)

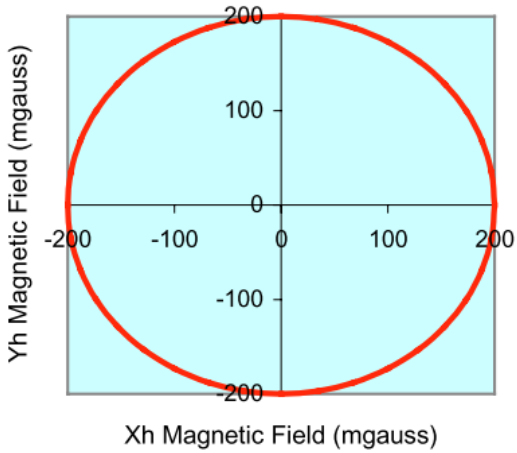

Figure C-2: Representation of measures of the y- axis against the measurements on the navigation x-axis in the absence of magnetic disturbances (Caruso, 2000)

Magnetic distortions can be categorized into two types:

- Hard iron: errors are induced by permanent unwanted fields (Madwick, Harrison and Vaidyanathan, 2011). They are generated by ferromagnetic materials attached to the magnetometer frame (Caruso, 2000), typically by the structure or the equipment installed near the magnetometer or even by non-varying currents in close-by wires. This type of error results in a bias.
- The soft iron distortion arises from the interaction of the earth's magnetic field and any magnetically soft material surrounding the compass. Like the hard iron materials, the soft metals also distort the earth's magnetic field lines. The difference is that the amount of distortion from the soft iron depends on the compass orientation.

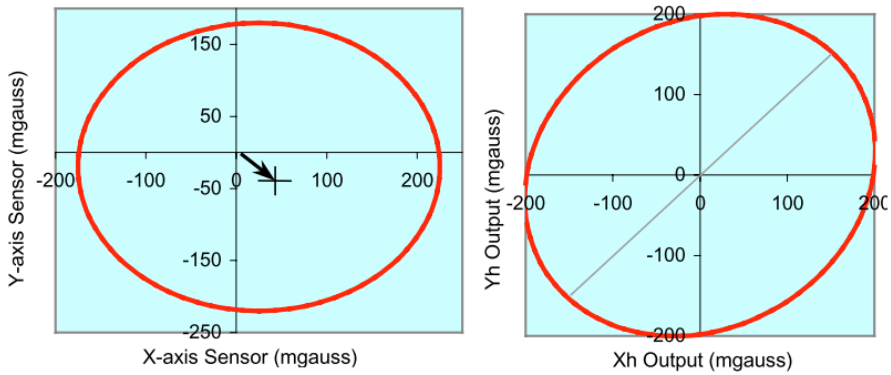

Figure C-3: Representation of measures of the y-axis against the measurements on the navigation x-axis in the absence of magnetic disturbances [4]

Taking these two effects into account, the measurements in the horizontal plane tangent to the reference ellipsoid of the Earth at a given location are given by the real value of the geomagnetic field multiplied by a scale factor m_{sf} and to the addition of a constant offset value m_o. In this way they can be expressed as:

$$\hat{m}_x^m = m_{sf,x} m_x^m + m_{o,x} \tag{C-14}$$

$$\hat{m}_y^m = m_{sf,y} m_y^m + m_{o,y} \tag{C-15}$$

A simple calibration method of magnetometers similar to the one proposed in (Caruso, 1997) has been used in this thesis. It consists on rotating the vehicle in a complete sweep of the interval [-*Π*, *Π*]. From the obtained measurements, the scale factors and offsets can be calculated as:

$$the\ bigger\ between: m_{sf,x} = \frac{m_{y,max}^m - m_{y,min}^m}{m_{x,max}^m - m_{x,min}^m}\ or\ m_{sf,x} = 1 \tag{C-16}$$

$$the\ bigger\ between: m_{sf,y} = \frac{m_{x,max}^m - m_{x,min}^m}{m_{y,max}^m - m_{y,min}^m}\ \text{or}\ m_{sf,y} = 1 \tag{C-17}$$

$$m_{o,x} = [(m_{x,max}^m - m_{x,min}^m)/2 - m_{x,max}^m] m_{sf,x} \tag{C-18}$$

$$m_{o,y} = [(m_{y,max}^m - m_{y,min}^m)/2 - m_{y,max}^m] m_{sf,y} \tag{C-19}$$

For most of the cases, if a good initial calibration is done, the error in the heading solution is not too large.

Global Positioning System

The Global Positioning System is an absolute navigation system developed by the US Department of Defense in 1973. It became fully operational in 1995 with a minimum of 24 satellites on six equally spread orbits around the Earth located about 20200 km above its surface. The GPS is able to provide continuous information about the position and velocity in the three dimensions and the Coordinated Universal Time (UTC) via its satellite constellation. Each GPS satellite transmits the data on two frequencies: L1 (1575.42 MHz) and L2 (1227.60 MHz). It is necessary to receive at least the information of 4 satellites to be able of calculating a 3D position solution. For these calculations, the first step is to know the positions of the satellites that the receptor is measuring. This information is obtained from the ephemeris data transmitted by the satellites, which provides their positions in the Earth-Centered Earth-Fixed (ECEF) Coordinates.

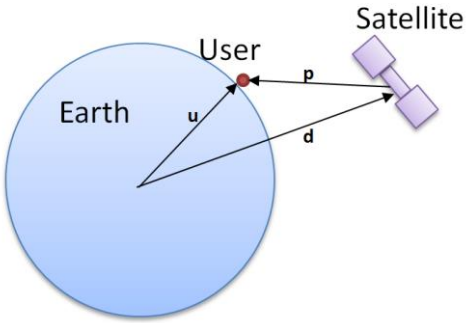

Figure C-4: GPS position Calculation

As is possible to see in Figure C-4, the user position (u) can be calculated by using the pseudorange information (p) and the satellite position (d) as:

$$u = \rho_i + d_i \tag{C-20}$$

Where "i" is the index that determines the satellite that sends the data.

The GNSS is able to calculate the pseudoranges by measuring the traveling time of the data and assuming that it travels at the velocity of the light (c).

$$\rho_i = c(t_r - t_t) \tag{C-21}$$

Where t_r is the time in which the GNSS sensor receives the signal and t_t is the time in which the satellite sent the data. With this information, it is possible to calculate the user position in the following way:

$$\rho_i = \|u - d_i\| + c \cdot C_c + \epsilon_i \tag{C-22}$$

In eq. (C-22) C_c is an error due to the clock drifts in the satellite and receiver. The remaining error components are collected in ϵ_i. Disregarding this term, four equations are needed in order to know the position vector of the user "u" and the clock error. Usually, there are more than four satellites available. So if this over-determined system can be solved, for example, with a least-squares strategy, a more accurate solution can be achieved.